**Title**
Nanotopographical Cues for Modulating Fibrosis and Drug Delivery



**Author**
Walsh, Laura

**Publication Date**
2016

Peer reviewed|Thesis/dissertation

Nanotopographical Cues for Modulating Fibrosis and Drug Delivery

by

Laura Aiko Michelle Walsh

DISSERTATION

Submitted in partial satisfaction of the requirements for the degree of

DOCTOR OF PHILOSOPHY

in

Bioengineering

in the

GRADUATE DIVISION

of the

UNIVERSITY OF CALIFORNIA, SAN FRANCISCO

AND

UNIVERSITY OF CALIFORNIA, BERKELEY

## Dedication and Acknowledgements

This manuscript is dedicated to my family: my parents, who have worked so hard to give me every opportunity and were always there for me; my best friend and husband Alex; my brother Freddy; and my grandma, Miyoko.

I would like to acknowledge and thank my thesis advisor, Dr. Tejal Desai. I would like to also acknowledge my mentors, fellow lab mates, and students, in particular Kayte, Kim, Jennifer, Jessica, Molly, and my coauthors on the following manuscripts included in this body of work:

Uskoković, V., Lee, P. P., Walsh, L. A., Fischer, K. E. & Desai, T. A. PEGylated silicon nanowire coated silica microparticles for drug delivery across intestinal epithelium. *Biomaterials* **33,** 1663–72 (2012).

Kam KR, Walsh LA, Bock SM, Koval M, Fischer KE, Ross RF, Desai TA. Nanostructure-mediated transport of biologics across epithelial tissue: enhancing permeability via nanotopography. *Nano Lett.* **13,** 164–71 (2013).

Kam KR, Walsh LA, Bock SM, Ollerenshaw JD, Ross RF, Desai TA. The effect of nanotopography on modulating protein adsorption and the fibrotic response. Tissue Eng Part A. 2014 Jan;20(1-2):130-8.

Walsh L, Ryu J, Bock S, Koval M, Mauro T, Ross R, **Desai** T. Nanotopography facilitates in vivo transdermal delivery of high molecular weight therapeutics through an integrin-dependent mechanism. Nano Lett. 2015 Apr 8;15(4):2434-41.

## Abstract

Nanotopography in the cellular microenvironment provides biological cues and therefore has potential to be a useful tool for directing cellular behavior. Fibrotic encapsulation of implanted devices and materials can wall off and eventually cause functional failure of the implant. Drug delivery requires penetrating the epithelium, which encapsulates the body and provides a barrier to separate the body from its external environment. Both of these challenges could be elegantly surmounted using nanotopography, which would harness innate cellular responses to topographic cues to elicit desired cellular behavior. To this end, we fabricated high and low aspect ratio nanotopographically patterned thin films. Using scanning electron microscopy, real time polymerase chain reaction, immunofluorescence microscopy, *in vitro* drug delivery assays, transmission electron microscopy, inhibitor studies, and rabbit and rat *in vivo* drug delivery studies, we investigated cellular response to our nanotopographic thin films. We determined that high aspect ratio topography altered fibroblast morphology and decreased proliferation, possibly due to decreased protein adsorption. The fibroblasts also down regulated expression of mRNA of key factors associated with fibrosis, such as collagens 1 and 3. Low aspect ratio nanotopography increased drug delivery *in vitro* across an intestinal epithelial model monolayer by increasing paracellular permeability and remodeling the tight junction. This increase in drug delivery required integrin engagement and MLCK activity, and is consistent with the increased focal adhesion formation. Tight junction remodeling was also observed in a multilayered keratinocyte model, showing this mechanism can be generalized to multiple epithelium types. By facilitating direct contact of nanotopography with the viable epidermis using microneedles to

pierce the stratum corneum, we are able to transdermally deliver a 150 kiloDalton, IgG-based therapeutic *in vivo*.

## Table of Contents

# List of Figures

## Chapter 3



## Chapter 4

**Chapter 5**

# Introduction

## Cellular interaction with biomaterials

Cells are finely tuned to adapt and react to environmental cues – biochemical and physical. It is well established that cells are capable of responding to nanoscale cues found in their microenvironment. The extracellular matrix (ECM) is a hierarchical environment containing microscale to nanoscale features ranging from microns to tens of nanometers in length. The ECM is composed of complex architectural features at the nanoscale, including pores, fibers, ridges, and protein band periodicities of ~60 nanometer (nm).[1] Nanoscale features, being at the subcellular size scale, have the ability to influence cellular behaviors such as morphology, proliferation, and differentiation.[2–4] Therefore, nanotopography -- defined as a sub-micron textured surface where the surface features have at least one dimension on the nanoscale -- offers the opportunity to perturb a wide range of cellular responses. A better understanding of the cell–material interface on the nanoscale enables the exploration of a spectrum of interactions that are crucial to designing advanced medical devices and implants, but also open the door to a novel way of directing cellular behavior.

Contact of biomaterials with biological fluid immediately results in the adsorption of proteins onto the surface of the material. These proteins serve as cellular receptors for interaction and adhesion.[5] It is well established that modifying the nanotopography of a surface influences the adsorption of proteins and other biomolecules.[6–10] Increased surface roughness of poly(methyl methacrylate) (PMMA) increased hydrophobicity, which increased protein adsorbtion.[6] Decreasing the pore size, 45 to 2.2 nm, on silica particles decreased adsorption of bovine serum albumin.[10] Therefore, modification of biomaterial surfaces can be a tool to direct cellular

interaction and adhesion. Indeed, surface alteration has been shown to effect the extent of cellular adhesion.[6,11–17] Increasing the surface roughness of PMMA increased cellular adhesion of chick embryo vascular and corneal explant cells, probably due to changes in fibronectin adsorption.[6] The amount of protein adsorption paralleled the adherence of human osteoblast-like cells on titanium surfaces of different roughnesses.[12]

**Nanotopography and Fibrosis**

Implant-induced fibrosis has generated much attention in the medical community and in the field of tissue engineering. Almost all soft tissue implants undergo fibrotic encapsulation and eventual loss of functional tissue in the vicinity surrounding the implant. The fibroblast is a specific cell that synthesizes and deposits the extracellular matrix, forming the structural network for soft tissue. Although it plays a critical role in wound healing, the over-proliferation of fibroblasts and the subsequent overproduction of ECM proteins have been implicated in fibrosis. It is well known that implant fibrosis and fibrotic encapsulation can often contribute to medical device failures, ranging from breast implant contracture to biosensor inactivation.[18–20] Fibrosis has also been implicated in postsurgical adhesions, contributing to the failure of gastrointestinal, gynecological, and sinus surgeries.[21]

To this end, new biomaterial interfaces that foster an antifibrotic environment must be developed. Previously, there has been considerable work on chemistry-based approaches for decreasing fibrosis. For example, Risbud et al. reported how biocompatible hydrogels composed of chitosan-pyrrolidone arrest capsular fibroblast growth.[22] Other materials such as alginate, hyaluronic acid, and derivatives of chitin have been demonstrated to mimic fetal wound healing by selectively inhibiting fibroblast growth.[23,24] Recently, however, it has been established that cells are capable of responding to nanotopographical cues found in their microenvironment.

Therefore, nanotopography offers the opportunity to perturb a wide range of cellular responses. A better understanding of the cell–material interface on the nanoscale enables the exploration of a spectrum of interactions that are crucial to designing advanced medical devices and implants. Herein we report how nanostructured biomaterials can be used to generate an antifibrotic environment for cells.

To investigate how nanotopography influences cellular behavior, nanostructures must be fabricated with a high level of repeatability and precision. Current advancements in nano- and microtechnology offer new possibilities of probing cell–material interactions to better understand biological functions.[25,26] Ranging from microcontact printing to photolithography, there are various techniques for systematically controlling topographical features. One such fabrication technique to achieve nanofeatures is nanoimprint lithography (NIL). This technique is a stamping process capable of generating nanometer length patterns as small as 10 nm.[27,28] In contrast to conventional photolithography, nanofeatures are generated by the mechanical deformation of a thermoplastic material using a mold with nanofeatures. Molds are fabricated using electron beam lithography to overcome the diffraction limit of light and to produce features on the nanoscale.

The design of the nanostructured substrates was inspired by the ECM that surrounds soft tissue implants. Mimicking the ECM involved rationally designing structures that were similar to collagen, the most abundant ECM protein in the body. Collagen consists of staggered arrays of tropocollagen molecules that bind together to form fibrils. These collagen fibrils have diameters that range from 100 to 500 nm and lengths up to the millimeter length scale.[29] Despite significant research efforts over the past two decades, the effect of collagen fibril geometry on wound healing and fibrosis remains largely unknown.

Fibrosis is the scarring and stiffening of tissue from the accumulation of excess extracellular matrix in response to chronic inflammatory processes and foreign materials. During the fibrotic response, fibroblasts are recruited to the site of tissue injury and differentiate into myofibroblasts in response to chemical cues such as transforming growth factor beta (TGFb) and chemokines, and physical cues such as tension.[30–32] Activated myofibroblasts promote the turnover of established extracellular matrix and synthesize new ECM proteins, while also providing the mechanical tension to close wounds.[33,34] Herein we examine the effect of nanotopography on fibroblast phenotype and function by investigating the ability of topography to decrease the fibrotic activity of fibroblasts as measured by fibroblast proliferation, morphology, and expression of profibrosis genes.

## Nanotopography applications in drug delivery

Nanotopography represents a versatile new tool in the field of drug delivery with the potential to improve upon harsher or more complex chemical and physical delivery techniques. The range of available topography geometry and fabrication methods has led to applications in multiple modalities of drug delivery, including intracellular and transcellular delivery, both via oral and transdermal delivery methods.

### Intracellular Delivery

Intracellular delivery of drugs, ranging from small ribonucleic acids (RNAs) up to macromolecules, holds powerful therapeutic potential. Nanotechnology has already shown promise in targeted drug delivery for a number of disease models .[35] Within this field, several distinct nanotopographies have demonstrated robust intracellular delivery of drug via different modalities. First, Dalby et al developed nanotopography that increases drug delivery by

activating endocytosis.[36] Fabrication of the nanocolumns was achieved through colloidal lithography, whereby a colloidal mask was electrostatically adsorbed followed by ion beam etching to create nanopillar topography. Fibroblasts in contact with the nanopillars showed increased endocytic activity, demonstrated by an increase in clathrin and dynamin localization around columns. Analyzing fibroblast phenotype by transmission electron microscopy (TEM) revealed that cells seeded on these structures increased vesicle formation and attempted to internalize the columns. These findings suggest cell contact with nanocolumns activates endocytosis. Echoing this finding, Teo et al have found that cellular interaction with nanotopography can encourage drug uptake by micropinocytosis.[37] Teo developed nano and micropillars using a stamping process called nanoimprint lithography. Both human mesenchymal stem cells (hMCSs) and monkey kidney fibroblasts increased internalization of dextran while interacting with either nano or micropillars. However, transfection efficiency was highest in hMSCs cultured on nanopillars, demonstrating that this is a cell and structure-scale dependent effect. Moreover, Solanki et al demonstrated that nanotopography improves the efficiency of small interfering ribonucleic acids (siRNA) uptake in stem cells.[38] Solanki coated a monolayer of self-assembled silica nanoparticles with both laminin and siRNA. Neural stem cells showed maximal gene knockdown in cells seeded on 100 nm silica particles. Interestingly, this technique was shown to be generalizable to siRNA delivery to other mammalian cell types.

Moreover, nanotopography, specifically nanowires and nanotubes which demonstrate robust regulation of cell growth and material biocompatibility[39,40], can also directly deliver a drug intracellularly.[41,42] Silicon nanowires grown by either chemical vapor deposition or reactive ion etching have both been shown to penetrate the cell membrane while maintaining membrane integrity. The target molecule can be loaded on to nanowires by surface-modification and

delivered directly into the cytosol of cells. Shalek et al demonstrated the delivery of a small molecule, siRNA, peptides, and proteins, as well as co-delivery of siRNA and protein.[41] Similarly VanDersarl et al, inspired by gap junctions and other stable conduits for intracellular communication, have developed nanostraws that can directly deliver drug into the cytosol (Figure 1).[43] Nanostraws of tunable diameter and length were created by coating filter membranes with alumina then selectively etching away the membrane. Nanostraws directly delivered small molecules, proteins, and plasmids without endocytosis or adenovirus vectors. Furthermore, these connections were stable for several days, negating the need for repeat penetrations.

### Transepithelial Delivery

While direct intracellular delivery is a powerful technique, it requires direct access to cells or tissues of interest. Systemic drug delivery requires circumventing the epithelium, a substantial barrier that separates the body from its external environment. The epithelium is a functionalized tissue designed to compartmentalize the body. As such, the epithelium is a significant obstacle to drug delivery, especially for high molecular weight therapeutics. The newest generation of drugs is biologics. Biologics include protein, peptide, and siRNA based drugs, and are all developed from an understanding of the biology of a disease. With a tailored approach to drug development, these therapeutics hold great potential. However, biologics face many drug delivery limitations, and poor drug distribution and low absorption levels lead to many developed drugs not reaching commercial markets. Diffusion and delivery of biologics are limited by their size, chemistry, and clearance rates. For instance, the rate of diffusion across the gastrointestinal epithelium of molecules greater than 20 kilo Dalton (kDa) is highly limited, while the same limit for the stratum corneum of the skin is 0.5 kDa.

Skin serves as the critical boundary between the external world and our viscera. The stringency of the epidermal barrier is reflected by the dearth of transdermally delivered drugs; currently only 17 drugs have been approved for this delivery route by the Food and Drug Administration (FDA), and all of these agents fall within a very narrow parameter space (<500 Daltons in size and highly lipophilic). The limitations of transdermal technology appear even starker with the increasingly frequent development of high molecular weight, antibody-based therapeutics, many of which have promising biologic effects but are hampered by limited delivery options.

Until recently, skin barrier function was thought to be mediated entirely by the outermost stratum corneum, a defined meshwork of anucleate keratinocytes, lipids, and proteins. However, recent studies have discovered the presence of the epidermal tight junction (TJ) and multiple TJ proteins, including occludin, zonula occludins-1 (ZO-1), and in particular claudins, which are critical for epidermal barrier function[44–51] . TJ complexes function as the paracellular barrier in simple epithelial cell types such as gastrointestinal mucosal cells and offer an additional well-conserved mechanism through which the skin can regulate its permeability[52–54]. Tight junctions are cell to cell junctions that determine the flow of molecules and fluid.[55] Claudins, a class of transmembrane proteins, interact with adjacent cell claudins to occlude the paracellular space.[56,54,53] Claudins, and therefore tight junctions, are linked to the cytoskeleton by binding to proteins like ZO-1, which also binds to actin.[48] Thus, the cellular pathways that lead to the interaction of the cell with surfaces could draw away actin from the TJs allowing for increased permeability. While multiple technologies have attempted to increase the permeability of the stratum corneum less emphasis has been placed on modulation of the skin TJ barrier[57–60].

Intravenous or subcutaneous injection is the standard method of administration of larger drugs and biologics. Various chemical and physical methods have been employed to deliver drug

across epithelia without injection, but drugs delivered are limited to low molecular weights.[61–66] Nanotopography has shown promise in improving transepithelial drug delivery in two ways, by increasing the time and concentration gradient across the epithelium or by perturbation of cell-cell attachments like tight junctions. Fischer et al have demonstrated that silicon nanowires, grown by a vapor-liquid-solid method on glass microbeads, can increase adhesion to epithelium *in vitro* and *in vivo*.[67] In the context of oral drug delivery, this increased adhesion of drug loaded microbeads to the intestine increasing the residence time and concentration gradient, which drives drug diffusion across the intestine. Under *in vitro* mucus flow, microbeads coated with longer nanowires had significantly longer median survival times and resisted higher shear than those coated with shorter nanowires or nanowires coated in a mucoadhesive, lectin. The force needed to dislodge the nanowire coated beads increased 100 fold compared to non-coated controls. *In vivo*, nanowire coated microbeads increased residence time in the gastrointestinal tract by ten-fold compared to non-coated controls. Nanowires additionally have been found to modulate the barrier function of epithelium. With silicon nanowires grown on silica microbeads, Uskoković et al demonstrated that, in addition to adhesion, barrier function of the epithelium was also disrupted. In an intestinal cell line, Caco2, nanowires increased permeability, as measured by transport of fluorescein-Na, and decreased barrier function, as measured by transepithelial resistance (TER).[68] Specifically, the nanowires disrupted the tight junctions, the major determinant of paracellular permeability.

Cells are sensitive to the specific spacing between nanostructures.[69] Studies have also shown that the surface area of topographical features limits the size of the focal complexes that can form.[10,70] It has been observed that the size and shape of the focal adhesion has functional consequences.[71–73] Additionally, the spacing between focal adhesions also have an effect on

signaling.[73] It is well established that cells can interact with nanostructures using integrins and form focal complexes and adhesions.[74,75] These complexes link the extracellular environment to the actin cytoskeleton of the cell. TJs are also intimately connected to the actin cytoskeleton and sensitive to actin dynamics.[76] Building off of prior work in the lab using silica nanowire coated microbeads, which altered the barrier function of an intestinal epithelium model, we examined a repertoire of low aspect ratio nanotopography geometries for their ability to modulate the barrier function of both intestinal and epidermis. We hypothesized that nanotopographical geometries can modulate epithelial permeability. We examined transcellular transport by changes gene expression, measuring drug endocytosis, and inhibiting endocytic pathways. Tight junction structure and expression of related genes was measured as an indication of nanotopography's effect on paracellular transport. Cellular interaction with the nanotopography was studied by visualization of focal adhesion formation and downstream mechanotransduction signaling. Finally, we discovered that nanotopography mediated drug transport could be generalized from a gastrointestinal model to increase transdermal drug delivery *in vivo*.

**References:**


1. Yim, E. K. F. *et al.* Nanopattern-induced changes in morphology and motility of smooth muscle cells. *Biomaterials* **26,** 5405–13 (2005).

2. Pennisi, C. P. *et al.* Nanoscale topography reduces fibroblast growth, focal adhesion size and migration-related gene expression on platinum surfaces. *Colloids Surf. B. Biointerfaces* **85,** 189–97 (2011).

3. Kim, D.-H. *et al.* Mechanosensitivity of fibroblast cell shape and movement to anisotropic

substratum topography gradients. *Biomaterials* **30,** 5433–5444 (2009).

4. Karuri, N. W., Porri, T. J., Albrecht, R. M., Murphy, C. J. & Nealey, P. F. Nano- and microscale holes modulate cell-substrate adhesion, cytoskeletal organization, and -beta1 integrin localization in SV40 human corneal epithelial cells. *IEEE Trans. Nanobioscience* **5,** 273–80 (2006).

5. Balasubramanian, V., Grusin, N. K., Bucher, R. W., Turitto, V. T. & Slack, S. M. Residence-time dependent changes in fibrinogen adsorbed to polymeric biomaterials. *J. Biomed. Mater. Res.* **44,** 253–60 (1999).

6. Lampin, M., Warocquier-Clérout, Legris, C., Degrange, M. & Sigot-Luizard, M. F. Correlation between substratum roughness and wettability, cell adhesion, and cell migration. *J. Biomed. Mater. Res.* **36,** 99–108 (1997).

7. Lück, M., Paulke, B. R., Schröder, W., Blunk, T. & Müller, R. H. Analysis of plasma protein adsorption on polymeric nanoparticles with different surface characteristics. *J. Biomed. Mater. Res.* **39,** 478–85 (1998).

8. McFarland, C. D., Thomas, C. H., DeFilippis, C., Steele, J. G. & Healy, K. E. Protein adsorption and cell attachment to patterned surfaces. *J. Biomed. Mater. Res.* **49,** 200–10 (2000).

9. Denis, F. A. *et al.* Protein Adsorption on Model Surfaces with Controlled Nanotopography and Chemistry. *Langmuir* **18,** 819–828 (2002).

10. Kim, D.-H. *et al.* Modulation of adhesion and growth of cardiac myocytes by surface nanotopography. *Conf. Proc. ... Annu. Int. Conf. IEEE Eng. Med. Biol. Soc. IEEE Eng.*

*Med. Biol. Soc. Conf.* **4,** 4091–4094 (2005).

11. Naji, A. & Harmand, M. F. Study of the effect of the surface state on the cytocompatibility of a Co-Cr alloy using human osteoblasts and fibroblasts. *J. Biomed. Mater. Res.* **24,** 861–71 (1990).

12. Martin, J. Y. *et al.* Effect of titanium surface roughness on proliferation, differentiation, and protein synthesis of human osteoblast-like cells (MG63). *J. Biomed. Mater. Res.* **29,** 389–401 (1995).

13. Altankov, G., Grinnell, F. & Groth, T. Studies on the biocompatibility of materials: fibroblast reorganization of substratum-bound fibronectin on surfaces varying in wettability. *J. Biomed. Mater. Res.* **30,** 385–91 (1996).

14. Kanagaraja, S., Lundström, I., Nygren, H. & Tengvall, P. Platelet binding and protein adsorption to titanium and gold after short time exposure to heparinized plasma and whole blood. *Biomaterials* **17,** 2225–32 (1996).

15. Steele, J. G., Johnson, G., Griesser, H. J. & Underwood, P. A. Mechanism of initial attachment of corneal epithelial cells to polymeric surfaces. *Biomaterials* **18,** 1541–51 (1997).

16. Balcells, M. & Edelman, E. R. Effect of pre-adsorbed proteins on attachment, proliferation, and function of endothelial cells. *J. Cell. Physiol.* **191,** 155–61 (2002).

17. Lan, S., Veiseh, M. & Zhang, M. Surface modification of silicon and gold-patterned silicon surfaces for improved biocompatibility and cell patterning selectivity. *Biosens. Bioelectron.* **20,** 1697–708 (2005).

18. Chegini, N. Peritoneal molecular environment, adhesion formation and clinical implication. *Front. Biosci.* **7,** e91–115 (2002).

19. Hunter, L. W., Lieske, J. C., Tran, N. V & Miller, V. M. The association of matrix Gla protein isomers with calcification in capsules surrounding silicone breast implants. *Biomaterials* **32,** 8364–73 (2011).

20. Giurgiutiu, V. *et al.* Electromechanical impedance sensor for in vivo monitoring the body reaction to implants. *J. Invest. Surg.* **17,** 257–70

21. Schippers, E., Tittel, A., Ottinger, A. & Schumpelick, V. Laparoscopy versus laparotomy: comparison of adhesion-formation after bowel resection in a canine model. *Dig. Surg.* **15,** 145–7 (1998).

22. Risbud, M., Hardikar, A. & Bhonde, R. Growth modulation of fibroblasts by chitosan-polyvinyl pyrrolidone hydrogel: implications for wound management? *J. Biosci.* **25,** 25–31 (2000).

23. Li, Y., Rodrigues, J. & Tomás, H. Injectable and biodegradable hydrogels: gelation, biodegradation and biomedical applications. *Chem. Soc. Rev.* **41,** 2193–221 (2012).

24. Mast, B. A., Diegelmann, R. F., Krummel, T. M. & Cohen, I. K. Hyaluronic acid modulates proliferation, collagen and protein synthesis of cultured fetal fibroblasts. *Matrix* **13,** 441–6 (1993).

25. Tian, Y. C. & Phillips, A. O. Interaction between the transforming growth factor-beta type II receptor/Smad pathway and beta-catenin during transforming growth factor-beta1-mediated adherens junction disassembly. *Am. J. Pathol.* **160,** 1619–28 (2002).

26. Sharma, G. *et al.* Polymer particle shape independently influences binding and internalization by macrophages. *J. Control. Release* **147,** 408–12 (2010).

27. Chou, S. Y. & Krauss, P. R. Imprint lithography with sub-10 nm feature size and high throughput. *Microelectron. Eng.* **35,** 237–240 (1997).

28. Chou, S. Y., Krauss, P. R. & Renstrom, P. J. Imprint Lithography with 25-Nanometer Resolution. *Science (80-. ).* **272,** 85–87 (1996).

29. Gautieri, A., Vesentini, S., Redaelli, A. & Buehler, M. J. Hierarchical structure and nanomechanics of collagen microfibrils from the atomistic scale up. *Nano Lett.* **11,** 757–66 (2011).

30. Tomasek, J. J., Gabbiani, G., Hinz, B., Chaponnier, C. & Brown, R. A. Myofibroblasts and mechano-regulation of connective tissue remodelling. *Nat. Rev. Mol. Cell Biol.* **3,** 349–63 (2002).

31. Li, A. G. *et al.* Elevation of transforming growth factor beta (TGFbeta) and its downstream mediators in subcutaneous foreign body capsule tissue. *J. Biomed. Mater. Res. A* **82,** 498–508 (2007).

32. Wynn, T. A. Cellular and molecular mechanisms of fibrosis. *J. Pathol.* **214,** 199–210 (2008).

33. Hinz, B., Mastrangelo, D., Iselin, C. E., Chaponnier, C. & Gabbiani, G. Mechanical tension controls granulation tissue contractile activity and myofibroblast differentiation. *Am. J. Pathol.* **159,** 1009–20 (2001).

34. Gabbiani, G., Ryan, G. B. & Majne, G. Presence of modified fibroblasts in granulation

tissue and their possible role in wound contraction. *Experientia* **27,** 549–50 (1971).

35. Farokhzad, O. C. & Langer, R. Impact of Nanotechnology on Drug\nDelivery. *ACS Nano* **3,** 16–20 (2009).

36. Dalby, M. J. *et al.* Increasing fibroblast response to materials using nanotopography: morphological and genetic measurements of cell response to 13-nm-high polymer demixed islands. *Exp. Cell Res.* **276,** 1–9 (2002).

37. Teo, B. K. K. *et al.* The effect of micro and nanotopography on endocytosis in drug and gene delivery systems. *Biomaterials* **32,** 9866–75 (2011).

38. Solanki, A., Shah, S., Yin, P. T. & Lee, K.-B. Nanotopography-mediated reverse uptake for siRNA delivery into neural stem cells to enhance neuronal differentiation. *Sci. Rep.* **3,** 1553 (2013).

39. Tan, a. W., Pingguan-Murphy, B., Ahmad, R. & Akbar, S. a. Review of titania nanotubes: Fabrication and cellular response. *Ceram. Int.* **38,** 4421–4435 (2012).

40. Correa-Duarte, M. a. *et al.* Fabrication and biocompatibility of carbon nanotube-based 3D networks as scaffolds for cell seeding and growth. *Nano Lett.* **4,** 2233–2236 (2004).

41. Shalek, A. K. *et al.* Vertical silicon nanowires as a universal platform for delivering biomolecules into living cells. *Proc. Natl. Acad. Sci. U. S. A.* **107,** 1870–5 (2010).

42. McKnight, T. E. *et al.* Tracking Gene Expression after DNA Delivery Using Spatially Indexed Nanofiber Arrays. *Nano Lett.* **4,** 1213–1219 (2004).

43. VanDersarl, J. J., Xu, A. M. & Melosh, N. A. Nanostraws for direct fluidic intracellular access. *Nano Lett.* **12,** 3881–6 (2012).

44. Celli, A. *et al.* Tight junction properties change during epidermis development. *Exp. Dermatol.* **21,** 798–801 (2012).

45. Kirschner, N., Houdek, P., Fromm, M., Moll, I. & Brandner, J. M. Tight junctions form a barrier in human epidermis. *Eur. J. Cell Biol.* **89,** 839–842 (2010).

46. Roussel, A. J. J., Knol, A. C., Bourdeau, P. J. & Bruet, V. Optimization of an Immunohistochemical Method to Assess Distribution of Tight Junction Proteins in Canine Epidermis and Adnexae. *J. Comp. Pathol.* **150,** 35–46 (2014).

47. Furuse, M. *et al.* Occludin - a Novel Integral Membrane-Protein Localizing at Tight Junctions. *J. Cell Biol.* **123,** 1777–1788 (1993).

48. Fanning, A. S., Jameson, B. J., Jesaitis, L. A. & Anderson, J. M. The Tight Junction Protein ZO-1 Establishes a Link between the Transmembrane Protein Occludin and the Actin Cytoskeleton. *J. Biol. Chem.* **273,** 29745–29753 (1998).

49. Furuse, M., Fujita, K., Hiiragi, T., Fujimoto, K. & Tsukita, S. Claudin-1 and -2: Novel integral membrane proteins localizing at tight junctions with no sequence similarity to occludin. *J. Cell Biol.* **141,** 1539–1550 (1998).

50. Sugawara, T. *et al.* Tight junction dysfunction in the stratum granulosum leads to aberrant stratum corneum barrier function in claudin-1-deficient mice. *J. Dermatol. Sci.* **70,** 12–18 (2013).

51. Furuse, M. *et al.* Claudin-based tight junctions are crucial for the mammalian epidermal barrier: a lesson from claudin-1-deficient mice. *J. Cell Biol.* **156,** 1099–1111 (2002).

52. Deli, M. A. Potential use of tight junction modulators to reversibly open membranous

barriers and improve drug delivery. *Biochim. Biophys. Acta - Biomembr.* **1788,** 892–910 (2009).

53. Findley, M. K. & Koval, M. Regulation and roles for claudin-family tight junction proteins. *IUBMB Life* **61,** 431–437 (2009).

54. Tsukita, S. & Furuse, M. Pores in the Wall Claudins Constitute Tight Junction Strands Containing Aqueous Pores. *J. Cell Biol.* **149,** 13–16 (2000).

55. Madara, J. L. Regulation of the movement of solutes across tight junctions. *Annu. Rev. Physiol.* **60,** 143–159 (1998).

56. Tsukita, S. & Furuse, M. Occludin and claudins in tight-junction strands: leading or supporting players? *Trends Cell Biol.* **9,** 268–273 (1999).

57. Broderick, K. E. *et al.* Optimized In Vivo Transfer of Small Interfering RNA Targeting Dermal Tissue Using In Vivo Surface Electroporation. *Mol. Ther. — Nucleic Acids* **1,** e11 (2012).

58. Elsabahy, M. & Foldvari, M. Needle-free gene delivery through the skin: an overview of recent strategies. *Curr. Pharm. Des.* **19,** 7301–7315 (2013).

59. Brown, M. B., Traynor, M. J., Martin, G. P. & Akomeah, F. K. Transdermal drug delivery systems: skin perturbation devices. *Methods Mol. Biol.* **437,** 119–139 (2008).

60. Rao, R. & Nanda, S. Sonophoresis: recent advancements and future trends. *J. Pharm. Pharmacol.* **61,** 689–705 (2009).

61. Xia, H. *et al.* Low molecular weight protamine-functionalized nanoparticles for drug delivery to the brain after intranasal administration. *Biomaterials* **32,** 9888–9898 (2011).

62. Oh, D.-H., Chun, K.-H., Jeon, S.-O., Kang, J.-W. & Lee, S. Enhanced transbuccal salmon calcitonin (sCT) delivery: Effect of chemical enhancers and electrical assistance on in vitro sCT buccal permeation. *Eur. J. Pharm. Biopharm.* **79,** 357–363 (2011).

63. Gratieri, T., Gelfuso, G. M., de Freitas, O., Rocha, E. M. & Lopez, R. F. V. Enhancing and sustaining the topical ocular delivery of fluconazole using chitosan solution and poloxamer/chitosan in situ forming gel. *Eur. J. Pharm. Biopharm.* **79,** 320–327 (2011).

64. Polat, B. E., Hart, D., Langer, R. & Blankschtein, D. Ultrasound-mediated transdermal drug delivery: Mechanisms, scope, and emerging trends. *J. Control. Release* **152,** 330–348 (2011).

65. Sonaje, K. *et al.* Self-Assembled pH-Sensitive Nanoparticles: A Platform for Oral Delivery of Protein Drugs. *Adv. Funct. Mater.* **20,** 3695–3700 (2010).

66. Shofner, J. P., Phillips, M. A. & Peppas, N. A. Cellular evaluation of synthesized insulin/transferrin bioconjugates for oral insulin delivery using intelligent complexation hydrogels. *Macromol. Biosci.* **10,** 299–306 (2010).

67. Fischer, K. E. *et al.* Hierarchical nanoengineered surfaces for enhanced cytoadhesion and drug delivery. *Biomaterials* **32,** 3499–506 (2011).

68. Uskoković, V., Lee, P. P., Walsh, L. A., Fischer, K. E. & Desai, T. A. PEGylated silicon nanowire coated silica microparticles for drug delivery across intestinal epithelium. *Biomaterials* **33,** 1663–72 (2012).

69. Sjöström, T. *et al.* Fabrication of pillar-like titania nanostructures on titanium and their interactions with human skeletal stem cells. *Acta Biomater.* **5,** 1433–1441 (2009).

70. Lee, J. *et al.* The control of cell adhesion and viability by zinc oxide nanorods. *Biomaterials* **29,** 3743–3749 (2008).

71. Balaban, N. Q. *et al.* Force and focal adhesion assembly: a close relationship studied using elastic micropatterned substrates. *Nat. Cell Biol.* **3,** 466–472 (2001).

72. Besser, A. & Safran, S. A. Force-Induced Adsorption and Anisotropic Growth of Focal Adhesions. *Biophys. J.* **90,** 3469–3484 (2006).

73. Takagi, J., Petre, B. M., Walz, T. & Springer, T. A. Global conformational rearrangements in integrin extracellular domains in outside-in and inside-out signaling. *Cell* **110,** 599–511 (2002).

74. Dalby, M. J. Topographically induced direct cell mechanotransduction. *Med. Eng. Phys.* **27,** 730–742 (2005).

75. Biggs, M. J. P., Richards, R. G. & Dalby, M. J. Nanotopographical modification: a regulator of cellular function through focal adhesions. *Nanomedicine-Nanotechnology Biol. Med.* **6,** 619–633 (2010).

76. Shen, L. *et al.* Myosin light chain phosphorylation regulates barrier function by remodeling tight junction structure. *J. Cell Sci.* **119,** 2095–2106 (2006).

## Methods

### Fabrication of nanostructured surfaces

Fabrication of a mold for the nanostructured thin films was performed using electron beam lithography (JEOL JBX-9300FS EBL; Jeol Ltd., Tokyo, Japan). A nanostructured pattern was generated on a polymethylmethacrylate (PMMA) resist that had been spin casted onto an underlying silicon substrate. After developing away the PMMA resist, anisotropic reactive ion etching was employed to precisely etch the underlying silicon substrate, resulting in the nanofeatured molds shown in Figure 1. The mold was stamped into FDA-approved polypropylene or polystyrene thin films (25.4 mm; Premier Lab Supply, Inc., Port St. Lucie, FL). Briefly, the polystyrene or polypropylene film was placed in contact with the silicon mold and exposed to $T$=170°C and $P$=2 GPa using an Obducat 6-inch nanoimprint lithography system (Obducat, Lund, Sweden). Afterward, the mold was removed to reveal well-defined nanofeatures on the thin film.

### Contact angle measurements

Water contact angle measurements were performed with a goniometer to measure the wettability of the nanostructured surfaces. The nanostructured surfaces were thoroughly cleaned in a 99% isopropyl alcohol bath and then fully dried. A single drop of deionized (DI) water was placed on each nanostructured surface. The contact angle of the water droplet is the angle at which the liquid–vapor interface meets the solid–liquid interface and is the resultant between the adhesive and cohesive thermodynamic forces. As a droplet spreads over a surface, the contact angle decreases. Therefore, the contact angle is an inverse measure of the wettability of a surface. A

contact angle greater than 90 indicates that the wetting of the surface is thermodynamically unfavorable, so the fluid will minimize the surface contact and form a liquid droplet. Using this analysis, the contact angles of DI water were measured.

**Protein adsorption to nanostructured surfaces**

Nanostructured surfaces were cut into circular shapes with a 6-mm diameter biopsy punch and glued to the bottom of a 24-well plate (VWR, Brisbane, CA) with a silicone medical adhesive glue (Silastic Medical Adhesive Silicone Type A; Dow Corning, Midland, MI). After the glue dried, the thin films were thoroughly cleaned with 70% ethanol, followed by DI water overnight, and dried with compressed air. Solutions of FITC-IgG (Sigma-Aldrich, St. Louis, MO), FITC-BSA (Sigma-Aldrich), and fibrinogen-Alexa Fluor 568 (Life Technologies, Grand Island, NY), (each at a concentration of 0.1 mg/mL) were incubated on the nanostructured surface for 2 h. The thin films were rinsed with DI water and sonicated (Ultrasonic Bath Sonicator Model 75T; VWR) for 10 min at the default frequency. They were then mounted for visualization with a spinning disk confocal microscope (Ti-E Microscope; Nikon Instruments, Inc., Melville, NY, with a CSU-22 spinning disk confocal; Yokogawa Electric Corporation, Newnan, GA).

**Culture of cells on topographic nanostructured surfaces**

NIH 3T3 mouse fibroblasts were cultured in the DMEM high glucose (Gibco; Life Technologies) supplemented with 10% fetal bovine serum (HyClone, Logan, UT) and 100 IU/mL penicillin–streptomycin (Sigma-Aldrich). The cultures were incubated in an atmosphere containing 5% $CO_2$ and 90% relative humidity at 37°C. Growth media were exchanged every third day. The cells were subcultured at 90% confluency by trypsinization with

0.25% trypsin-EDTA. Cells from passage numbers between 160 and 170 were used for the experiments.

**Cyquant proliferation assay**

Six millimeter biopsy punches were used to cut the nanostructured thin films into a circular shape. The thin films were then glued to the bottom of the wells of 96-well plates (VWR) using the same glue as previously described. The films were disinfected with 70% ethanol overnight and air-dried in a CII safety cabinet. Fibroblasts were seeded at a density of 2000 cells/well and cultured over a 4-day time period. At 24, 48, 72, and 96 h, the media was aspirated and the plate was frozen at −80°C overnight. A cell pellet of 1 million cells was used for quantifying the number of cells that proliferated on the substrates. The cell pellet was serially diluted to generate a standard curve that ranged from 50 to 50,000 cells. The green fluorescent Cyquant dye was used to detect the number of cells for each time point (Cyquant Cell Proliferation Assays; Life Technologies). The signal was read on a fluorometer (SpectraMAX 190; Molecular Devices, Sunnyvale, CA) at a wavelength of 495 nm.

**Immunofluorescence staining of F-actin and cell area quantification**

Cells were fixed in 3.7% paraformaldehyde for 15 min and permeabilized with Triton X (0.1%) for 20 min. The F-actin was stained with phalloidin conjugated to Alexa Fluor 568 and diluted 1:40 in phosphate-buffered saline (PBS) for 30 min at 25°C (Life Technologies). The nucleus was stained with Hoechst 33258 at a dilution of 1:2000 for 30 min (Life Technologies). Samples were washed three times for 5 min in 1 mL PBS and mounted on a glass cover slip with hard mounting media (Vectashield; Vector Laboratories, Burlingame, CA) before inspection with

spinning disk confocal microscopy. Images were analyzed with ImageJ software that was downloaded from the National Institutes of Health (Image J, http://rsb.info.nih.gov/ij/). The images were imported into the software as an 8-bit grayscale sequence and then smoothed with brightness and contrast functions to enhance the features relative to the background. The threshold function was applied to create a binary image for particle analysis. ImageJ software detected the cell based on the binary image and calculated parameters such as circularity, cell area, perimeter, and aspect ratio. The data obtained from ImageJ were imported to Microsoft Excel for calculating means and standard deviations for circularity (0–1). Circularity was calculated using the equation, $4\pi(\text{area}/\text{perimeter}^2)$. A circularity value of 1.0 indicates a perfect circle and a value that approaches 0.0 is an increasingly elongated polygon, suggesting a more spread out cellular morphology.

**Scanning electron microscopy**

Fibroblasts were seeded onto the nanostructured thin films. On day 2, they were fixed with 3% glutaraldehyde in 0.1 M sodium cocadylate (pH 7.4), containing 0.1 M sucrose. After 45 min of incubation, the cells were rinsed with the cacodylate-sucrose buffer for 10 min. Next, the samples were dehydrated by gently adding solutions of ethanol in a graded series of concentrations (35%, 50%, 75%, 95%, 100%, and 100%) for 10 min each. The last step was to replace the 100% ethanol solution with HMDS, and then air-dried in the fume hood for 30 min. The samples were then sputter coated with 200 angstroms of gold–palladium and then imaged on a Hitachi S-5000 scanning electron microscope.

**Quantitative polymerase chain reaction methods**

The following films were cut into 6-mm circular shapes and glued as previously described: the homogeneous low aspect ratio substrate S(0.5, 1.4, 3.4), the highest aspect ratio substrate P(20), P(flat), S(flat), or tissue culture polystyrene (TCPS). 3T3 cells were seeded at a density of 5000 cells/cm$^2$ in a 96-well tissue culture plate. After 72 h, cells were lysed, reverse transcription was performed, and quantitative polymerase chain reaction (qPCR) (StepONEPlus; Applied Biosystems, Life Technologies) was performed using the Fast SYBR Green cells to $C_T$ kit in accordance with the manufacturer's instructions (Life Technologies). The experiment was carried out in triplicate ($n$=3) and the evaluation of mRNA expression by qPCR was also run in triplicate. The expression of *GAPDH*, collagen type 1 alpha 2, collagen type 3 alpha 1, connective tissue growth factor (*CTGF*), epidermal growth factor (*EGF*), integrin linked kinase (*ILK*), and transforming growth factor β1 (TGF-β1) were analyzed. The real-time polymerase chain reaction (PCR) results were analyzed using the Livak method and normalized to *GAPDH* transcript levels.[17] The primer sequences that were used are as follows: the *GAPDH* forward was 5′-CTC TCT GCT CCT CCT GTT CG-3′ and *GAPDH* reverse was 5′-GCC CAA TAC GAC CAA ATC C-3′. The collagen type 1 alpha 2 primer sequences in the forward and reverse directions were AAG GGT GCT ACT GGA CTC CC and TTG TTA CCG GAT TCT CCT TTG G, respectively. The collagen type 3 alpha 1 primer sequences in the forward and reverse directions were CTGTAACATGGAAACTGGGGAAA and CCATAGCTGAACTGAAAACCACC, respectively. The *ILK* primer sequences in the forward and reverse directions were CACGGCAATGTGCCACTTC and GCTCACAAGAGCCCCGTTAG, respectively. The *EGF* primer sequences in the forward and reverse directions were AGCATCTCTCGGATTGACCCA and CCTGTCCCGTTAAGGAAAACTCT, respectively. The *TGF-β1* primer sequences in the

forward and reverse directions were CTTCAATACGTCAGACATTCGGG and GTAACGCCAGGAATTGTTGCTA, respectively. And finally, the *CTGF* primer sequences in the forward and reverse directions were GGGCCTCTTCTGCGATTTC and ATCCAGGCAAGTGCATTGGTA, respectively.

**Statistical analysis**

Data are reported as mean value±standard deviation. Multiple comparisons were analyzed with a one-way ANOVA test followed by the Holm-Sidak *t*-test. *p*-values of less than 0.05 were considered statistically significant. For the proliferation data, each group had an $n$=6, and for the gene expression data, each group had an $n$=3 with a technical replicate of $n$=3.

**Film and device fabrication**

Nanostructured films are made, as previously described, by nanoimprint lithography whereby a thermoplastic is heated above its glass transition temperature and pressed into a silicon mold (*38*). Molds are fabricated by electron beam lithography, allowing for precise design of submicron structures. This method has allowed the fabrication of thin films with varying nanotopographies. Films used in the in vivo studies were the highest performer in prior drug delivery studies and are made from polyether ether ketone (PEEK) with nanocolumns of three different lengths and widths: 1um length - 360-370nm width; 400nm length - 158-170nm width; and 200nm length - 80-115nm width. For the in vitro studies, a simple topography composed of PEEK or polypropylene nanocolumns measuring 300 nm high and 200 nm wide was used. These films were used for *in vitro* studies because they were similarly high performing as the *in vivo* topography and offered a simple baseline design from which to iterate future studies to isolate nanostructure parameters.

The *in vivo* devices are made of an impermeable backing, a reservoir for a drug solution, a rate-controlling membrane, and silicon microneedle array (MNA) with or without a nanostructured film. The MNA is made up of 200 μm long, 90 μm wide microneedles with a pitch of 400 μm and a density of about 750 needles per square cm. The MNA is 25 mm by 25 mm and the entire device is 45 mm by 45 mm including the adhesive zone to affix the device to the skin. Using heat, the nanostructured thin films are vacuum sealed onto the MNA.

**In vivo drug delivery**

The nanostructured surfaces were integrated into a 25 mm by 25 mm transdermal microneedle patch for *in vivo* drug delivery studies in a rabbit model. 11 New Zealand White healthy rabbits weighing approximately 4 kg were used. Each animal was closely clipped to remove the fur in the left flank region. The study consisted of 3 groups: (1) the subcutaneous injection group receiving 2.5 mg/animal (n=2), (2) the nanotopography-wrapped microneedles group receiving 1.875 mg/animal (n=5), and (3) the smooth microneedles group receiving 1.875 mg/animal (n=4). The *in vivo* test facility used for this animal study is registered with the United States Department of Agriculture to conduct research in laboratory animals and is AAALAC accredited. The study was reviewed and approved by the Facility's Institutional Animal Care and Use Committee (IACUC). Blood samples were drawn from an ear vein to measure the etanercept concentration in the blood serum at 0, 0.5, 2, 6, 24, and 48 hours. All animals were euthanized following collection of the last blood sample. Etanercept was assayed in duplicate samples from each serum collection using Human sTNF-receptor ELISA kit (R&D Systems, Minneapolis, MN) which has a minimum detectable dose of 0.6 pg/mL.

For the rat studies, 12 Sprague Dawley rats weighing approximately 450 g were used. Each animal was closely clipped and Nair hair removal product was applied to remove fur in the central

back region. The study consisted of three groups: (1) the nanotopography-wrapped microneedles group receiving 12.5 mg/animal (n=4), (2) the smooth microneedles group receiving 12.5 mg/animal (n=4), and (3) reservoir patch group receiving 12.5 mg/animal (n=4). ). The *in vivo* test facility used for this animal study is registered with the United States Department of Agriculture to conduct research in laboratory animals and is AAALAC accredited. The study was reviewed and approved by the Facility's Institutional Animal Care and Use Committee (IACUC). Blood samples were drawn from the tail vein to measure the etanercept concentration in the blood serum at 0, 8, 24, 36, 48, and 72 hours. All animals were euthanized following collection of the last blood sample. Etanercept was assayed in duplicate samples from each serum collection using Human sTNF-receptor ELISA kit (R&D Systems, Minneapolis, MN) which has a minimum detectable dose of 0.6 pg/mL.

**Primary human keratinocyte cultures**

Primary human keratinocytes were derived from healthy neonatal foreskin. Epidermis was dissociated from dermis with dispase, and keratinocytes were grown to confluency in human epidermal media without antibiotics (CellnTec Media CnT-PR) (Zen-Bio, Raleigh, NC). Upon reaching confluency, the cells were dissociated and seeded on transwell inserts to differentiate them into multilayered cultures. Cells were air-lifted on day 3 of transwell culture, and media was exchanged daily into the basolateral chamber (CellnTec media CnT PR-D) (Zen-Bio, Raleigh, NC).

**Stratified keratinocyte immunofluorescence staining**

Day 8 primary human keratinocytes were used for all immunofluorescence studies. Cells were exposed to no device, flat control film, or nanostructured film on the apical surface (air interface) for 24 hours. After 24 hours, the devices were removed, and cells were fixed for 10 minutes in

100% methanol at -20 degrees Celsius and then for 20 minutes in 4% paraformaldehyde at room temperature. After fixation, the membranes were paraffin embedded, sectioned, and placed onto glass slides. For staining, the slides were de-paraffinized, blocked with 4% bovine serum albumin (BSA) for 1 hour, and then incubated with primary antibody diluted in 4% BSA for 12 hours at 4 degrees Celsius. The following primary antibodies were used: mouse anti-claudin-1 (Invitrogen 374900, Carlsbad, CA) (1:200); rabbit anti-claudin-4 (Abcam ab53156, Cambridge, England) (1:200). Following incubation with primary antibody, the sections were washed with 1x phosphate buffered saline (PBS) and then incubated with secondary antibody diluted in 4% BSA for 1 hour at room temperature. The following secondary antibodies were used: rabbit Alexa 568 (1:500) and mouse Alexa 488 (1:500). Following incubation with secondary antibody, the sections were washed and protected with a cover slip.

For reversal studies, the device was removed after 24 hour exposure, the cells were fed new media, and fixation and staining were performed after another 24 hours in the same manner as outlined above.

**Caco-2 cell culture**

Caco-2 cells from the human intestinal line (American Type Culture Collection (ATCC), Manassas, VA) were cultured in MEM with Earle's BSS supplemented with 20% FBS, 1% penicillin-streptomycin, and 1% sodium pyruvate, in an atmosphere containing 5% $CO_2$ and 90% relative humidity at 37 degrees Celsius. The cells were subcultured at 90% confluency by trypsinization with 0.05% trypsin-EDTA.

**Caco-2 immunofluorescence and TEM**

Caco-2 cells were grown to confluency on Transwell inserts (BD Falcon, Franklin Lakes, NJ) until tight junctions formed as measured by TEER (World Precision Instruments, Sarasota, FL).

No film, a flat film, or a nanostructured film were placed in contact with the cell monolayer. After two hours in contact with the films, immunofluorescence samples were fixed with 3.7% paraformaldehyde (PFA) for 15 minutes at room temperature. Samples were blocked and permeabilized with a solution of 1% BSA with 0.1% Triton-x in a phosphate buffer solution (PBS) for one hour at room temperature. The samples were incubated with a primary antibody: mouse anti-claudin-1 (Santa Cruz Biotechnology XX7, Santa Cruz, CA) (1:200), rabbit anti-claudin-4 (Abcam ab53156, Cambridge, England) (1:200), mouse anti-occludin (33-1500 Invitrogen, Carlsbad, CA) (1:100), rabbit anti-pFAK (Life Technologies 44-6246, Carlsbad, CA) (1:100), FITC conjugated mouse anti-vinculin (Sigma F7053, St. Louis, MO) (1:100), rabbit anti-pMLC (Cell Signaling Technologies 3671S, Danvers, MA) (1:50), rabbit anti-integrin beta1 (Abcam AB52971, Cambridge, England) (1:100), or rabbit anti-ZO-1 (Invitrogen 40220, Carlsbad, CA) (1:100) at 37 degrees Celsius for 1 hour. After washing with PBS, a secondary antibody solution goat anti-rabbit Alexa 488 (Life Technologies A11008, Carlsbad, CA) (1:100) or goat anti-mouse Alexa 488 (Life Technologies A11029, Carlsbad, CA) (1:100), and rhodamine phalloidin (Life Technologies R415, Carlsbad, CA) (1:40) was added for 1 hour at 37 degrees Celsius. The samples were then mounted with vectashield HardSet mounting medium with DAPI (Fisher Scientific, Waltham, MA) for imaging with a Nikon FN-1 Microscope (Melville, NY).

Samples for TEM were fixed in 2.5% glutaraldehyde (EM grade) in PBS solution for 1 hour at room temperature. Samples were dehydrated with 25%, 50%, 70%, 95%, then 100% ethanol solutions. For resin infiltration, samples were incubated with 1:1 solution of 100% ethanol and Epon resin for one hour, then incubated, covered, overnight in pure Epon resin. To embed samples, samples were placed in fresh epon resin and put in an oven at $60^0$ C for two days. Samples were imaged on a H-7500 TEM (Hitachi, Los Angeles, CA).

**TEER and drug delivery studies**

Caco-2 cells were grown to confluency on transwell inserts (BD Falcon) until tight junctions formed as measured by TEER (World Precision Instruments, Sarasota, FL). Cells were incubated with 2 mg/mL RGDS peptide, mouse anti-integrin beta1 (Millipore MAB2253, Temecula, CA) (1:25) and anti-integrin alphaV (Millipore MAB2021Z, Temecula, CA) (1:5), or 330 μM MLCK inhibitor peptide 18 (aka PIK) (Millipore 475981, Temecula, CA) for one hour at 37 degrees Celsius. No film, a flat film, or a nanostructured film were then placed in contact with the cell monolayer and FITC-BSA (Sigma, St. Louis, MO) was added to the apical chamber to a final concentration of 0.1 mg/mL. The basolateral chamber was sampled at time points and the amount of FITC-BSA transported was measured on a UV-vis spectrophotometer or the TEER was measured. After the final time point, MLCK treated samples were then fixed and stained as above for microscopy.

**Statistical analysis**

Data are reported as mean values +/- standard deviation. Multiple comparisons were analyzed with a one-way ANOVA test followed by the Holm t-test. P-values of less than 0.05 were considered statistically significant

SUPPLEMENTAL INFORMATION

Caco2 cells were seeded at a density of 50,000 cells in a 96-well tissue culture plate. The nanostructured and unimprinted thin films were placed in contact with the cells for 2 hours at 37°C (see Supplemental information). Cell lysis, reverse transcription (Eppendorf), and qPCR (Applied Biosystems, StepONEPlus) were performed using the Fast SYBR Green kit in accordance with the manufacturer's instructions. The experiment was performed in triplicate (n=3) and the evaluation of mRNA expression by qPCR was also performed in triplicate. The

expression of GAPDH (forward 5’ CTCTCTGCTCCTCCTGTT CG-3’, reverse 5’-GCCCAATACGACCAAATCC-3’), ZO-1 (forward 5’- TGTGAGTCCTTCAGCTGTGG-3’, and reverse 5’- TTTCCTGCTCAACTCCTTCG-3’), ocln (forward 5’-ACCGAATCATTATGCACCAAGC-3’, reverse 5’- AGATGGCAATGCACATCA CAA-3’), MLCK (forward 5’- CCCGAGGTTGTCTGGTTCAAA-3’, reverse 5’-GCAGGTGTACTTGGCATCGT-3’), and FAK (forward 5’- GGCCTGCTTTGGATTCCG C-3’, reverse 5’- CAGTGAACCTCCTCTGACCG-3’) were analyzed.

# Chapter 3 – The effect of nanotopography on modulating protein adsorption and the fibrotic response


## Abstract

Understanding and modulating the cellular response to implanted biomaterials is crucial for the field of tissue engineering and regenerative medicine. Since cells typically reside in an extracellular matrix containing nanoscale architecture, identifying synthetic nanostructures that induce desirable cellular behaviors could greatly impact the field. Using nanoimprint lithography, nanostructured patterns were generated on thin film polymeric materials. The ability of these surfaces to influence protein adsorption, fibroblast proliferation and morphology, and fibrotic markers was investigated. Nanostructured features with aspect ratios greater than five allowed for less protein adsorption, resulting in decreased fibroblast proliferation and rounded cellular morphology. These nanofeatures also induced significantly lower gene expression of collagen 1α2, collagen 3α1, and growth factors such as connective tissue growth factor, integrin linked kinase, transforming growth factor β1 (TGF-β1), and epidermal growth factor, key factors associated with a fibrotic response. The results demonstrate that select nanostructured surfaces could be used to modulate the fibrotic behavior in cells and have the potential to be used as antifibrotic architecture for medical implants or tissue engineering scaffolds.


## Introduction

Implant-induced fibrosis has generated much attention in the medical community and in the field of tissue engineering. Almost all soft tissue implants undergo fibrotic encapsulation and eventual loss of functional tissue in the vicinity surrounding the implant. The fibroblast is a specific cell that synthesizes and deposits the extracellular matrix (ECM), forming the structural network for

soft tissue. Although it plays a critical role in wound healing, the over-proliferation of fibroblasts and the subsequent overproduction of ECM proteins have been implicated in fibrosis. It is well known that implant fibrosis and fibrotic encapsulation can often contribute to medical device failures, ranging from breast implant contracture to biosensor inactivation.[1–3] Fibrosis has also been implicated in postsurgical adhesions, contributing to the failure of gastrointestinal, gynecological, and sinus surgeries.[4]

To this end, new biomaterial interfaces that foster an antifibrotic environment must be developed. Previously, there has been considerable work on chemistry-based approaches for decreasing fibrosis. For example, Risbud *et al.* reported how biocompatible hydrogels composed of chitosan-pyrrolidone arrest capsular fibroblast growth.[5] Other materials such as alginate, hyaluronic acid, and derivatives of chitin have been demonstrated to mimic fetal wound healing by selectively inhibiting fibroblast growth.[6,7] Recently, however, it has been established that cells are capable of responding to nanotopographical cues found in their microenvironment. The ECM is composed of complex architectural features at the nanoscale, including pores, fibers, ridges, and protein band periodicities of ∼60 nm.[8] Nanoscale features, being at the subcellular size scale, have the ability to influence cellular behaviors such as morphology, proliferation, and differentiation.[9–11] Therefore, nanotopography offers the opportunity to perturb a wide range of cellular responses. A better understanding of the cell–material interface on the nanoscale enables the exploration of a spectrum of interactions that are crucial to designing advanced medical devices and implants. Herein we report how nanostructured biomaterials can be used to generate an antifibrotic environment for cells.

To investigate how nanotopography influences cellular behavior, nanostructures must be fabricated with a high level of repeatability and precision. Current advancements in nano- and microtechnology offer new possibilities of probing cell–material interactions to better understand biological functions.[12,13] Ranging from microcontact printing to photolithography, there are various techniques for systematically controlling topographical features. One such fabrication technique to achieve nanofeatures is nanoimprint lithography (NIL). This technique is a stamping process capable of generating nanometer length patterns as small as 10 nm.[14,15] In contrast to conventional photolithography, nanofeatures are generated by the mechanical deformation of a thermoplastic material using a mold with nanofeatures. Molds are fabricated using electron beam lithography to overcome the diffraction limit of light and to produce features on the nanoscale.

The design of the nanostructured substrates was inspired by the ECM that surrounds soft tissue implants. Mimicking the ECM involved rationally designing structures that were similar to collagen, the most abundant ECM protein in the body. Collagen consists of staggered arrays of tropocollagen molecules that bind together to form fibrils. These collagen fibrils have diameters that range from 100 to 500 nm and lengths up to the millimeter length scale.[16] Despite significant research efforts over the past two decades, the effect of collagen fibril geometry on wound healing and fibrosis remains largely unknown. Herein we designed surfaces with arrays of nanopillars that have diameters ranging from 200 to 800 nm to capture the full breadth of collagen fibril diameters that are found in nature. Moreover, collagen and many other components of the ECM are hierarchical structures from the molecular length scale to the macroscopic length scale. Therefore, one of the substrates was designed to mimic the complex hierarchical structure of collagen by containing micron-sized features with two levels of

nanosized features. All four of the nanostructured substrates were designed to emulate the *in vivo* cross section of severed collagen fibers that results from soft tissue injury as a two-dimensional array of nanopillars. To this end, we utilized NIL to generate various nanostructured surfaces in two commonly used polymeric materials as a platform to examine how nanotopographical cues influence fibroblast behavior. Since cellular attachment and proliferation are mediated by protein adsorption to the underlying substrate, we hypothesized that nanostructured topography would influence protein adsorption, thereby affecting the fibrotic response.

## Results

### Nanofabrication

NIL was utilized to generate four unique nanostructured topographies as shown in Figure 1. The different substrates consisted of a polypropylene film with high aspect ratio nanopillars [height (H)=16 μm, diameter (D)=800 nm, aspect ratio (AR)=20, surface roughness=850 nm]; a polystyrene film with high aspect ratio nanopillars (H=1 μm, D=200 nm, AR=5, surface roughness=73 nm); a polystyrene film with a patchwork pattern of nanostructures (H=175 nm, D=200 nm, AR=0.88, surface roughness=9 nm); and finally, a polystyrene film with three different nanopillars combined in a hierarchical pattern with the largest pillar diameter of 1 μm having an average height of 520 nm, the medium pillar diameter of 400 nm having an average height of 560 nm, and the smallest pillar diameter of 200 nm having an average height of 680 nm. The ARs for the three structures were 0.5, 1.4, and 3.4, and the average surface roughness was 145 nm. All films will be referred to as either P or S for polypropylene or polystyrene, respectively, followed by the nanostructure aspect ratio in parentheses [e.g., “P(20)” encodes for the polypropylene film with a nanostructure aspect ratio of 20].

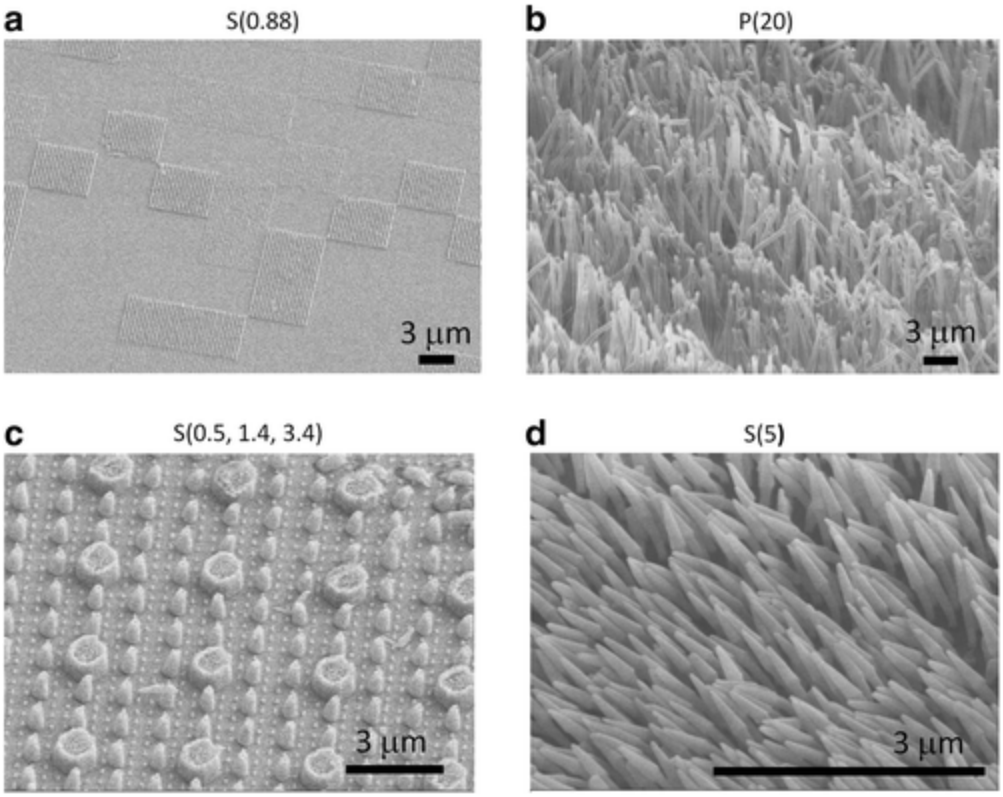


**Figure 1**

Nanoimprint lithography was employed to imprint the nanofeatures from nanofeatured molds into polystyrene or polypropylene thin films. Scanning electron microscopy (SEM) images reveal **(a)** a polystyrene thin film with features having an aspect ratio of 0.88, **(b)** a polypropylene thin film with features having an aspect ratio of 20, **(c)** a polystyrene thin film with hierarchical nanofeatures having aspect ratios of 0.5, 1.4, and 3.4, and **(d)** a polystyrene thin film with features having an aspect ratio of 5.

**Contact angle measurements and protein adsorption**

Characterization of hydrophobicity was performed through static water contact angle measurements. Figure 2 shows the contact angles in degrees for each nanostructured substrate. P(20) resulted in a higher contact angle compared with the P(flat) control. Similarly, the

polystyrene nanostructured S(5), S(0.5, 1.4, 3.4), and S(0.88) resulted in higher contact angles than the S(flat) control. Next, we tested the hypothesis that higher contact angles correlated with elevated protein adsorption levels. To test this hypothesis, we incubated the nanostructured substrates in solutions composed of proteins that are commonly found in blood to mimic the *in vivo* environment of blood-contacting medical device implants and biosensors. The blood protein solutions were composed of either FITC-BSA, FITC-IgG, or Alexa Fluor 568-Fibrinogen.[18] Next, the nanostructured substrates were imaged with confocal microscopy as shown in Figure 3. The nanotopography dramatically affects the way proteins adsorb to the various surfaces. For example, the higher aspect ratio features [S(5) and P(20)] seem to adsorb FITC-BSA, FITC-IgG, and fibrinogen only to the tips of the nanopillars. Interestingly, FITC-BSA and FITC-IgG adsorb to the tops of the micron-sized features as well as to the nanopillar tips of the hierarchical S(0.5, 1.4, 3.4) nanostructured thin film. However, fibrinogen appears to adsorb nonpreferentially on the S(0.5, 1.4, 2.4) surface. Furthermore, the heterogeneously patterned S(0.88) surface induced preferential protein adsorption in a quilt-like pattern for all three proteins.

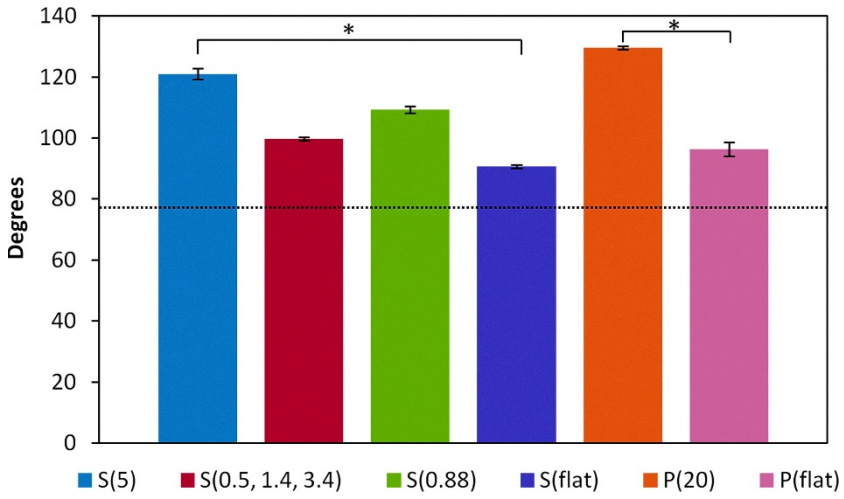


**Figure 2**

The water contact angle measurements demonstrate that the presence of nanofeatures on the polystyrene and polypropylene thin films increases the contact angles. This result translates into a more globally hydrophobic surface. *$p$<0.05.

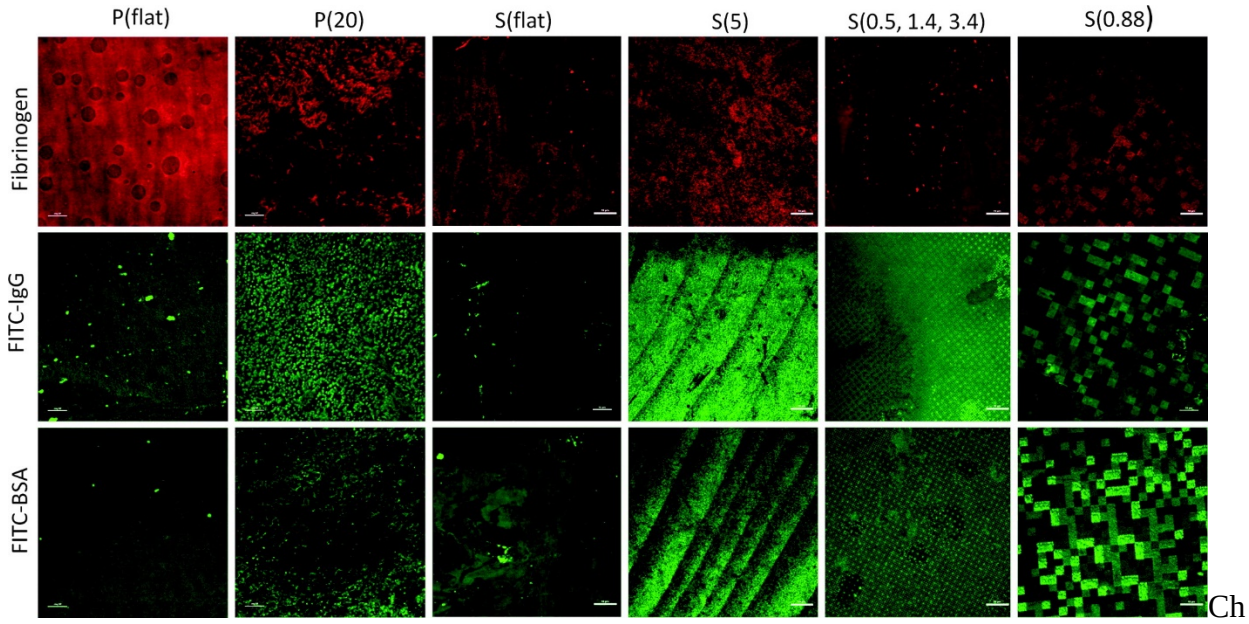


**Figure 3**

Alexa Fluor-Fibrinogen, FITC-IgG, and FITC-BSA were physisorbed onto the nanostructured and control surfaces. The proteins adsorbed to the surfaces in different patterns. Color images available online at www.liebertpub.com/tea

**Fibroblast proliferation**

Fibroblasts were cultured on the nanostructured substrates for 4 days and measured with the Cyquant cell proliferation assay at different time points to generate a cell proliferation curve. Figure 4 shows that fibroblasts grown on P(20) and S(5), the substrates with the highest aspect ratio features, seem to grow at the slowest rate. Additionally, observation of F-actin in the immunofluorescence staining showed different cell morphologies on the nanostructured surfaces compared to flat controls. As presented in Figure 5, the fibroblasts were well spread with many

stress fibers on the control flat substrates. However, the fibroblasts grown on P(20) and S(5) substrates were rounder and had fewer stress fibers. Quantitative analysis of cell morphology as measured by circularity confirmed what was observed qualitatively. Fibroblasts grown on the high aspect ratio P(20) and S(5) surfaces have statistically significantly ($p$<0.001) higher circularity values than those of the cells grown on low aspect ratio substrates, P(flat), S(flat), S(0.88), and S(0.5, 1.4, 3.4).

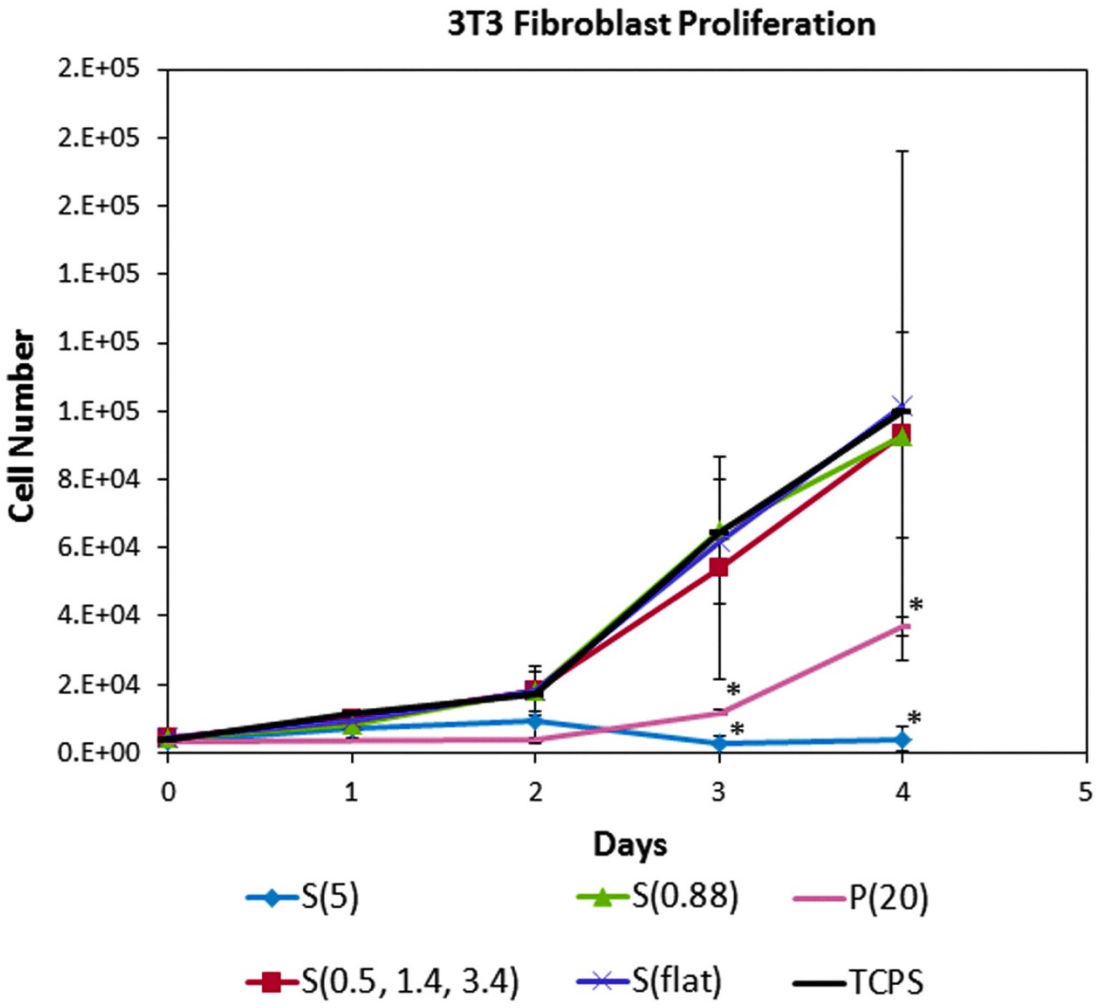


**Figure 4**

3T3 fibroblast proliferation was quantified with the Cyquant assay. Over 4 days, the fibroblasts grew significantly more slowly on the P(20) and the S(5) nanostructured surfaces compared to the other surfaces.

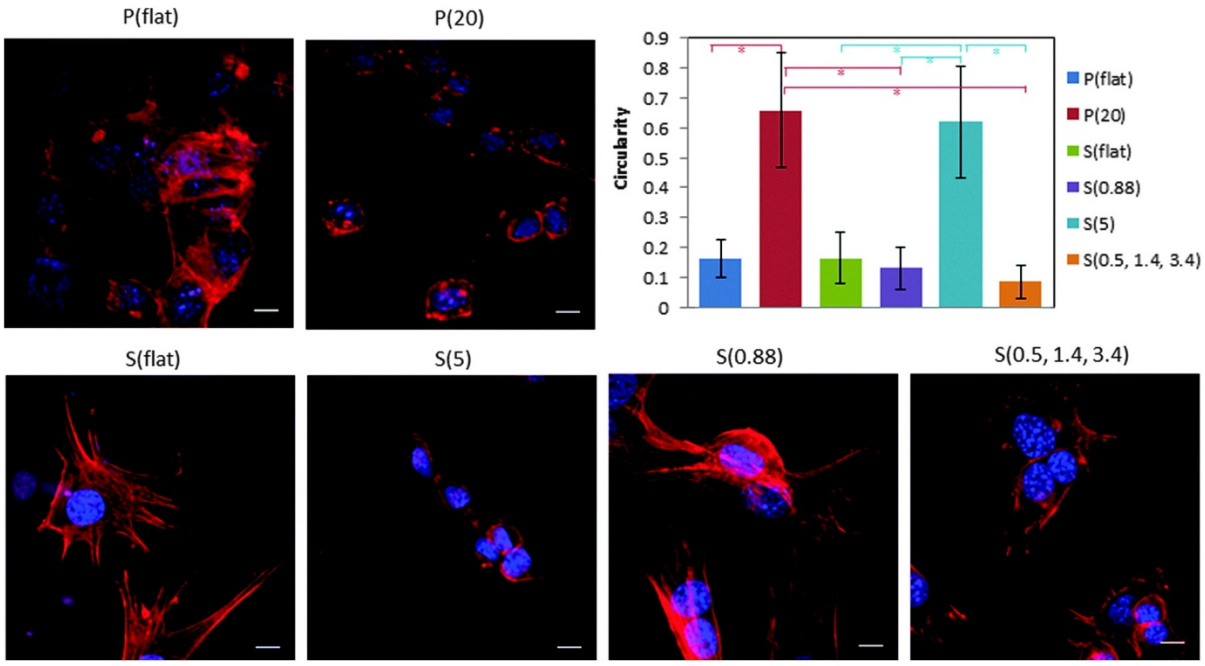


**Figure 5**

The fibroblast morphology indicates that the higher aspect ratio nanofeatures induce a rounded cellular morphology compared to the lower aspect ratio nanofeatures and the flat controls. The scale bars are 10 μm. The circularity values for the fibroblasts grown on high aspect ratio nanostructured surfaces [P(20) and S(5)] are significantly higher than those of the low aspect ratio nanostructured surfaces [P(flat), S(flat), S(0.88), S(0.5, 1.4, 3.4)]. The * symbol indicates $p<0.001$. This result indicates that the fibroblasts are unable to attach and spread on the high aspect ratio nanofeatures.

**Cell morphology**

Scanning electron microscopy (SEM) was employed to directly image the interactions of the filopodial projections with the nanofeatures. Fibroblasts grown on flat polypropylene (Fig. 6a) showed a typical, spread fibroblast shape. In contrast, fibroblasts grown on P(20) films (Fig. 6b) were more rounded. As seen with flat polypropylene, fibroblasts grown on flat polystyrene (Fig. 6c) were spread out with many filopodia. Fibroblasts on S(5) films (Fig. 6d) were more rounded like those on the P(20) film. In contrast, fibroblasts grown on the low aspect ratio polystyrene films, S(0.88) and S(0.5, 1.4, 3.4) showed a more typical fibroblast morphology (Fig. 6e, f). Interestingly, fibroblasts growing on the S(0.88) substrates preferentially grow on certain nanopatterned features. The fibroblasts exhibit star-like filopodial projections that adhere to the nanopatterned square patches. On S(0.5, 1.4, 3.4) films, fibroblasts seem to preferentially extend filopodia to taller structures (Fig. 1c).

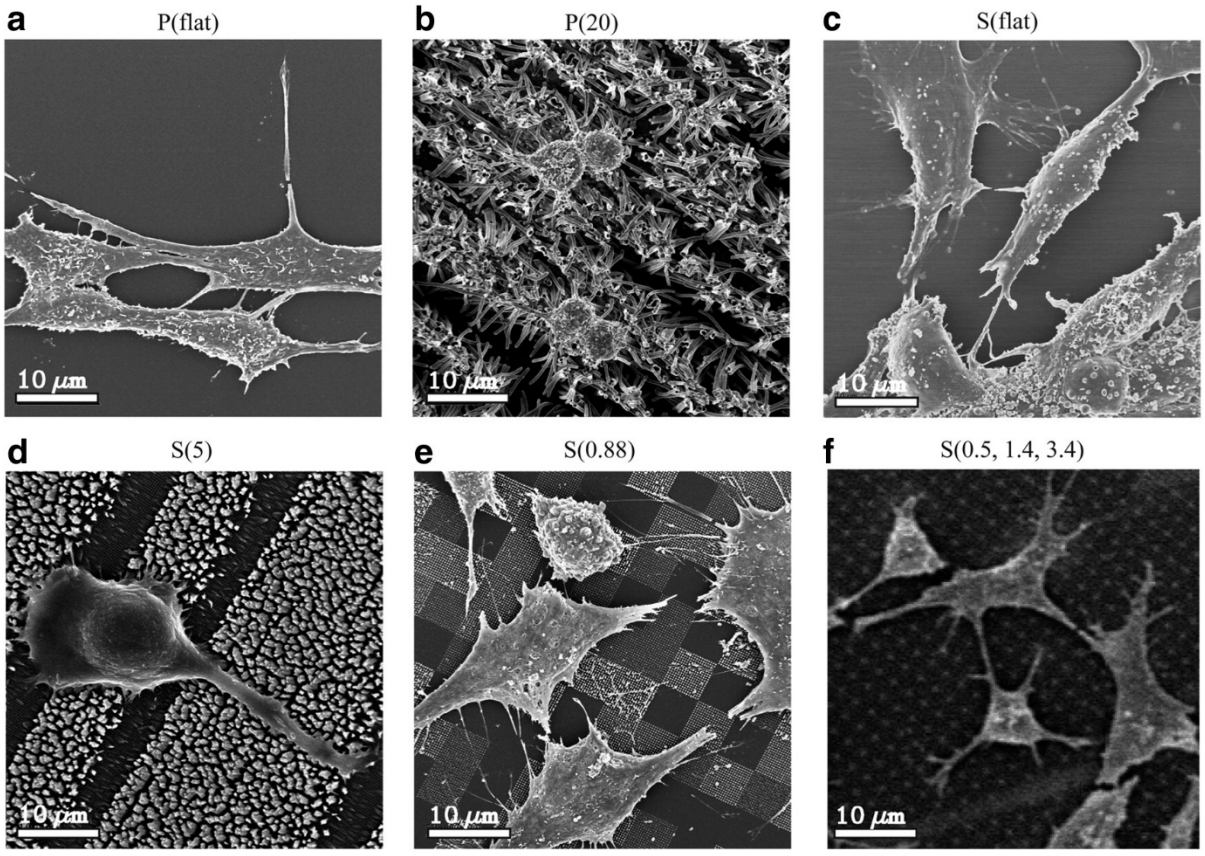

**Figure 6**

SEM images demonstrate how the fibroblasts are interacting directly with the nanostructures. **(a)** Fibroblasts grown on P(flat). **(b)** Fibroblasts grown on P(20). **(c)** Fibroblasts grown on S(flat). **(d)** Fibroblasts grown on S(5). **(e)** Fibroblasts grown on S(0.88). **(f)** Fibroblasts grown on S(0.5, 1.4, 3.4). Similarly to Figure 5, the P(20) and S(5) nanostructured surfaces induce a rounded morphology, indicating an antifibrotic environment. The scale bars are 10 μm.

**Gene expression**

Expression of the following six genes was measured by qPCR: collagen 1α2 (COL1α2), collagen 3α1 (COL3α1), CTGF, ILK, transforming growth factor β1 (TGF-β1), and EGF. The results indicate that P(20) elicits a significant down-regulation in fibrotic markers as shown in Figure 7. For example, the fibroblast gene expression of both COL1α2 (Fig. 7a) and COL3α1 (Fig. 7b) on P(20) are significantly downregulated compared to the lower aspect ratio S(0.5, 1.4, 3.4), unimprinted control, and TCPS control, suggesting an overall decrease in collagen production with high aspect ratio nanostructures. Similarly, CTGF, TGF-β1, and EGF growth factors responsible for the proliferative behavior of fibroblasts are substantially downregulated in the presence of the P(20) nanostructured surface.

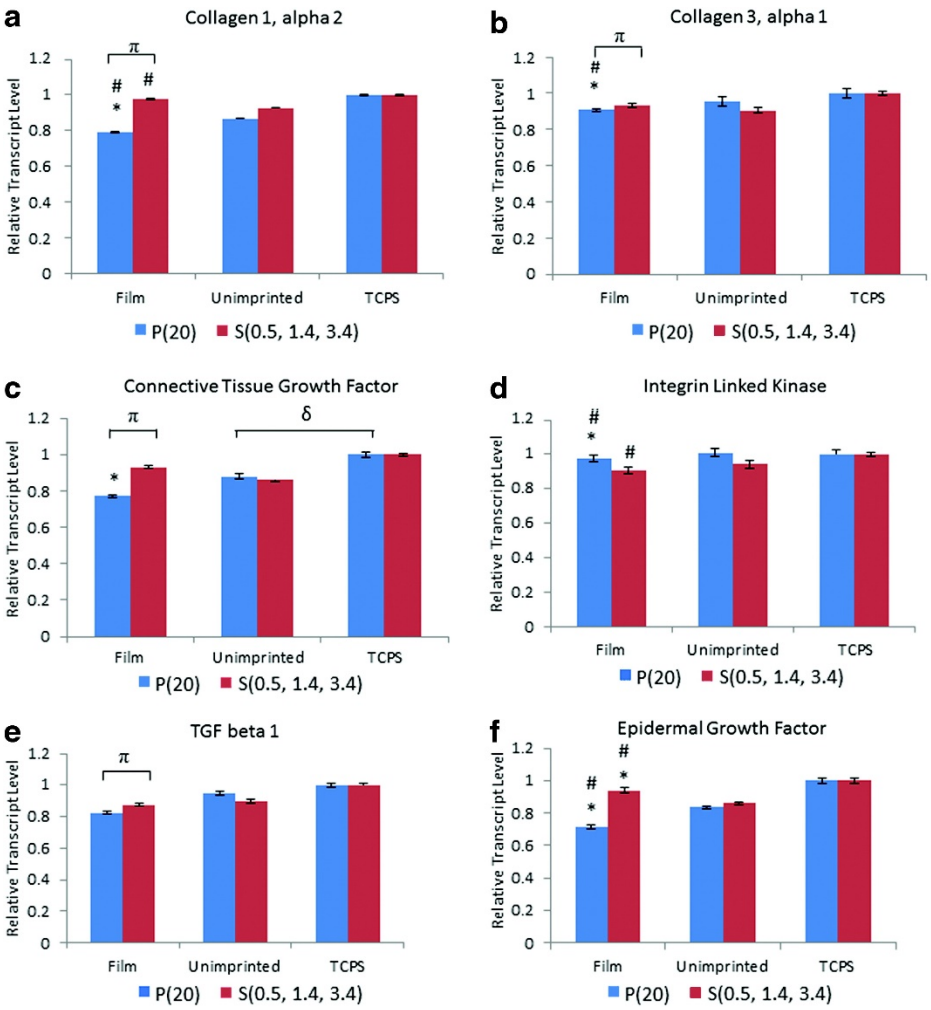


**FIG. 7.**

Gene expression studies for **(a)** collagen 1α2, **(b)** collagen 3α1, **(c)** connective tissue growth factor, **(d)** integrin linked kinase, **(e)** transforming growth factor β1, and **(f)** epidermal growth factor are displayed for P(20) and S(0.5, 1.4, 3.4). The * refers to a significant difference of $p<0.05$ between the film and the tissue culture polystyrene (TCPS) control, while the # corresponds to a significant difference of $p<0.05$ between the film and the unimprinted control group. π and δ refer to a significant difference of $p<0.05$ between P(20) and S(0.5, 1.4, 3.4) films and unimprinted control and TCPS control, respectively.

## Discussion

The ECM is a hierarchical environment containing microscale to nanoscale features ranging from microns to tens of nanometers in length. Fibroblasts in a wound site interact with clusters of severed collagen fibrils in an inhomogeneous pattern, and they may perceive this environment as surfaces containing nano- and microgrooves, ridges, and pillars with variable densities and roughnesses. A better understanding of the role that nanotopographical cues have on the fibrotic phenotype is important to the development of implanted materials.

In this study, we demonstrated how nanostructure-mediated cues elicit a dramatic effect on protein adsorption, cell shape, proliferation, and gene expression, with potential applications for decreasing fibrosis *in vivo*. We tested four different nanostructured surfaces and discovered that surfaces with higher aspect ratio features above five fostered an antifibrotic microenvironment. This result may be directly related to the surface structure or indirectly related to the way the surface topography influences ECM protein recruitment. The longer and thinner nanofeatures may resist protein adsorption due to steric hindrance and entropic repulsive forces.[19] Although others have observed differential cellular responses to nanotopography, most research has focused on cell–surface interactions and have not investigated the intermediate effect that nanostructures have on protein adsorption.[9,10,20–22] Unlike microtopography, whereby the cells are mechanically constrained between features, nanotopography may work by influencing how proteins are presented to cells. The adsorption of proteins to biomaterial surfaces is a dynamic process whereby proteins bind, rearrange, and detach. This process plays a crucial role in influencing cell growth, proliferation, and the overall incorporation of the biomaterial into the body. Depending on the shape of the nanofeature, the new surface energy may result in a more

hydrophilic or hydrophobic environment, which can lead to protein resistance or even protein denaturation in the extreme case. The results from Figure 2 indicate that regardless of material chemistry, nanotopography increases the contact angles of polystyrene and polypropylene, and therefore increases the hydrophobicity and surface energy of the thin films. P(20) and S(5) both have higher contact angles compared to the other surfaces. Perhaps, this superhydrophobic effect from the nanostructures may induce conformational denaturation of the adsorbed proteins, ultimately affecting the cell–materials interactions.[23] Without suitable protein presentation on the surface, the fibroblasts are less capable of attaching and maintaining healthy phenotypes.[24]

As we can see from Figure 3, the three blood proteins have drastically different adsorption patterns on the different surfaces. This is a striking result because it suggests that the nanostructure of the underlying surface influences the way proteins adsorb, which could be relevant to the surface properties of medical device implant materials. Interestingly, fibrinogen appears to adsorb to the same surface in a different way than FITC-IgG and FITC-BSA. For many of the surfaces, there are patches of no protein adsorption, particularly for P(20) and S(5). Fibrinogen is a much larger protein than IgG and BSA with a Stokes radius of 10.7 nm, twice the size of IgG (5.5 nm) and three times the size of BSA (3.4 nm).[25] Therefore, it may be difficult for the relatively larger fibrinogen molecules to conform to surfaces with high roughness such as in P(20) and S(5).

The various protein adsorption patterns strongly correlate to changes in phenotypic behaviors. For example, the nanotopographies of the surfaces may contribute to the different fibroblast morphologies that were observed by immunofluorescence and SEM. Interestingly, fibroblasts grown on P(20) and S(5) exhibited more rounded morphologies as quantified by circularity in

Figure 5. In contrast, cells grown on S(0.5, 1.4, 3.4), S(0.88), and the flat control surfaces displayed well-spread morphologies. Numerous studies in the literature have described a common trend of decreased cellular adhesion and spreading with an increase in nanofeature height.[26,27] This phenomenon is thought to be associated with perturbed focal adhesion formation, as well as an inhibition of protein adsorption. In our studies, we observed differential protein adsorption patterns on the various surfaces. The nanostructures that induced rounded cellular morphologies also had protein adsorption localized only to the tips of the nanopillars. This would suggest that the cellular filopodia could not find suitable sites of attachment due to the restriction of protein adsorption to the tips. Furthermore, this would indicate that the higher aspect ratio nanofeatures restrict integrin adhesion formation to the apexes of the nanopillars.

In this study, there are two mechanisms of action on the nanoscale that contribute to the fibroblast response to nanotopography: protein adsorption and substrate mechanics. In Figure 6, it is apparent that the low aspect ratio nanofeatures promote more interaction with the cells. S(0.5, 1.4, 3.4) has relatively low aspect ratio features, and we observed filopodia projections extending to the tips of the nanopillars. Filopodia tips are ∼100 nm and are the main sensory tools for spatial information.[28] Since the S(0.5, 1.4, 3.4) nanostructures have larger diameters that range from 200 nm to 1 μm, the fibroblasts were able to form intact focal adhesions to this surface.[7] Similarly, S(0.88) is another nanostructured surface with low aspect ratio features. Fibroblasts on this surface were well spread, and each filopodia appears to terminate on a region that has a high protein density. In contrast, it is apparent that the fibroblasts on P(20) and S(5) are pinned to the top of the nanopillars and unable to spread. It is well established that fibroblasts proliferate and form organized F-actin and stress fibers on higher moduli substrates.[29,30] To the perspective of a fibroblast, a low aspect ratio feature is locally stiffer than a high aspect ratio

feature due to the higher critical buckling load of a shorter and wider feature. These observations are consistent with the well-established fact that anchorage-dependent cells must attach and spread on an underlying substrate with a sufficient mechanical stiffness. Additionally, our study suggests that protein adsorption patterns to nanofeatures contribute to the cellular spreading as well.

Since focal adhesions link the cytoskeleton to the ECM through integrin clustering, it was hypothesized that the ability of the fibroblast to adhere and spread will alter cell signaling and mechanotransduction processes.[32] A potential explanation for the observed nanotopographical effects on fibroblast behavior could be the model of tensional integrity (tensegrity) developed by Ingber *et al.* in 1993.[31] In this model, integrins act as mechanoreceptors that transmit mechanical signals through the tensionally integrated cytoskeleton. The higher aspect ratio nanostructured substrates such as P(20) and P(5) have higher surface roughnesses, which may correspond to fewer cellular contact points for integrin engagement. Therefore, nanostructured surfaces that induce fewer and weaker focal adhesions may be associated with lower ECM production, proliferation, and gene expression since the reduced tension will lead to lower signal transduction to the nucleus.[25] Consistent with this hypothesis, P(20), the nanostructure with the highest aspect ratio features, induced lower gene expression levels for COL1α2, COL3α1, CTGF, TGF-β1, and EGF compared to the lower aspect ratio substrate, S(0.5, 1.4, 3.4). This decreased gene expression is in agreement with the significant reduction in cell growth observed on the same surface. COL1α2 and COL3α1 are significant components of scar tissue, so a downregulation in these genes suggests that this higher aspect ratio nanostructured surface could act as an antifibrotic interface.

Taken together, these results demonstrate that the aspect ratio and organization of nanotopographical cues influence fibroblast proliferation, cellular morphology, and expression of key fibrotic markers compared to flat control surfaces of the same material chemistry. The observed phenotypic effects are most likely due to altered protein adsorption to the nanofeatures. The proposed mechanism is through decreased focal adhesion formation and cell spreading. This work has broad applications for decreased scar formation around implanted biomaterials.

## Acknowledgments

We would like to thank Professor Ronald Fearing and the University of California, San Francisco Nikon center for their valuable insight and advice, Devin Brown and Nicole Devlin at the Georgia Tech Microelectronics Research Center for generating the NIL molds, Sunland Biotechnology for ELISA testing, and American Preclinical Services for the animal studies. Funding for this work was kindly provided by the Kimberly-Clark Corporation and the National Institutes of Health (NIH).

## References

1. Chegini N. Peritoneal molecular environment, adhesion formation and clinical implication. Front Biosci 7**,**e91, 2002

2. Hunter L.W., Lieske J.C., Tran N.V., and Miller V.M. The association of matrix Gla protein isomers with calcification in capsules surrounding silicone breast implants. Biomaterials 32**,**8364, 2011

3. Giurgiutiu V., et al. Electromechanical impedance sensor for *in vivo* monitoring the body reaction to implants. J Invest Surg 17**,**257, 2004

4. Schippers E., Tittel A., Ottinger A., and Schumpelick V. Laparoscopy versus laparotomy: comparison of adhesion-formation after bowel resection in a canine model. Dig Surg 15**,**145, 1998

5. Risbud M., Hardikar A., and Bhonde R. Growth modulation of fibroblasts by chitosan-polyvinyl pyrrolidone hydrogel: Implications for wound management? J. Biosci 25**,**25, 2000

6. Li Y., Rodrigues J., and Tomas H. Injectable and biodegradable hydrogels: gelation, biodegradation and biomedical applications. Chem Soc Rev 41**,**2193, 2012

7. Mast B.A., Diegelmann R.F., Krummel T.M., and Cohen I.K. Hyaluronic acid modulates proliferation, collagen and protein synthesis of cultured fetal fibroblasts. Matrix 13**,**441, 1993

8. Yim E.K.F. *et al.* Nanopattern-induced changes in morphology and motility of smooth muscle cells. Biomaterials 26**,**5405, 2005

9. Pennisi C.P., et al. Nanoscale topography reduces fibroblast growth, focal adhesion size and migration-related gene expression on platinum surfaces. Colloids Surf B Biointerfaces 85**,**189, 2011

10. Kim D.-H., et al. Mechanosensitivity of fibroblast cell shape and movement to anisotropic substratum topography gradients. Biomaterials 30**,**5433, 2009

11. Karuri N.W., Porri T.J., Albrecht R.M., Murphy C.J., and Nealey P.F. Nano- and microscale holes modulate cell-substrate adhesion, cytoskeletal organization, and -beta1 integrin localization in SV40 human corneal epithelial cells. IEEE Trans Nanobioscience 5**,**273, 2006

12. Qian T., and Wang Y. Micro/nano-fabrication technologies for cell biology. Med Biol Eng Comput 48**,**1023, 2010

13. Sharma G., et al. Polymer particle shape independently influences binding and internalization by macrophages. J Control Release 147**,**408, 2010

14. Chou S.Y., Krauss P.R., and Renstrom P.J. Imprint lithography with 25-nanometer resolution. Science 272**,**85, 1996

15. Chou S.Y., and Krauss P.R. Imprint lithography with sub-10 nm feature size and high throughput. Microelectron Eng 35**,**237, 1997

16. Gautieri A., Vesentini S., Redaelli A., and Buehler M.J. Hierarchical structure and nanomechanics of collagen microfibrils from the atomistic scale up. Nano Lett 11**,**757, 2011

17. Livak K.J., and Schmittgen T.D. Analysis of relative gene expression data using real-time quantitative PCR and the 2(-Delta Delta C(T)) method. Methods 25**,**402, 2001

18. Mabuchi K., et al. Changes with respect to time in the *in vivo* adsorption of plasma proteins onto artificial heart blood pumps. ASAIO J 38**,**M536, 1992

19. Rixman M.A., Dean D., Macias C.E., and Ortiz C. Nanoscale intermolecular interactions between human serum albumin and alkanethiol self-assembled monolayers. Langmuir 19**,**6202, 2003

20. Wood M.A., Bagnaninchi P., and Dalby M.J. The beta integrins and cytoskeletal nanoimprinting. Exp Cell Res 314**,**927, 2008

21. Dalby M.J. Cellular response to low adhesion nanotopographies. Int J Nanomedicine 2**,**373, 2007

22. Dalby M.J., Yarwood S.J., Johnstone H.J., Affrossman S., and Riehle M.O. Fibroblast signaling events in response to nanotopography: a gene array study. IEEE Trans Nanobioscience 1**,**12, 2002

23. Roach P., Farrar D., and Perry C.C. Interpretation of protein adsorption: surface-induced conformational changes. J Am Chem Soc 127**,**8168, 2005

24. Misra R.D.K., Girase B., Nune V.K.C., and Xu W. Cellular interactions and modulated osteoblasts functions mediated by protein adsorption. Adv Eng Mater 14**,**B247, 2012

25. Axelsson I. Characterization of proteins and other macromolecules by agarose gel chromatography. J Chromatogr A 152**,**21, 1978

26. Sjöström T., et al. Fabrication of pillar-like titania nanostructures on titanium and their interactions with human skeletal stem cells. Acta Biomater 5**,**1433, 2009

27. Lee J., Chu B.H., Chen K.-H., Ren F., and Lele T.P. Randomly oriented, upright SiO2 coated nanorods for reduced adhesion of mammalian cells. Biomaterials 30**,**4488, 2009

28. Yang C., and Svitkina T. Filopodia initiation: focus on the Arp2/3 complex and formins. Cell Adh Migr 5**,**402, 2011

29. Discher D.E., Janmey P., and Wang Y. Tissue cells feel and respond to the stiffness of their substrate. Science 310**,**1139, 2005

30. Hadjipanayi E., Mudera V., and Brown R.A. Close dependence of fibroblast proliferation on collagen scaffold matrix stiffness. J Tissue Eng Regen Med 3**,**77, 2009

31. Wang N., Butler J.P., and Ingber D.E. Mechanotransduction across the cell surface and through the cytoskeleton. Science 260**,**1124, 1993

32. Dalby M.J., et al. Nanotopographical stimulation of mechanotransduction and changes in interphase centromere positioning. J Cell Biochem 100**,**326, 2007

# Chapter 4 – *In vitro* drug delivery mediated by nanotopography

## Barrier function perturbed by nanowire coating of microspheres

Silicon nanowires grown on microspheres increase adhesion to intestinal epithelium and also increase drug loading capacity for oral drug delivery. Further investigation of the biological response of epithelium to the topographical cues presented by these nanowires demonstrated that, in addition to increased adhesion, barrier function of the epithelium was disrupted. In an intestinal cell line, Caco2, nanowires increased permeability, as measured by transport of fluorescein-Na, and decreased barrier function, as measured by transepithelial resistance (TER).[1] Specifically, the nanowires disrupted the tight junctions, the major determinant of paracellular permeability. We examined mRNA expression of genes involved with cytoskeletal remodeling and mechanotransduction signaling up stream of tight junction formation to investigate how cells were responding to the topographical cues presented by the nanowires.

The real-time quantitative RT-PCR data in Fig. 1 show that already after 2 hours of incubation a significant up-regulation of both *PKC* genes has occurred in cells incubated with NW and $NW_{PEG}$ (Fig 1 a,b). The overall up-regulation of *PKC* genes compared to both the control and cells treated with silica beads (B, $B_{PEG}$) was shown to be significantly more in cells treated with NW than in those incubated with $NW_{PEG}$. No statistically significant difference in the mRNA expression between $B_{PEG}$, $NW_{PEG}$ and the control was detected for *RhoA* and *Rac1* at any of the time points (data not shown). Only when the amount of NW particles added to the cells was quadrupled, *Rac1* turns out to be up-regulated, along with *CDC42* (Fig. 1c). After 4 h of incubation, the expression of both *PKC*s in cells incubated with NW and $NW_{PEG}$ becomes significantly higher compared to $B_{PEG}$ and the control; no statistical difference ($p < 0.05$) was

found between $B_{PEG}$ and the control. At the same time, while the expression of *RhoA* and *Rac1* in cells incubated with $NW_{PEG}$ is higher on average compared to $B_{PEG}$ and the control, the higher expression levels were not statistically significant. Although *PKC* genes affect the TJ by controlling the contraction of apical acto-myosin filaments and coordinating the assembly of adherens junctions, respectively[2], *RhoA* and *Rac1* regulate many processes related to mechanotransduction, including cell migration processes[3]. Since no cell movement was detected and the integrity of the cell layer was preserved even at highest particle dosages (20 mg per well) and incubation times (24 h), little detectable change in expression of these genes was observed. *PKC* genes, on the other hand, express proteins involved in regulating epithelial permeability by maintaining the fluidity of the TJ.[4] Up-regulated expression of both *PKC*-α and *PKC-z* levels may thus correspond to the observed alteration of the ZO-1 intensity around the TJ, suggestive of increased paracellular permeability. In general, the more fluid the membrane, the greater the expression of *PKC*-α[5], a principle which is consistent with our findings. These results suggest that an altered expression of proteins involved in the assembly of the epithelial TJ is responsible for variations in its fluidity and permeability. Finally, *CDC42* is a GTPase that regulates f-actin polymerization and depolarization and its up-regulation corresponds to the earlier observed cytoskeletal reorganization following treatments with all types of particles[1].

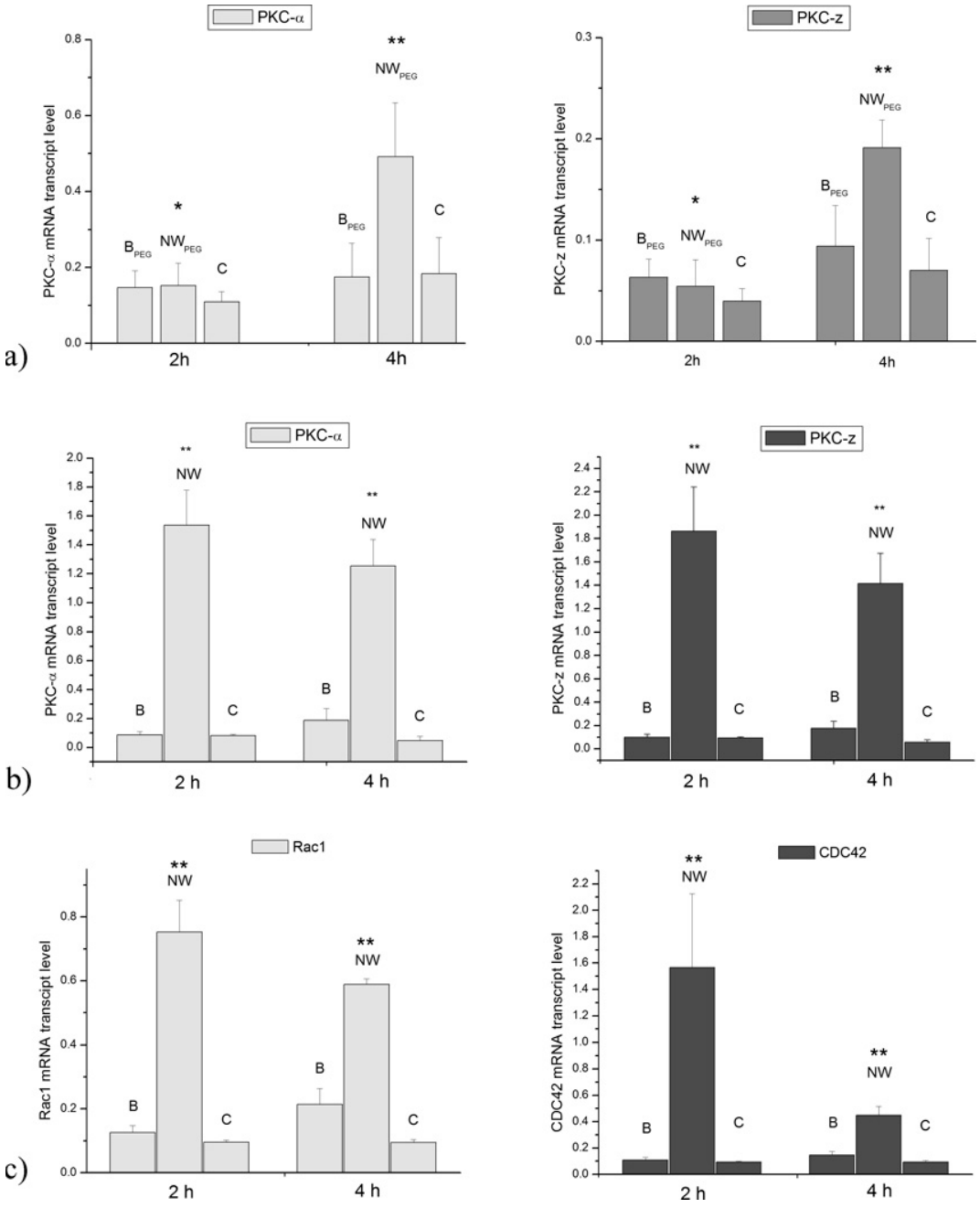


**Figure 1**

The effect of: (a) $B_{PEG}$ and $NW_{PEG}$ particles on the mRNA expression of *PKC*-α and *PKC-z*; (b) B and NW particles on the mRNA expression of *PKC-α* and *PKC-z*; (c) B and NW particles on the mRNA expression of *Rac1* and *CDC42*, all in Caco-2 cells. mRNA expression was detected

by quantitative RT-polymerase chain reaction relative to the housekeeping gene *GAPDH*. Data are shown as means with error bars representing standard deviation (* => $p < 0.05$; ** => $p < 0.0001$, with respect to the control group).

**Fabrication of Nanostructured Polymer Thin Films**

Inspired by the approach of using nanowires and therefore topography to modulate barrier function, we fabricated nanostructured thin films and examined them for the ability to modulate barrier function and drug delivery. Fabrication of a mold for the nanostructured thin films was performed using electron beam lithography (JEOL JBX-9300FS EBL). A nanostructured pattern was generated on a polymethylmethacrylate (PMMA) resist that had been spin-casted onto an underlying silicon substrate. After developing away the PMMA resist, anisotropic reactive ion-etching was employed to precisely etch the underlying silicon substrate, resulting in the nanofeatured mold shown in Figure 1. The mold was stamped into FDA-approved polypropylene (Premier Lab Supply Inc., 25.4 mm) through nanoimprint lithography (NIL) techniques, which is a facile and versatile process that allows for rapid patterning of large areas. This method allows for virtually any pattern to be generated at a resolution as small as 10 nm in a reproducible manner.[6,7] Therefore, virtually any kind of pattern can be fabricated to systematically investigate particular structural parameters such as pitch, diameter, height, aspect ratio, and so forth. Briefly, the polypropylene thin film was placed in contact with the silicon mold and exposed to T = 170 °C and P = 2 GPa using an Obducat 6-in. nanoimprint lithography system. Afterward, the mold was removed to reveal well-defined nanofeatures on a polypropylene thin film. Through scanning electron microscopy inspection, it was apparent that the features consisted of an array of nanopillars, each with an average height (H) of 300 nm, an average diameter (D) of 200 nm

(aspect ratio (AR) = 1.5), and a pitch spacing of 300 nm. The root-mean-square (rms) surface roughness of the nanostructured thin film was 47 nm, as measured utilizing atomic force microscopy. Another nanostructured thin film was fabricated that had higher AR nanopillars (H = 16 μm, D = 800 nm, AR = 20, surface roughness = 850 nm). These two nanostructured thin films were tested to investigate the effect of two different aspect ratios on drug transport. The two nanostructured thin films will be referred to as P(1.5) and P(20) where P represents polypropylene and the number inside the parentheses represents the AR of the nanopillars.[8]

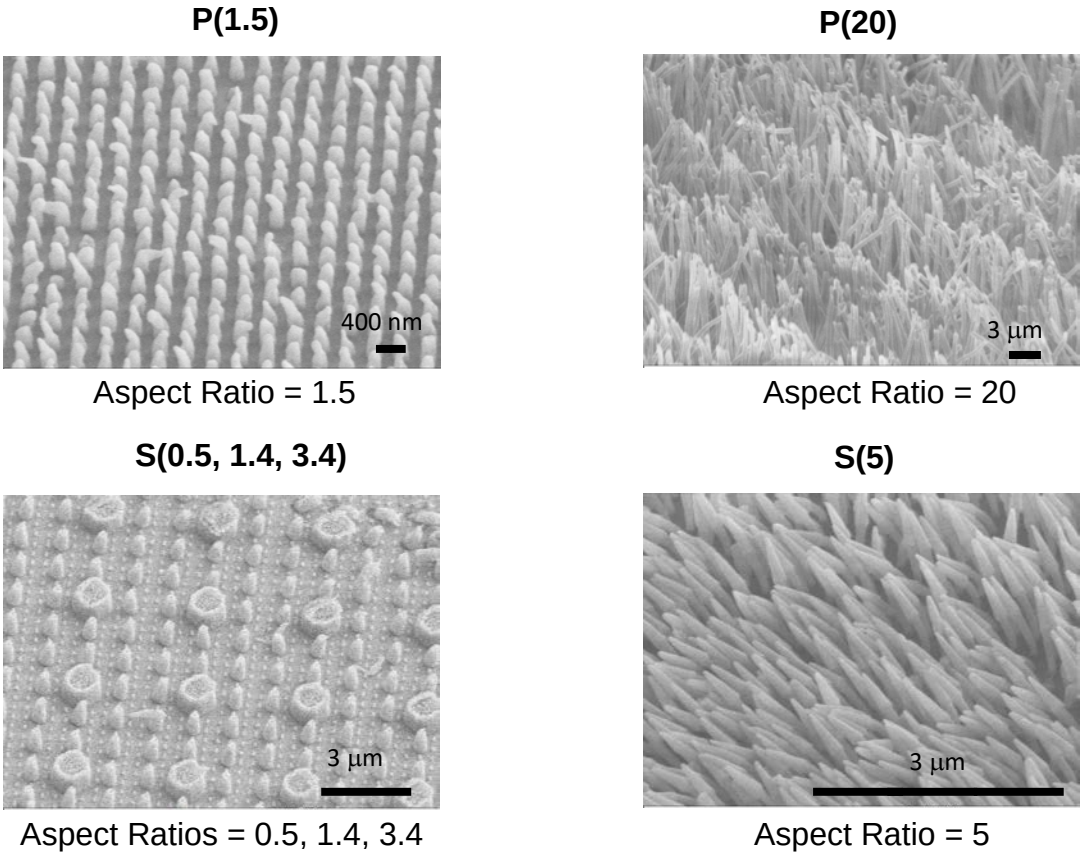


**Figure 2**

SEM images of nanostructured films. Films are named by the polymer, P for polypropylene and S for polystyrene, and the aspect ratio of the topographical features. Aspect ratio is the height divided by the width of the feature.

| | Height (nm) | Width (nm) | Aspect ratio | Roughness (nm) | Shear (MPa) |
|---|---|---|---|---|---|
| P(1.5) | 300 | 200 | 1.5 | 47 | 218 |
| S(0.5,1.4) | 1000;400;200 | 520;560;680 | 0.5;1.4;3.4 | 145 | 319 |
| S(5) | 1000 | 200 | 5 | 73 | 39 |
| P(20) | 16000 | 800 | 20 | 850 | 27 |

**Table 1**

Physical characteristics of nanostructured thin films.

**Nanotopographical cues do not increase transcellular transport**

Nanotopographical cues increase drug transport across caco-2 cells, a well-established epithelial drug delivery model owing to the formation of well-defined tight junctions. Figure 3 shows that when cells grown in a monolayer on a permeable transwell membrane insert (Fig. 3 d) are put in contact with low aspect ratio nanotopographical thin film, P(1.5), there is a statistically significant increase in drug delivery as measured by delivering drug to the apical chamber and sampling for drug in the basolateral chamber (Fig. 3 a-c). This increase is most markedly seen in

low aspect ratio nanotopography as compared to either high aspect ratio topography, P(20), which behaves similarly to flat, unimprinted polypropylene, and was seen for all three model drugs.

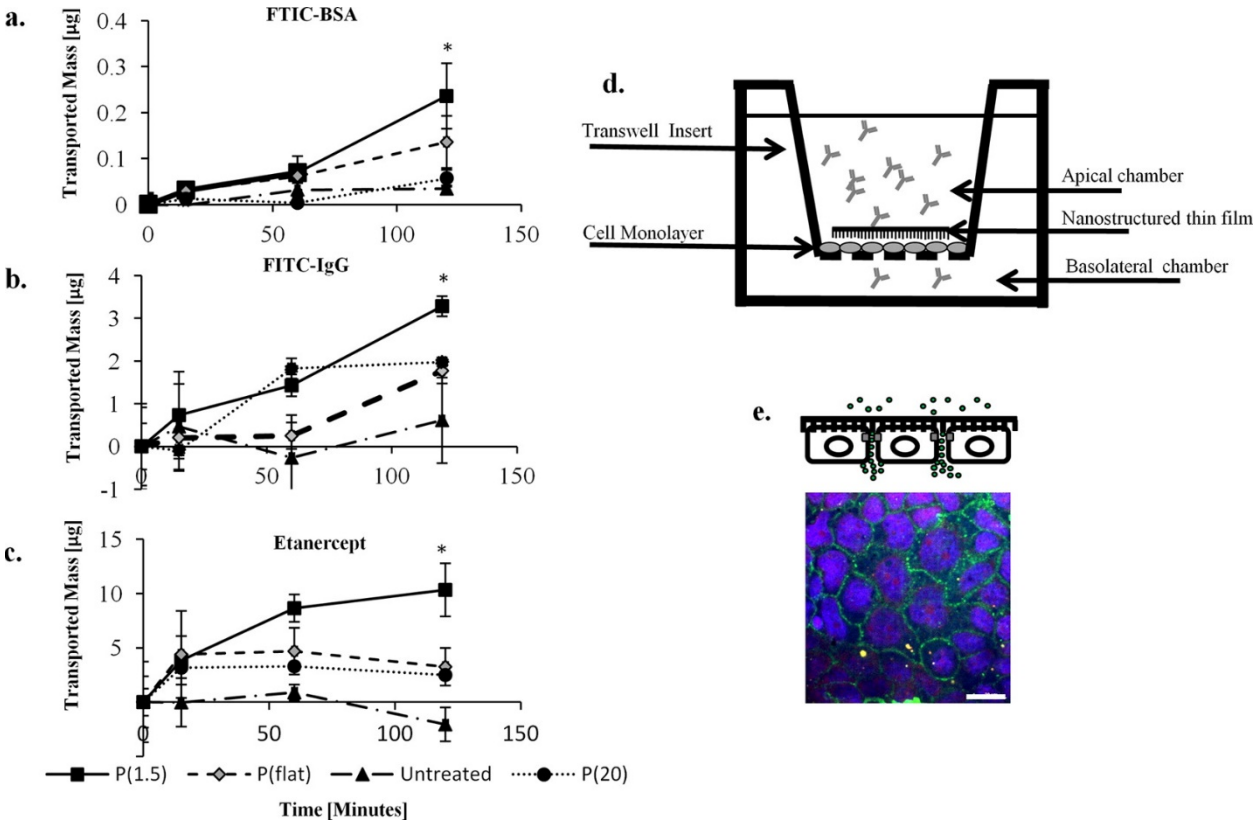


**Figure 3**

In vitro transport studies. Transport studies show that P(1.5) significantly enhances the transport of high MW species across the Caco-2 cell monolayers over 2 h. Data are displayed as the mean mass in micrograms (± standard deviation). Parts (a), (b), and (c) are the transport of FITC-BSA, FITC-IgG, and etanercept, respectively. Part (d) is a schematic of the transport study setup. The nanostructured thin film is placed directly in contact with the Caco-2 monolayer. The drug solution is placed in the apical chamber and is sampled (with PBS replacement) periodically

from the basal camber. (e) It appears that the IgG-FITC (green) is located around the Caco-2 cells (blue Hoechst) directly in the paracellular space. The scale bars represent 20 μm.[9]

Transepithelial drug delivery can be divided into two different mechanisms of crossing the cellular monolayer: transcellular whereby the therapeutic crosses through the cell and paracellular in which the drug passes through the junction between cells. We examined the expression of mRNA transcripts of genes related to either endocytosis and therefore transcellular transport, or the tight junction, a component of paracellular transport. Synaptotagmin-like protein 1 (sytl1) expression was upregulated 20 fold by nanotopography P(1.5) as compared to flat or cells alone (Figure 4). Sytl1 controls the spatial organization of actin at adherins junctions and also may play a role in vesicle trafficking. This implicates that nanotopography is possibly increasing drug transport by stimulating transcellular transport.

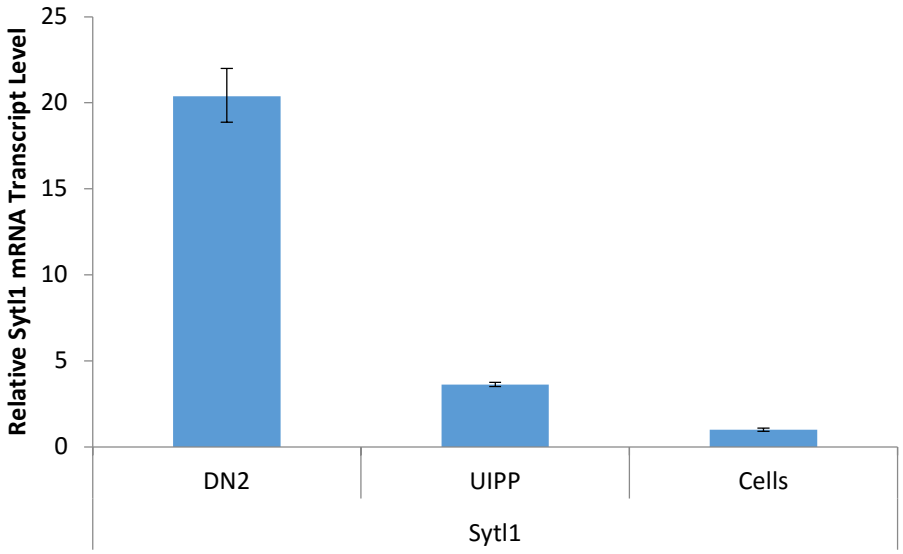


**Figure 4**

The effect of P(1.5) (DN2) or unimprinted polypropylene (UIPP) on the expression of sytl1 mRNA. Data is shown as means with standard deviation as error bars. Difference between P(1.5) and UIPP, and UIPP and cells are statistically significant ($p<0.05$).

To follow up the increase in expression of sytl1, caco2 cells were incubated with four different labeled model drugs: albumin, 10 kilo Dalton (kDa) dextran, 40 kDa dextran, and IgG. The number of caco2 cells endocytosing drug was examined by measuring the number of FITC positive cells by flow cytometry. Nanotopography had no effect on the number of FITC positive cells in all drug except for IgG where cells in contact with DN2 actually showed a decrease in the number of cells containing drug (Fig. 5). Since no difference was seen between cells in contact with nanotopography and cells in contact with UIPP, this suggests that transcellular transport is not the mechanism by which nanotopography increases drug transport.

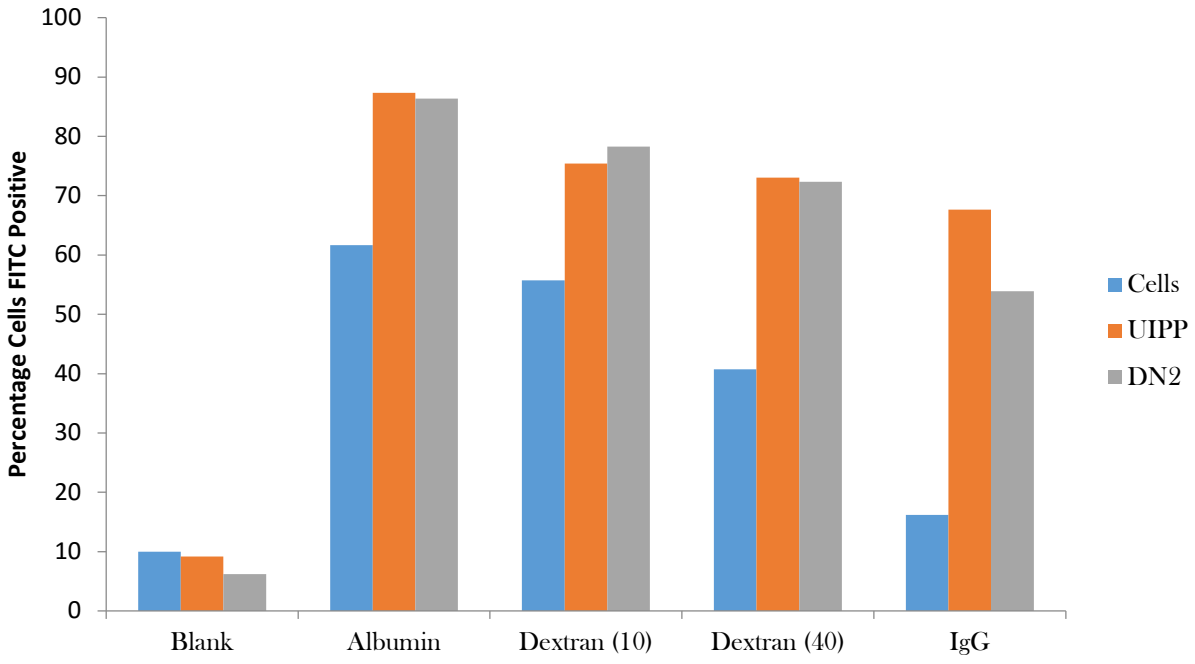

**Figure 5**

The effect of DN2, P(1.5), (blue) or unimprinted polypropylene (UIPP) (orange) on endocytosis of FITC labeled albumin, 10 kDa dextran (dextran (10)), 40 kDa dextran (Dextran (40)), and IgG as measured by percentage of FITC positive cells by flow cytometry. There is no difference in the extent of endocytosis of drug as a result of nanotopography, except a minor decrease with nanotopography contact for IgG.

To further investigate whether transcellular transport is involved in nanotopography mediated drug transport, the broad kinase inhibitor genistein was used to inhibit clathrin independent endocytic pathways.[10] When cells are put in contact with thin films, there is a decrease in transepithelial electrical resistance (TEER) whereby cells in contact with nanotopography show a greater decrease in TEER (Fig. 6, a). If an increase in endocytosis was responsible for the increase in permeability of epithelium in contact with nanotopography, it would be expected that treatment with genistein would prevent this drop in TEER. Regardless of whether cells were treated with genistein, a decrease in TEER was observed when the cells were in contact with nanotopography, further suggesting that paracellular, not transcellular transport is increased (Fig. 6, b).

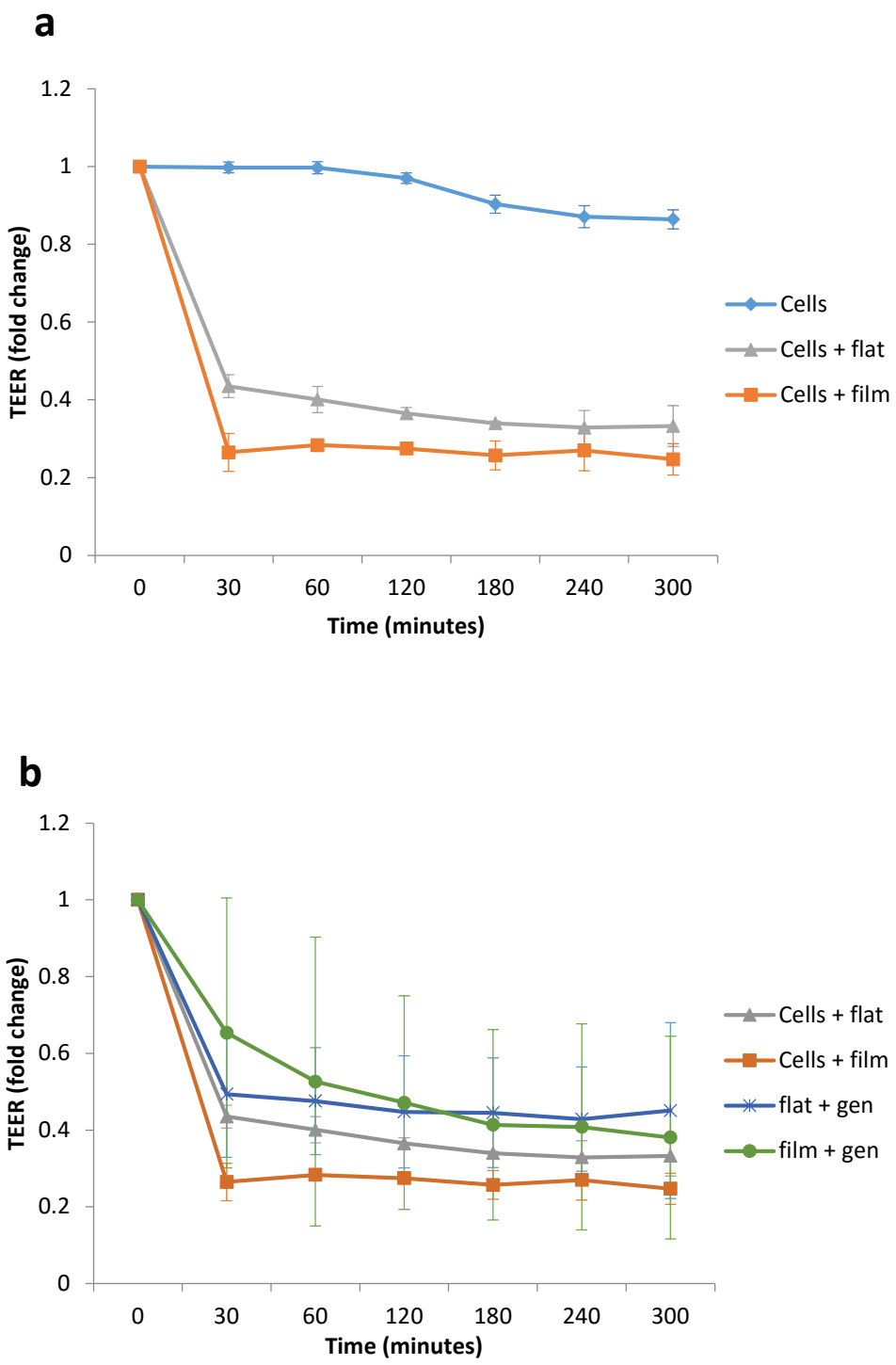
a
1.2
1
0.8
0.6
0.4
0.2
0
TEER (fold change)
0
30
60
120
180
240
300
Time (minutes)
Cells
Cells + flat
Cells + film
b
1.2
1
0.8
0.6
0.4
0.2
0
TEER (fold change)
0
30
60
120
180
240
300
Time (minutes)
Cells + flat
Cells + film
flat + gen
film + gen

**Figure 6**

Transepithelial electrical resistance fold change (a) of cells alone (blue diamonds), in contact with unimprinted polypropylene film (flat, gray triangles), or P(1.5) nanostructured film (film, orange squares). Cells in contact with P(1.5) has a greater magnitude decrease than cells in contact with UIPP film. (b) Fold change of TEER with and without genistein (gen) inhibitor treatment of cells in contact with either UIPP (flat) or P(1.5) film (film). Genistein inhibition of endocytosis does not prevent drop in TEER seen with application of nanostructured films.

**Nanotopographical cues increase drug transport by remodeling tight junctions**

To investigate the involvement of paracellular transport in nanotopography mediated transport, the expression of tight junction protein mRNA transcripts in cells in contact with nanotopography was measured. The expression of junctional adhesional molecule-1 (JAM-1) was slightly decreased by nanotopography (Figure 7). JAM-1 is an immunoglobulin-gene family protein that is involved in cell to cell adhesion in tight junctions.[11] Changes in transcript levels suggest a possibly involvement of paracellular permeability in nanotopography mediated drug transport. Therefore, further examination of expression of claudins, a class of transmembrane proteins in TJs that physically occlude the paracellular space and determine the permeability of the TJ. Examining three difference claudins, 2, 4 and 7 over 6 hours showed differences depending on the claudin. Claudin 2, a claudin expressed by epithelium with higher paracellular permeability, showed no difference between cells in contact with nanotopography, cells in contact with unstructured polypropylene, or cells alone (Figure 8, a). Claudin 4, a claudin expressed in less permeable epithelium, after an initial increase in expression after two hours in contact with either a nanostructured P(1.5) film or an UIPP (unimprinted polypropylene) film, was down regulated by nanotopography at both four and six hours. This implies a modulation of

paracellular permeability by nanotopography by remodeling of the tight junction (Fig. 8, b). Claudin 7 selectively increases paracellular permeability. When cells are in contact with nanotopography, there is no difference in mRNA expression levels after two and four hours, but there is a decrease in expression at 6 hours in both cells in contact with the nanostructured thin films and UIPP, suggesting that the decrease in expression is due to chemical or material properties common to both this films rather than a specific response to topography (Fig. 8, c).

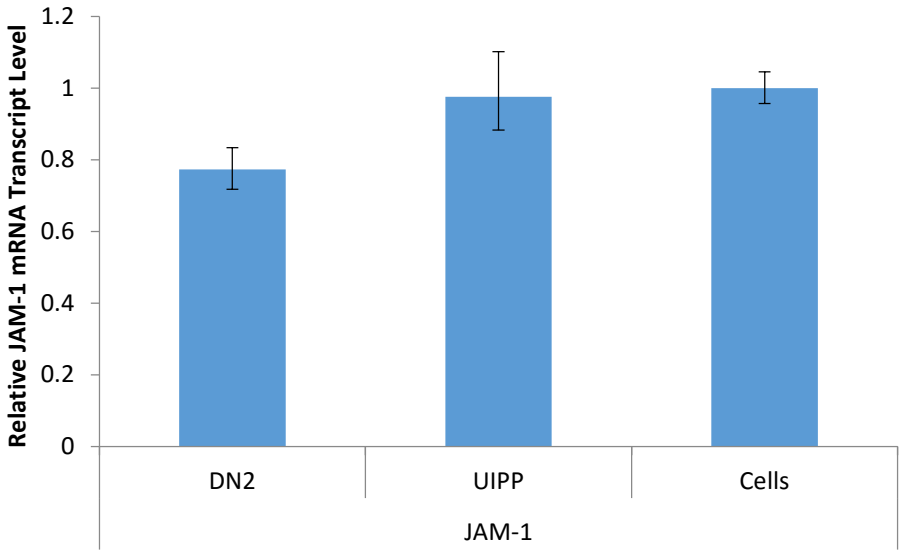


**Figure 7**

The effect of P(1.5) (DN2) or unimprinted polypropylene (UIPP) on the expression of JAM-1 mRNA. Data is shown as means with standard deviation as error bars. Difference between P(1.5) and UIPP, and P(1.5) and cells are statistically significant ($p<0.05$).

a

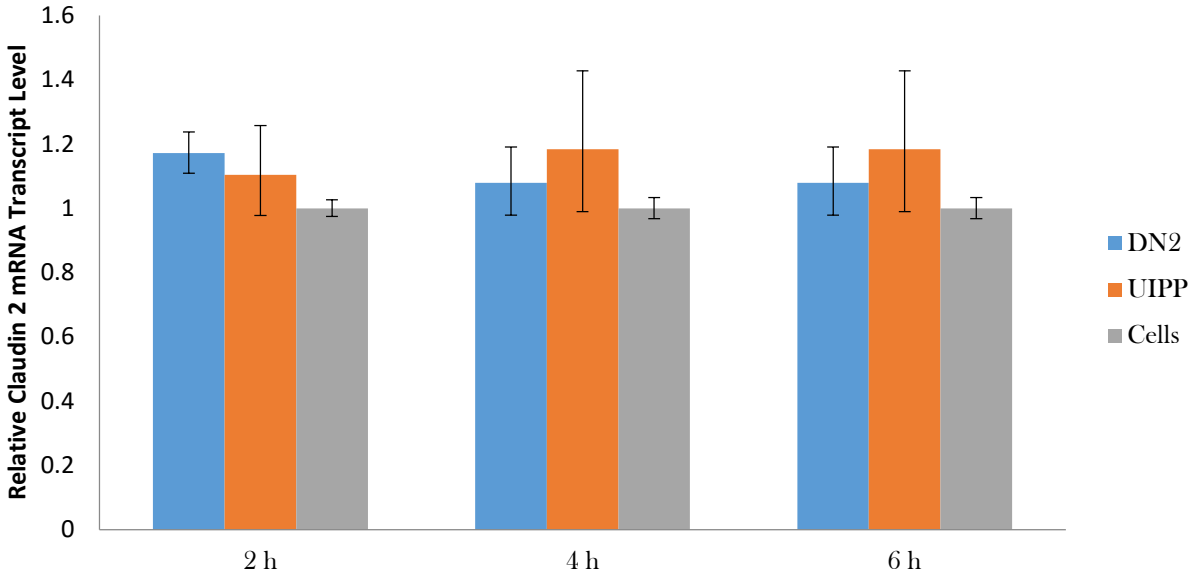
Relative Claudin 2 mRNA Transcript Level
1.6
1.4
1.2
1
0.8
0.6
0.4
0.2
0
2 h
4 h
6 h
DN2
UIPP
Cells

b

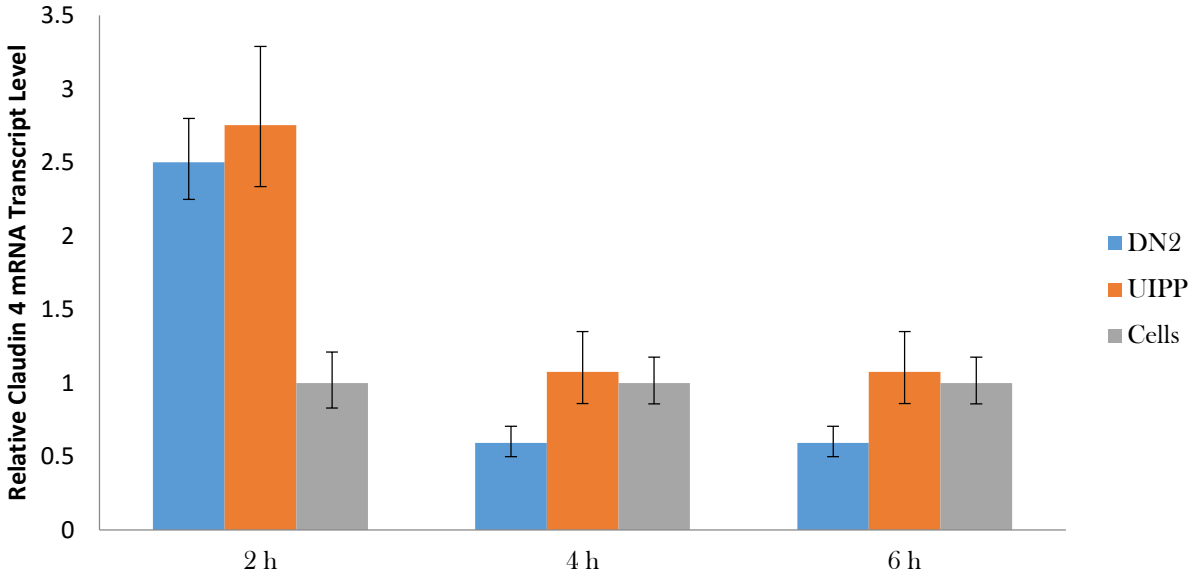
Relative Claudin 4 mRNA Transcript Level
3.5
3
2.5
2
1.5
1
0.5
0
2 h
4 h
6 h
DN2
UIPP
Cells

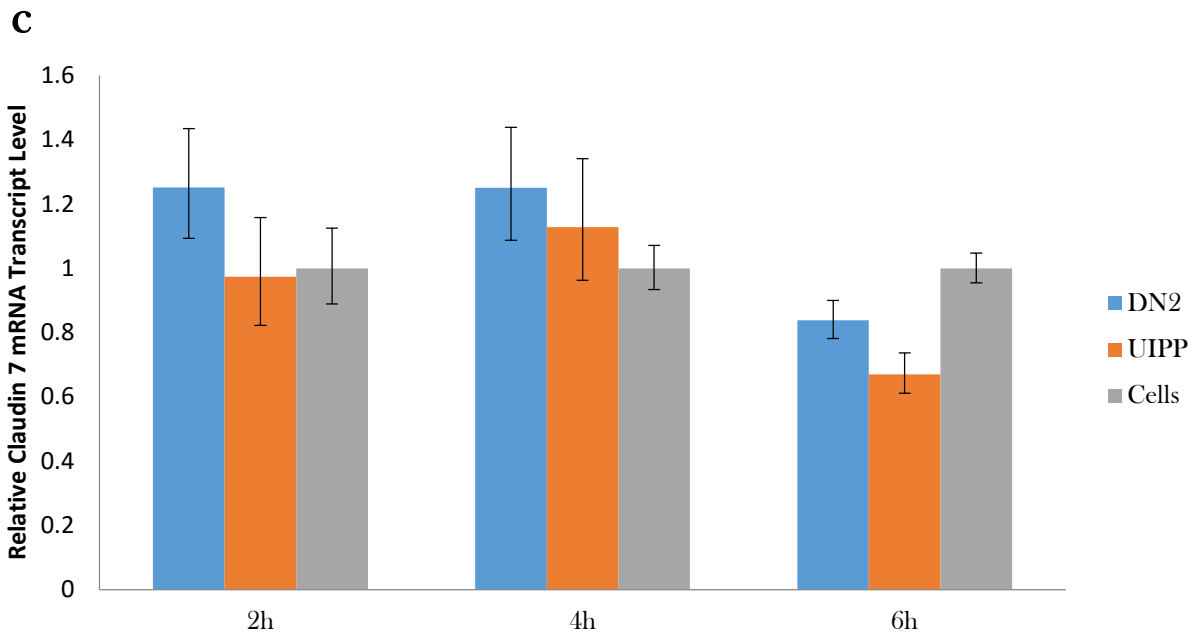


**Figure 8**

The effect of P(1.5) (DN2) or unimprinted polypropylene (UIPP) on the expression of claudin 2 (a), claudin 4 (b), and claudin 7 (c) mRNA at 2, 4 and 6 hours in contact with the films.. Data is shown as means with standard deviation as error bars. (a) Difference between claudin 2 mRNA expression of P(1.5) are statistically significant ($p<0.05$). (b) Difference between P(1.5) or UIPP and cells at 2 hours, P(1.5) and UIPP or cells at 4 hours, and P(1.5) and UIPP or cells at 6 hours are statistically significant ($p>0.05$). (c) Difference between P(1.5) and UIPP or cells at 6 hours is statistically significant ($p>0.05$).

To more broadly examine transcriptional changes in tight junction and polarity related proteins, we examined the gene expression of 84 related genes. The material of polypropylene alone decreased gene expression of 6 genes (Figure 9). VAMP (vesicle-associated membrane protein)-

associated protein A (VAPA) is a junctional interacting protein that is associated with vesicle trafficking, as it is found in both the plasma membrane and intracellular vesicles[12]. Myeloid/lymphoid or mixed-lineage leukemia; translocated to, 4 (MLLT4) is involved in tight junction assembly.[13] Both of these junctional interacting proteins are down regulated. Also down regulated at three genes associated with regulating the cytoskeleton and a cell surface receptor: scribble cell polarity complex component (LLGL1), par-3 family cell polarity regulator (PARD3), par-6 family cell polarity regulator beta (PARD6b), and claudin 5 (cldn5).

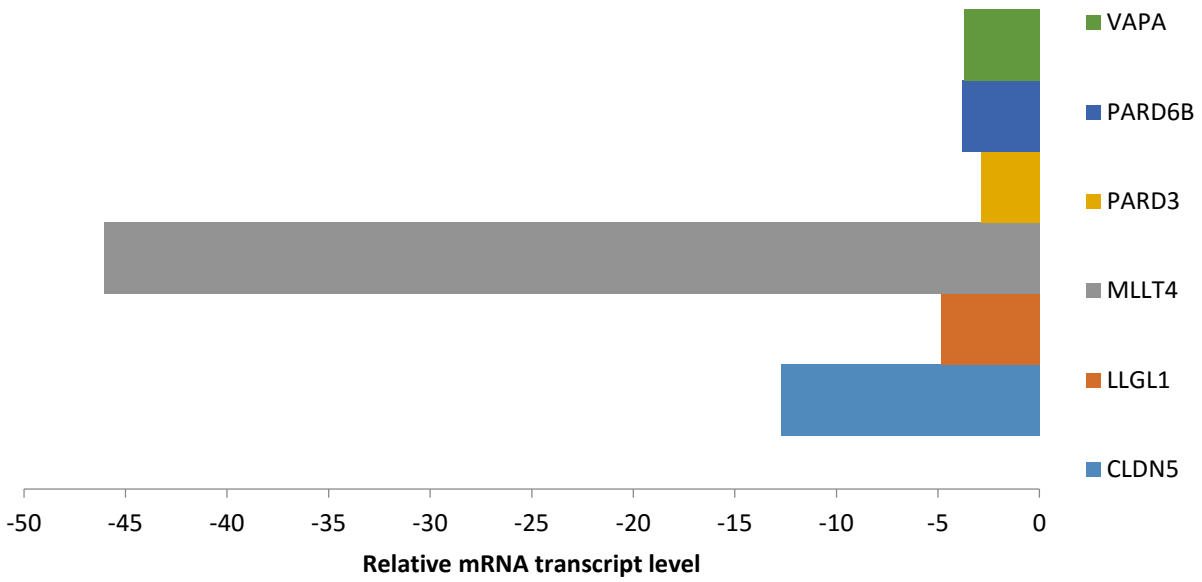

**Figure 9**

Statistically significant ($p>0.05$) gene expression changes comparing UIPP to Cells from tight junction array by qPCR. VAPA, PARD6B, PARD3, MLLT4, LLGL1, and CLDN5 are all down regulated by contact with UIPP as compared to cells alone.

Cells in contact with nanotopography down regulated expression of 11 genes as compared to cells alone. Two genes are also down regulated by UIPP, so probably due to the material and not topography. Tight junction associated protein 1 (TJAP1), tight junction protein 2 (TJP2), and tight junction protein 3 (TJP3) are all incorporated into the tight junction at different stages. TJP2 and TJP3, also known as zonula occludins 2 and 3 respectively, are required for proper assembly of tight junctions and form a link between the tight junction and the actin cytoskeleton.[14,15] Rac1 expression, which was increased in response to nanowires, is decreased in expression in cells in contact with the P(1.5) thin films. Microtubule affinity regulating kinase 2 (MARK2) shows decreased expression and is involved in establishing cellular polarity and remodeling of microtubules.[16] Interestingly, down regulation of phosphatase and tensin homolog (PTEN), as we observed, has been correlated with increased permeability of caco2 cells.[17] Protein kinase C zeta (PRKCZ), which was found to be upregulated by silicon nanowires, is down regulated by nanotopographical films. Claudin 6 (cldn6) expression is normally associated with decreased permeability.[18] Cldn6 expression was down regulated by nanotopography, which further supports that nanotopography is remodeling tight junctions and increasing paracellular permeability.

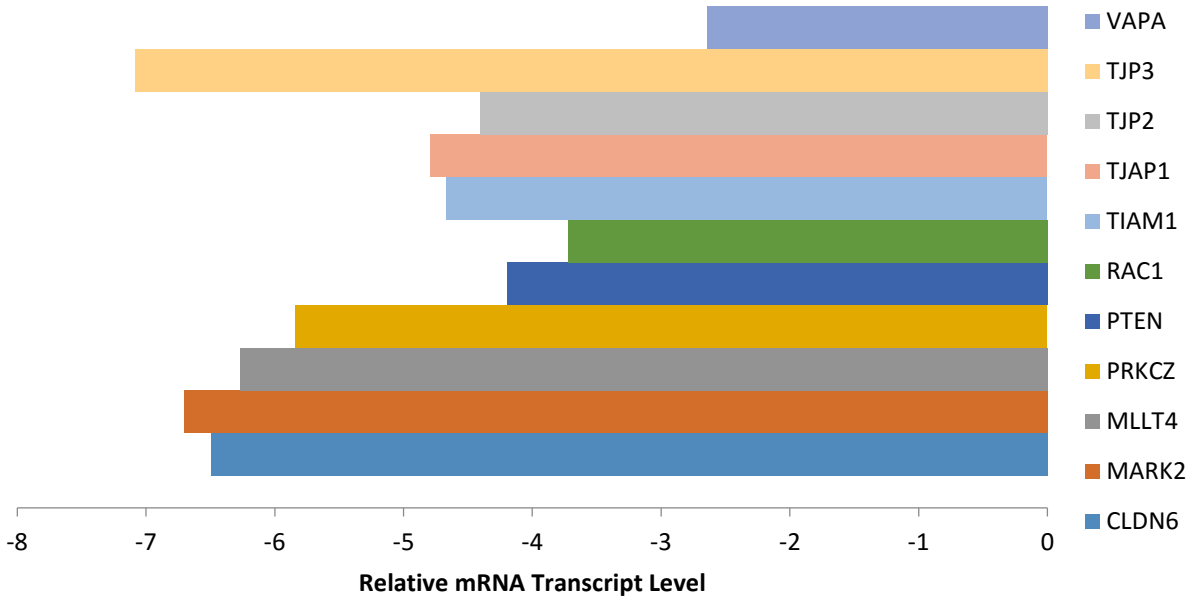


**Figure 10**

Statistically significant gene expression differences comparing P(1.5) and cells alone ($p<0.05$). VAPA, TJP3, TJP2, TJAP1, TIAM1, RAC1, PTEN, PRKCZ, MLLT4, MARK2, and CLDN6 are all down regulated by cellular contact with P(1.5) compared to cells alone.

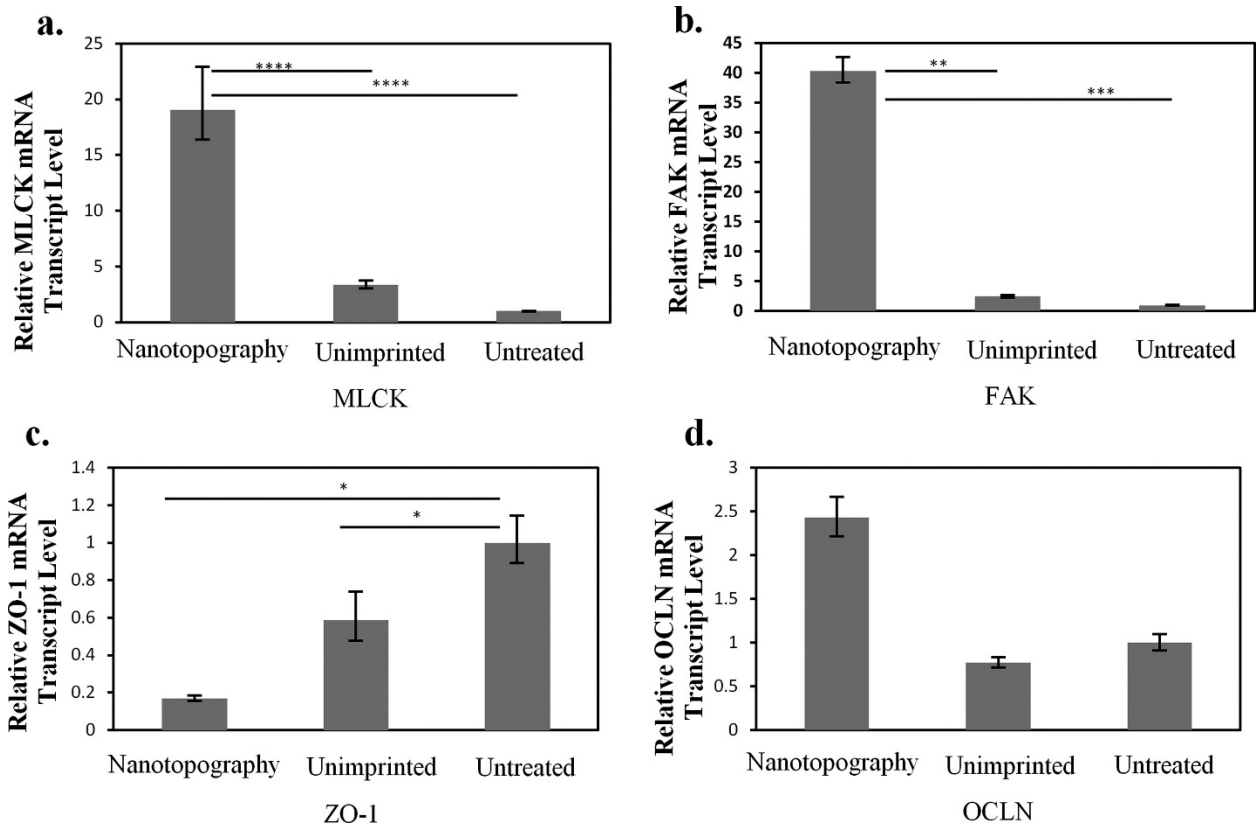


**Figure 11**

Quantitative PCR studies. The gene expression levels of the signaling molecules, myosin light chain kinase (MLCK) and focal adhesion kinase (FAK), are displayed in (a) and (b). The gene expression levels of tight junction proteins zonula occludin-1 (ZO-1) and occludin (ocln) are also displayed in (c) and (d). Data are normalized by expression levels of each gene by the controls (Untreated) and presented as an average ± standard deviation. *$p < 0.05$, **$p < 0.005$, ***$p < 0.002$, and ****$P < 0.001$, $n = 3$.[8]

To further examine the paracellular transport route, different signaling molecules were investigated through gene expression studies. From Figure 11, it is apparent that the nanostructured thin film has a dramatic effect on the overall mRNA transcription levels. For example, myosin light chain kinase (MLCK), an important regulator of paracellular permeability,

increased by 5.6-fold and 19-fold in cells that contacted the nanostructured thin films compared to the unimprinted polypropylene and untreated controls, respectively. MLCK is a protein kinase associated with tight junctions through the contraction of the cortical actin cytoskeleton and has been previously reported to enhance paracellular permeability.[19] These results suggest that the nanotopography may lead to increased paracellular transport by activating mechanotransduction pathways. Additionally, focal adhesion kinase (FAK) transcript expression was examined to measure the formation of focal adhesions as an indication of the level of signaling through integrin binding and clustering. Extensive work in the literature has demonstrated the coordinated cross talk between integrin-binding and the junctional complex for the maintenance of epithelial integrity.[20] To this end, we demonstrated that the FAK mRNA expression was increased over 16-fold in cells that contacted the nanostructured thin film. This data supports the observation that tight junction loosening may be triggered by integrin engagement mediated by FAK. Although our strategy utilizes a physical cue and not a biological peptide sequence, the mechanical stimulus from the nanostructures may imitate receptor–ligand interactions on the nano scale. Therefore, our approach offers a novel platform to investigate interactions that may be related to both physical and biological mechanisms.

This restructuring of the tight junctions to allow for paracellular drug transport is further supported by the gene expression results for tight junction proteins. There is a significant decrease in ZO-1 mRNA expression levels compared to the controls, as shown in Figure 11. Many studies have reported that a correlation exists between a decrease in ZO-1 protein expression and enhanced paracellular permeability. For example, Tian et. al demonstrated that stimulation of HK-2 cells with TGF-β resulted in a decrease in ZO-1 protein expression, indicating tight junction disassembly and a subsequent increase in paracellular permeability.[21]

Similarly, hepatic growth factor (HGF) stimulated RPE monolayers were observed to lose barrier function resulting from a decrease in ZO-1 protein expression in the presence of HGF.[22] Therefore, a decrease in ZO-1 gene expression is consistent with tight junction disassembly and enhanced paracellular permeability.

An increase in the expression of occludin (ocln) due to the nanostructured surface was also observed. Ocln is a transmembrane component of tight junctions that regulates paracellular permeability. Consistent with these results, Wang et. al also observed an increase in protein expression of ocln and enhanced paracellular permeability when BMECs were treated with VEGF.[23] Our results suggest that the nanostructures are influencing mechanotransduction pathways to actively remodel the tight junctions and facilitate the transport of etanercept. Furthermore, this phenomenon appears to be a reversible process as indicated by the TEER values returning to their original values when the nanostructured surfaces are removed after 24 h. This result suggests that the tight junctions recover and that the nanostructure does not illicit cytotoxic effects. The nanostructures seem to dramatically affect the paracellular pathway by directly modulating the tight junction proteins.[8]

We hypothesized that nanotopography increases paracellular transport by remodeling the tight junctions. Increased expression of FAK and MLCK implicate these signaling molecules play a role in increased paracellular transport in response to nanotopographical cues. To this end, we inhibited FAK chemically and examined whether there was still a decrease in TEER and therefore an increase in paracellular permeability. If FAK was indeed required for nanotopography-mediated transport, we would expect to see no decrease in TEER. As observed in figure 12, b there was a decrease in TEER with the inhibitor and no statistically significant

difference in TEER between cells in contact with nanotopography with and without inhibition. Therefore, FAK signaling is not required for this increase in paracellular permeability. However, FAK at the start of the proposed signaling pathway, and it is possible that there are redundant or compensatory signaling.

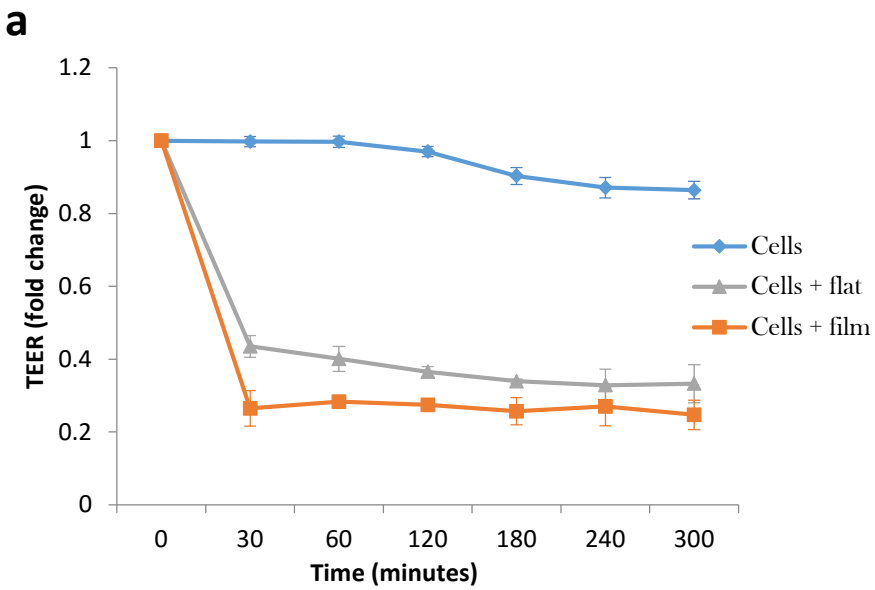


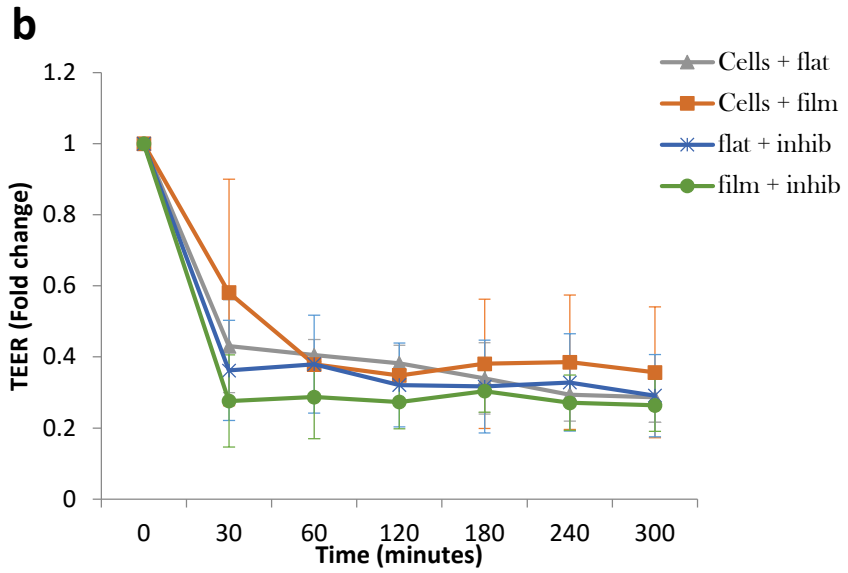

**Figure 12**

Transepithelial electrical resistance fold change (a) of cells alone (blue diamonds), in contact with unimprinted polypropylene film (flat, gray triangles), or P(1.5) nanostructured film (film, orange squares). Cells in contact with P(1.5) has a greater magnitude decrease than cells in contact with UIPP film. (b) Fold change of TEER with and without FAK inhibitor (inhib) treatment of cells in contact with either UIPP (flat) or P(1.5) film (film). FAK inhibitor does not inhibit drop in TEER seen with nanostructure application.

ROCK is a mechanotransduction signaling molecule downstream of focal adhesion formation and upstream of MLCK contraction of the cytoskeleton.[24,25] It plays a role in sensing and remodeling the cytoskeleton in response to perceived cellular tension and microenvironmental stiffness.[26] It also inhibits myosin phosphatase activity and directly phosphorylates myosin to contract the cellular cytoskeleton, which is connected to the tight junction via adaptor proteins such as the zonula occludins. We used an inhibitor of ROCK to investigate whether ROCK activity is required for increased 150 kDa dextran drug transport across a caco2 monolayer. Treatment with the ROCK inhibitor modestly decreased drug transport by nanotopography, but the difference was not statistically significant. This suggests that ROCK signaling could play a role in remodeling the tight junction as a result of cellular interaction with nanotopography, but there may be other parallel signaling pathways involved. ROCK has been implicated in being required for central MLC phosphorylation, while MLCK plays a spatially distinct role phosphorylating peripheral MLC.[27] This may explain why ROCK inhibition has less than complete effect and warrants investigating the role of MLCK activity in nanotopography mediated tight junction remodeling.

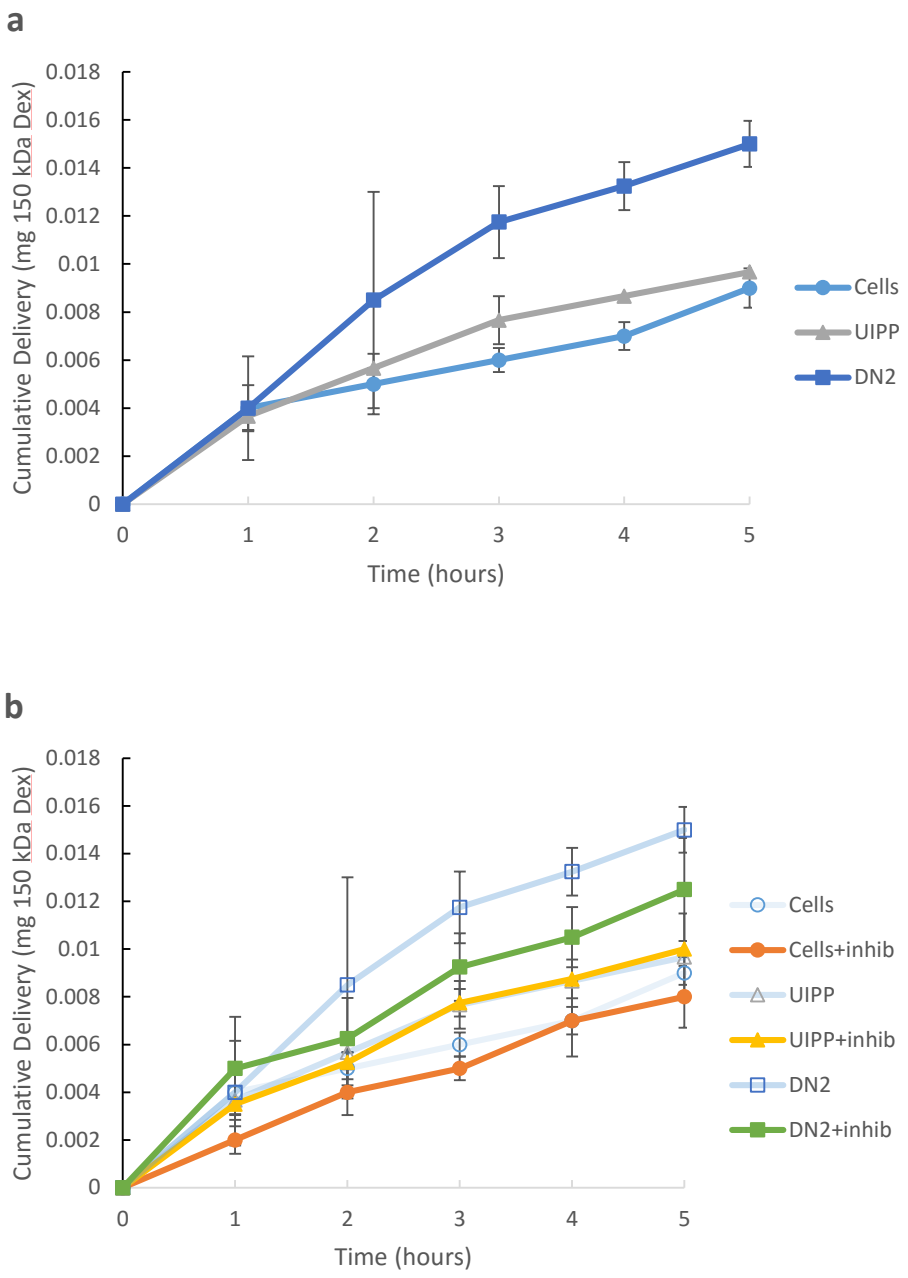


**Figure 13**

(a) 150 kDa dextran (Dex) drug delivery across caco-2 monolayer grown on transwell insert (cells, blue circles), cells in contact with UIPP (UIPP, gray triangles), and P(1.5) (DN2, dark blue squares). Difference between cells and UIPP or P(1.5) at 3 hour onward, and between UIPP

and P(1.5) at 4 hours are statistically significant (p>0.05). (b) 150 kDa dextran diffusion across caco-2 monolayer treated with ROCK inhibitor (cells+inhib, orange circles), cells treated with ROCK inhibitor in contact with UIPP (UIPP+inhibi, yellow triangles), and cells treated with ROCK inhibitor in contact with P(1.5) (DN2+inhib, green squares). ROCK inhibitor has a modest, but not statistically significant decrease in drug delivery across the caco2 monolayer.

**References**


1. Uskoković, V., Lee, P. P., Walsh, L. A., Fischer, K. E. & Desai, T. A. PEGylated silicon nanowire coated silica microparticles for drug delivery across intestinal epithelium. *Biomaterials* **33,** 1663–72 (2012).

2. Popoff, M. R. & Geny, B. Multifaceted role of Rho, Rac, Cdc42 and Ras in intercellular junctions, lessons from toxins. *Biochim. Biophys. Acta* **1788,** 797–812 (2009).

3. Migeotte, I., Grego-Bessa, J. & Anderson, K. V. Rac1 mediates morphogenetic responses to intercellular signals in the gastrulating mouse embryo. *Development* **138,** 3011–20 (2011).

4. Fasano, A. Regulation of intercellular tight junctions by zonula occludens toxin and its eukaryotic analogue zonulin. *Ann. N. Y. Acad. Sci.* **915,** 214–22 (2000).

5. Mashukova, A., Wald, F. A. & Salas, P. J. Tumor necrosis factor alpha and inflammation disrupt the polarity complex in intestinal epithelial cells by a posttranslational mechanism. *Mol. Cell. Biol.* **31,** 756–65 (2011).

6. Chou, S. Y. & Krauss, P. R. Imprint lithography with sub-10 nm feature size and high throughput. *Microelectron. Eng.* **35,** 237–240 (1997).

7. Chou, S. Y., Krauss, P. R. & Renstrom, P. J. Imprint Lithography with 25-Nanometer Resolution. *Science (80-. ).* **272,** 85–87 (1996).

8. Kam, K. R. *et al.* Nanostructure-mediated transport of biologics across epithelial tissue: enhancing permeability via nanotopography. *Nano Lett.* **13,** 164–71 (2013).

9. Kam, K. R. *et al.* Nanostructure-Mediated Transport of Biologics across Epithelial Tissue: Enhancing Permeability via Nanotopography. *Nano Lett.* **13,** 164–171 (2013).

10. Vercauteren, D. *et al.* The use of inhibitors to study endocytic pathways of gene carriers: optimization and pitfalls. *Mol. Ther.* **18,** 561–9 (2010).

11. Martìn-Padura, I. *et al.* Junctional Adhesion Molecule, a Novel Member of the Immunoglobulin Superfamily That Distributes at Intercellular Junctions and Modulates Monocyte Transmigration. *J. Cell Biol.* **142,** 117–127 (1998).

12. Lapierre, L. A., Tuma, P. L., Navarre, J., Goldenring, J. R. & Anderson, J. M. VAP-33 localizes to both an intracellular vesicle population and with occludin at the tight junction. *J. Cell Sci.* **112 ( Pt 2,** 3723–32 (1999).

13. Lorger, M. & Moelling, K. Regulation of epithelial wound closure and intercellular adhesion by interaction of AF6 with actin cytoskeleton. *J. Cell Sci.* **119,** 3385–98 (2006).

14. Fanning, A. S., Jameson, B. J., Jesaitis, L. A. & Anderson, J. M. The Tight Junction Protein ZO-1 Establishes a Link between the Transmembrane Protein Occludin and the Actin Cytoskeleton. *J. Biol. Chem.* **273,** 29745–29753 (1998).

15. Haskins, J., Gu, L., Wittchen, E. S., Hibbard, J. & Stevenson, B. R. ZO-3, a novel member of the MAGUK protein family found at the tight junction, interacts with ZO-1 and occludin. *J. Cell Biol.* **141,** 199–208 (1998).

16. Cohen, D., Brennwald, P. J., Rodriguez-Boulan, E. & Müsch, A. Mammalian PAR-1 determines epithelial lumen polarity by organizing the microtubule cytoskeleton. *J. Cell Biol.* **164,** 717–27 (2004).

17. Zhang, L., Shen, J., Cheng, J. & Fan, X. MicroRNA-21 regulates intestinal epithelial tight junction permeability. *Cell Biochem. Funct.* **33,** 235–40 (2015).

18. Sas, D., Hu, M., Moe, O. W. & Baum, M. Effect of claudins 6 and 9 on paracellular permeability in MDCK II cells. *Am. J. Physiol. Regul. Integr. Comp. Physiol.* **295,** R1713–9 (2008).

19. Shen, L. *et al.* Myosin light chain phosphorylation regulates barrier function by remodeling tight junction structure. *J. Cell Sci.* **119,** 2095–2106 (2006).

20. Ojakian, G., Ratcliffe, D. & Schwimmer, R. Integrin regulation of cell-cell adhesion during epithelial tubule formation. *J. Cell Sci.* **114,** 941–952 (2001).

21. Tian, Y. C. & Phillips, A. O. Interaction between the transforming growth factor-beta type II receptor/Smad pathway and beta-catenin during transforming growth factor-beta1-mediated adherens junction disassembly. *Am. J. Pathol.* **160,** 1619–28 (2002).

22. Jin, M., Chen, Y., He, S., Ryan, S. J. & Hinton, D. R. Hepatocyte growth factor and its role in the pathogenesis of retinal detachment. *Invest. Ophthalmol. Vis. Sci.* **45,** 323–9 (2004).

23. Wang, W., Dentler, W. L. & Borchardt, R. T. VEGF increases BMEC monolayer permeability by affecting occludin expression and tight junction assembly. *Am. J. Physiol. Heart Circ. Physiol.* **280,** H434–40 (2001).

24. Bishop, A. L. & Hall, A. Rho GTPases and their effector proteins. *Biochem. J.* **348 Pt 2,**

241–55 (2000).

25. Ishizaki, T. *et al.* p160ROCK, a Rho-associated coiled-coil forming protein kinase, works downstream of Rho and induces focal adhesions. *FEBS Lett.* **404,** 118–24 (1997).

26. Bhadriraju, K. *et al.* Activation of ROCK by RhoA is regulated by cell adhesion, shape, and cytoskeletal tension. *Exp. Cell Res.* **313,** 3616–23 (2007).

27. Totsukawa, G. *et al.* Distinct Roles of Rock (Rho-Kinase) and Mlck in Spatial Regulation of Mlc Phosphorylation for Assembly of Stress Fibers and Focal Adhesions in 3t3 Fibroblasts. *J. Cell Biol.* **150,** 797–806 (2000).

# Chapter 5 - Nanotopography facilitates in vivo transdermal delivery of high molecular weight therapeutics through an integrin-dependent mechanism.


## Abstract

Transdermal delivery of therapeutics is restricted by narrow limitations on size and hydrophobicity. Nanotopography has been shown to significantly enhance high molecular weight paracellular transport *in vitro*. Herein, we demonstrate for the first time that nanotopography applied to microneedles significantly enhances transdermal delivery of etanercept, a 150 kDalton therapeutic, in both rats and rabbits. We further show that this effect is mediated by remodeling of the tight junction proteins initiated via integrin binding to the nanotopography, followed by phosphorylation of myosin light chain (MLC) and activation of the actomyosin complex, which in turn increase paracellular permeability.


Skin serves as the critical boundary between the external world and our viscera. The stringency of the epidermal barrier is reflected by the dearth of transdermally delivered drugs; currently only 17 drugs have been approved for this delivery route by the Food and Drug Administration (FDA), and all of these agents fall within a very narrow parameter space (<500 Da in size and highly lipophilic). The limitations of transdermal technology appear even starker with the increasingly frequent development of high molecular weight, antibody-based therapeutics, many of which have promising biologic effects but are hampered by limited delivery options.

Until recently, skin barrier function was thought to be mediated entirely by the outermost stratum corneum, a defined meshwork of anucleate keratinocytes, lipids, and proteins. However, recent studies have discovered the presence of the epidermal tight junction (TJ) and multiple TJ proteins, including occludin, zonula occludins-1 (ZO-1), and in particular claudins, which are

critical for epidermal barrier function.[1–8] TJ complexes function as the paracellular barrier in simple epithelial cell types such as gastrointestinal mucosal cells and offer an additional well-conserved mechanism through which the skin can regulate its permeability.[9–11] While multiple technologies have attempted to increase the permeability of the stratum corneum, less emphasis has been placed on modulation of the skin TJ barrier.[12–15] In a recent study, Kam et al. demonstrated that nanotopography loosens tight junctions in simple epithelia and dramatically increases transepithelial transport of etanercept, a high molecular weight therapeutic that is used clinically for rheumatoid arthritis (RA) and severe psoriasis and psoriatic arthritis.[16] However, the extent to which nanotopography loosens tight junctions in more stratified squamous epithelium such as skin or *in vivo* is not known.

In this study, we explore nanotopography as a novel strategy to enhance transdermal drug delivery. In both rat and rabbit animal models, we demonstrate for the first time that the addition of nanotopography dramatically enhances transdermal delivery of etanercept through microneedle arrays (MNAs). To explore the molecular mechanisms underlying this phenomenon, we examined TJ protein expression in cultured human primary multilayered keratinocytes and found that levels of claudin-1 and claudin-4 are significantly and reversibly reduced with nanotopography. This phenomenon is conserved in intestinal epithelial Caco-2 cells and furthermore is dependent on upstream integrin binding and MLC phosphorylation. These findings demonstrate that nanotopographic surfaces provide a new approach to significantly expand the scope of drugs that can be administered transdermally, including agents with a size range that includes the emerging and expanding class of antibody-based therapeutics.

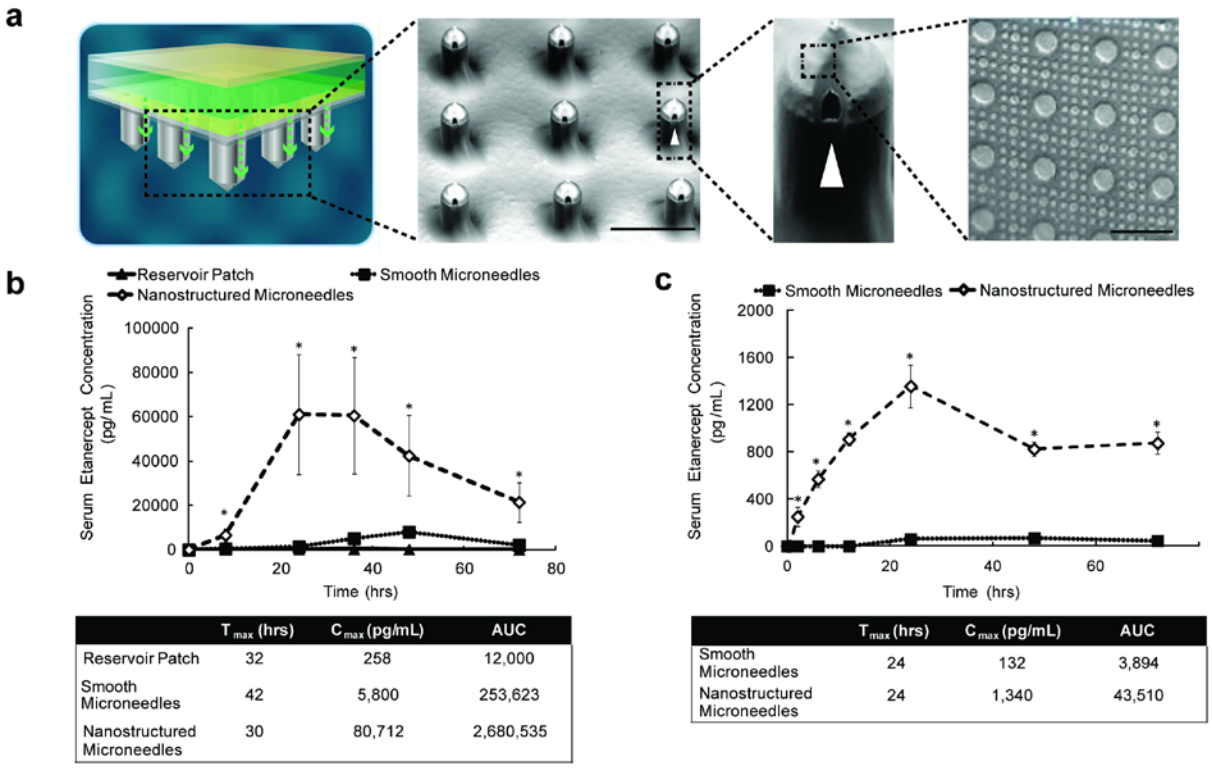


| | $T_{max}$ (hrs) | $C_{max}$ (pg/mL) | AUC |
|---|---|---|---|
| Reservoir Patch | 32 | 258 | 12,000 |
| Smooth Microneedles | 42 | 5,800 | 253,623 |
| Nanostructured Microneedles | 30 | 80,712 | 2,680,535 |

| | $T_{max}$ (hrs) | $C_{max}$ (pg/mL) | AUC |
|---|---|---|---|
| Smooth Microneedles | 24 | 132 | 3,894 |
| Nanostructured Microneedles | 24 | 1,340 | 43,510 |

**Figure 1**

Nanotopography significantly enhances transdermal delivery of etanercept in vivo (a) Schematic representation of the transdermal delivery devices used in this study. Progressing from top to bottom: each device is made of an impermeable backing (tan), drug reservoir (green), rate-controlling membrane (yellow), and silicon microneedle array (MNA) (grey). Each 290 μm long, 100 μm wide microneedle has longitudinal perforations along the side, through which drug flows out. Drug path is indicated by a green dashed arrow. Perforations are denoted with a white arrowhead. "Smooth" microneedles were not coated with a film, while "nanostructured" microneedles were coated with a nanostructured film. (scale bar represents 300 μm). Inset on furthest right depicts an SEM image of the nanostructures coated onto each microneedle (scale bar = 3 μm). (b) Nanostructured MNAs deliver significantly more etanercept transdermally than either drug reservoir patch alone or unstructured, smooth MNA controls in rats. After 72 hours, the

nanostructured MNA cumulatively delivered 10.6 times more etanercept (*p<0.01) and achieved a maximal serum concentration ($C_{max}$) 13.9 times higher (*p<0.01) than the smooth microneedles (n=4 animals for each category). (c) Nanostructured MNAs deliver significantly more etanercept transdermally than unstructured, smooth MNA controls in rabbits. After 72 hours, the nanostructured MNA devices cumulatively delivered 35 times more etanercept (*p<0.01) and achieved a $C_{max}$ 10.2 times higher than smooth MNA controls (*p<0.01) (n=4 animals for each category)

The effect of nanotopography on microneedle-based transdermal delivery of etanercept was assessed *in vivo* in both rabbits and rats. Transdermal devices consisting of two different permeability enhancing components were fabricated. The first component was a 25 mm by 25 mm array of microneedles, (Figure 1a). Each microneedle on this array was 290 μm in length and 100 μm wide, with a pitch of 400 μm; drug flowed out of each microneedle via longitudinal grooves along its sides. The second component was a polymeric film with nanostructures imprinted onto its surface (Figure 1a – inset). This film was draped over the microneedle array (MNA), effectively giving each needle a nanostructured coating. Depth of penetration of the MNAs was assessed in rats by soaking the skin samples in methylene blue following application of the MNA. The skin was then cryosectioned, and the depth of dye penetration was measured for each point in the array. Average depth of penetration in rat skin was 58 microns, placing the needles at the epidermal-dermal junction[17] (Figure S1).

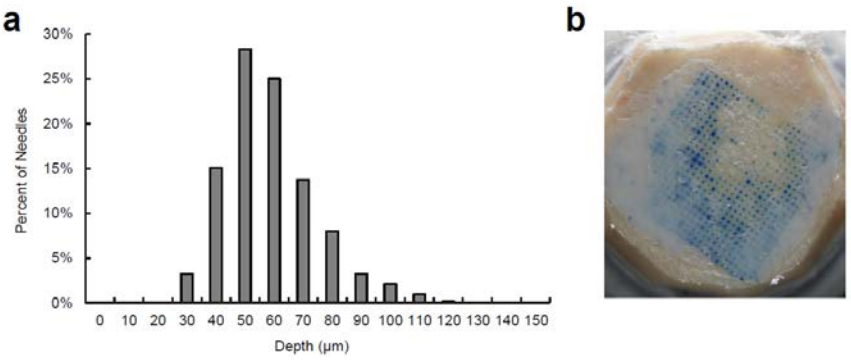


**Figure S1**

Microneedle penetration in rat skin. (a) The depth of MNA penetration ranged from 30 to 120 microns. Average depth of penetration in rat skin was 58 microns. (b) Depth of penetration of the MNAs was assessed in rats by soaking the skin samples in methylene blue following application of the MNA. The skin was then cryosectioned, and the depth of dye penetration was measured for each point in the array.

For drug delivery characterization, 12.5 mg of etanercept (0.25 mL at 50 mg/mL) was administered transdermally to rats, or 1.85 mg was administered to rabbits through one of three devices: the drug reservoir alone; an MNA array with no nanostructured coating ("smooth") ; or an MNA array coated with nanostructured film (Figure 1b and c). The serum concentration of etanercept via each delivery route was then measured over 72 hours. After 72 hours in rats, the nanostructured MNA cumulatively delivered 10.6 times more etanercept ($p<0.01$) and achieved a maximal serum concentration ($C_{max}$) 13.9 times higher ($p<0.01$) than the unstructured, smooth microneedles. In rabbits, the nanostructured MNA devices cumulatively delivered 35 times more etanercept ($p<0.01$) and achieved a $C_{max}$ 10.2 times higher than unstructured, smooth MNA controls ($p<0.01$). Regarding the kinetics of drug delivery, the time to maximal serum concentration ($T_{max}$) in rabbits was equivalent between nanostructured and smooth MNAs, while

in rats, the $T_{max}$ was shorter for the nanostructured MNAs (30 hours) than with the smooth MNAs (42 hours). Examination of the skin following application of the devices showed minimal erythema and inflammation after 72 hours (Figure S2).

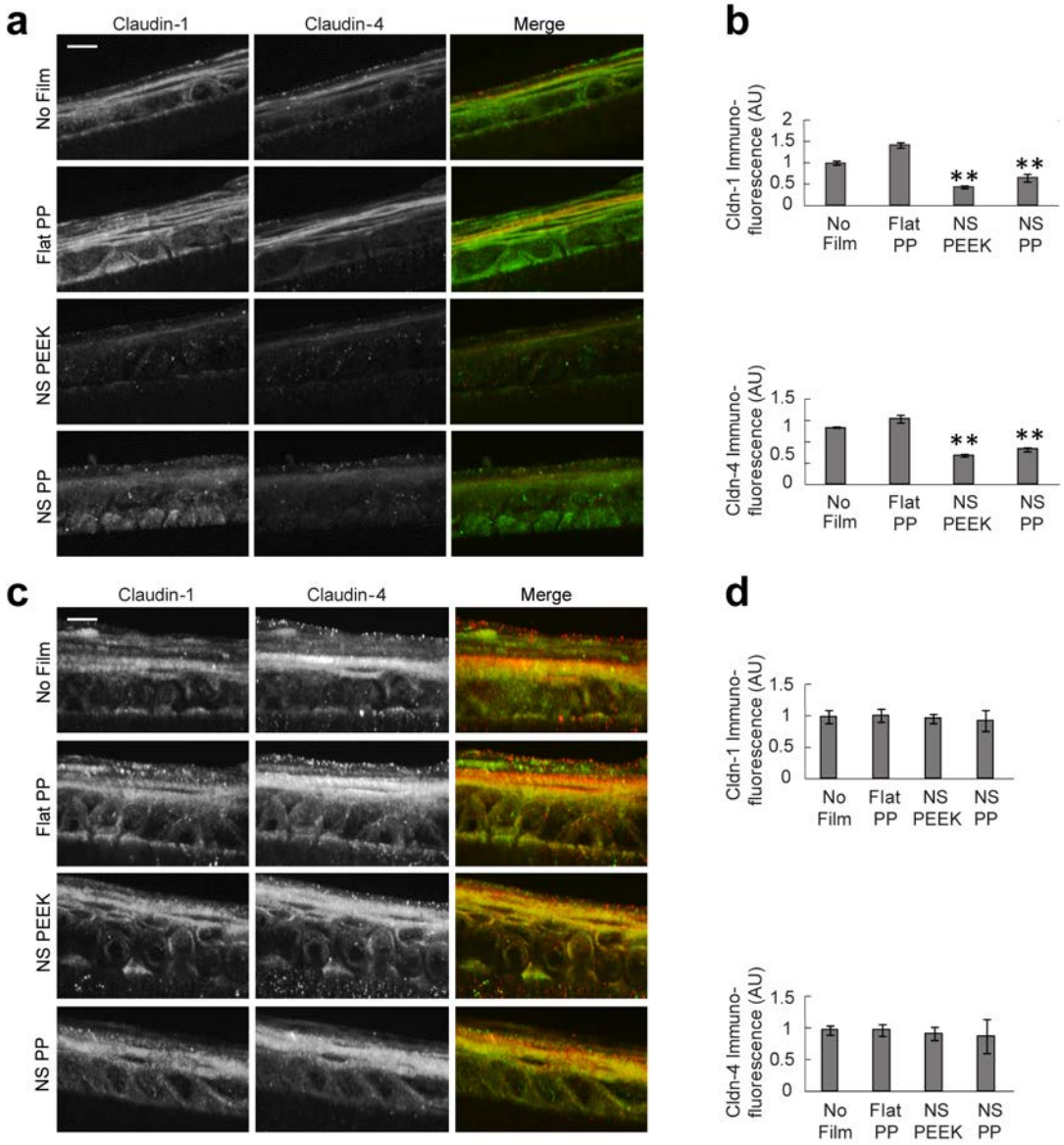


**Figure 2**

Nanotopography leads to reversible downregulation of claudin-1 and 4 expression in cultured human keratinocytes. (a-b) Day 8 primary human keratinocytes showed marked diminishment in

claudin-1 and 4 expression after 24 hour incubation with nanotopography, compared to controls that were exposed to no device or to unstructured, flat films. Claudin-1 was decreased by 58% with polyether ether ketone (PEEK)-based nanostructured films (NS PEEK) and by 36% with polypropylene-based nanostructured films (NS PP), relative to no device controls (**$p<0.01$). Claudin-4 was decreased by 49% with PEEK nanostructured films and by 39% with polypropylene nanostructured films, relative to no device controls (**$p<0.01$). Exposure to unstructured, flat films (Flat PP) had no effect on claudin-1 or 4 expression relative to no device controls (scale bar = 10 μm). Fluorescence intensity was normalized by area. (c-d) 24 hours following removal of nanotopography, the decrease in claudin-1 and 4 expression was reversed, and there was no statistically significant difference between nanotopography-treated keratinocytes (NS PP and NS PEEK) versus no device or unstructured, flat controls (scale bar = 10 μm).

To explore the molecular mechanisms through which nanotopography increases epidermal permeability, we directly exposed primary human cultured keratinocytes to the nanostructured coating. This culture system forms stratified layers and tight junctions that recapitulate skin development *in vivo*[1]. Keratinocytes were allowed to develop to day 8, at which point they develop only a minimal stratum corneum layer. We elected this time point in order to provide a differentiated cell system that still enables maximal contact of the nanostructured film to the epidermal TJs, which lie beneath the stratum corneum layer of skin. After 24 hours of exposure to the nanotopography, keratinocytes showed marked downregulation of the TJ proteins claudins-1 and 4, compared to control keratinocytes that were either unexposed or placed in contact with unstructured, flat control film of the same material ($p<0.01$) (Figure 2a and b).

To assess whether this effect on claudins was reversible, we removed nanotopography for 24 hours after exposure and again assessed for claudin-1 and 4 protein expression. After removal of

the device, claudin-1 and 4 levels were equivalent in keratinocytes alone, keratinocytes exposed to unstructured control films, and keratinocytes exposed to nanotopography, suggesting that alterations in TJ morphology by nanotopography are reversible (Figure 2c and d).

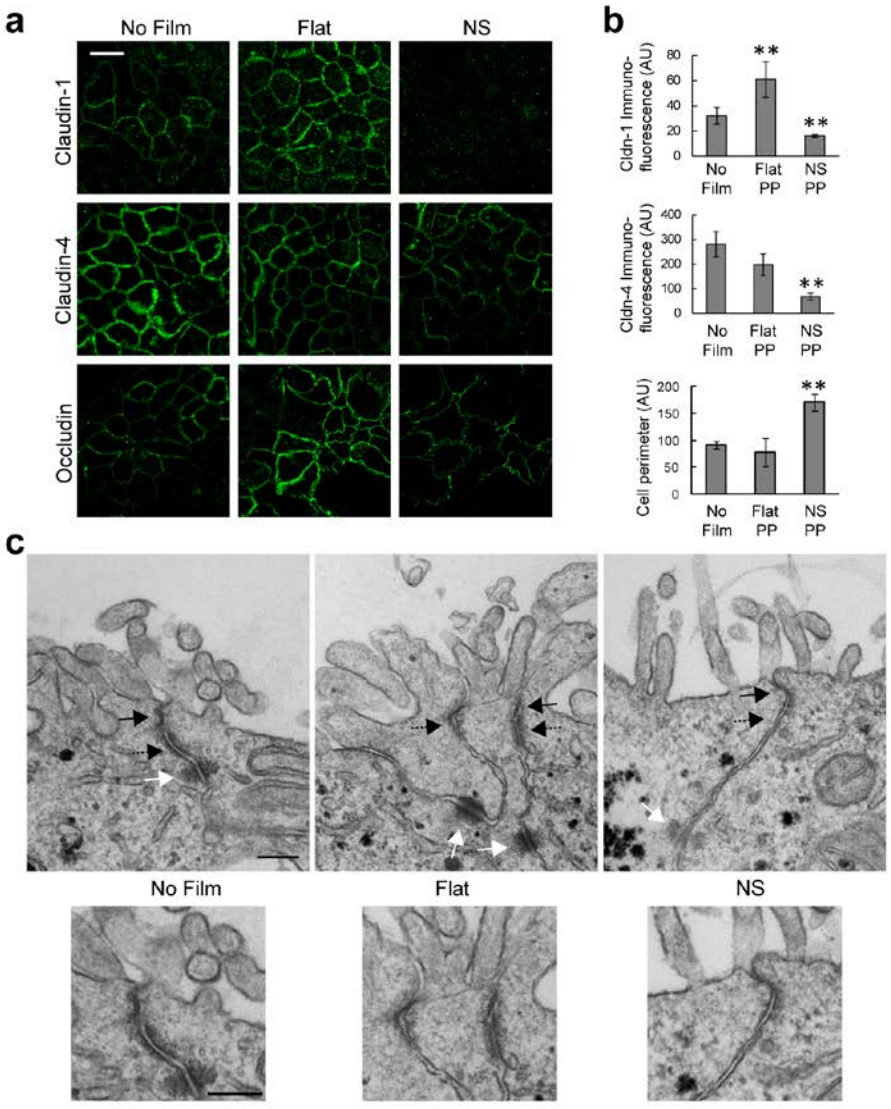


**Figure 3**

Nanotopography-induced disruption of TJ structure is conserved among different epithelia. (a-b) In Caco-2 cells, nanostructured films (NS) induce decreased expression of claudin-1 and 4 at cell borders, relative to controls exposed to no film or to unstructured, flat film (Flat). Claudin-1 was decreased 50% compared to no film control and 73% compared to the flat film control (**$p<0.01$). Claudin-4 was decreased 76% and 66% compared with the no film or flat film controls respectively (**$p<0.01$). Occludin immunostaining reveals a ruffled pattern when Caco-2 cells are in contact with the nanostructured film, in contrast to the stereotypical cobblestone pattern in control cells exposed to no film or unstructured, flat film (scale bar = 20 μm). Occludin ruffling, as measured by cell perimeter, was increased with nanotopography by 87% over cells alone and 118% over flat (**$p<0.01$). Fluorescence intensity was normalized by number of cells. (c) TEM imaging of the tight junction (TJ) (solid black arrow), adherens junction (AJ) (dashed black arrow), and desmosome (solid white arrow). Cells exposed to unstructured, flat films (Flat) show a partial loss of electron density in the TJ and AJ, relative to no film controls. Cells exposed to nanostructured films (NS) show near complete loss of electron density in the TJ and AJ, as well as partial loss in the underlying desmosome, relative to no film controls (scale bar = 200 nm).

To explore whether down regulation of claudins in keratinocytes is a robust and well-conserved mechanism, we performed analogous experiments in Caco-2 epithelial cells cultured on transwell permeable supports. Cells were either untreated or placed in contact with either an unstructured control film or a nanostructured film. Similar to keratinocytes, staining for claudins-1 and 4 in Caco-2 cells showed reduced localization at cell-cell junctions when cells were in contact with the nanostructures, in comparison to either the cells alone or cells in contact with an unstructured film, with claudin-1 being reduced by the greatest extent (Figure 3a). In contrast to claudins-1 and 4,

immunostaining of the TJ protein occludin was preserved. However, instead of the stereotypical cobblestone pattern demonstrated by the control cells, occludin staining demonstrated a ruffled pattern when cells were exposed to nanostructured films, a pattern which has previously been reported with disruption of other TJ proteins such as ZO-1[16] (Figure 3a).

To further explore the structural effect of nanotopography on TJ's, we characterized TJ structure in Caco-2 cells by transmission electron microscopy (TEM) (Figure 3c). Cells in contact with no film showed canonical cellular junction morphology, consisting of an apically located electron-dense TJ and a subjacent adherens junction (AJ) and desmosome. Cells in contact with the unstructured, flat film showed partially decreased electron density in both the TJ and AJ, as well as blurring of the boundaries between these two types of junctions. In cells treated with nanostructured film, the electron density of both the TJ and AJ were completely abrogated, suggesting significant loss of proteins and cytoskeleton within these complexes in response to nanotopography. In addition, there is loss of intermediate filaments near the desmosome with nanotopography. These data collectively demonstrate that nanotopography induces dramatic remodeling and diminishment of epithelial TJs, as well as other cell-cell adhesions.

To explain the structural changes in TJs discussed above, we hypothesized that epithelial cell interaction with nanotopography mediates changes in the actin cytoskeleton underlying TJs. It is well established that cells can bind to nanotopography[18–20], typically by recognizing conserved binding sequences in proteins absorbed onto the biomaterial[21]. This protein recognition is most often mediated by integrins, transmembrane cell surface receptors which serve as a link between the ECM and the actin cytoskeleton[22]. Integrin binding triggers a phosphorylation cascade that recruits and assembles a focal adhesion complex and culminates in phosphorylation and activation

of myosin[23]. Activation of myosin, in turn, alters the actin cytoskeleton, which can lead to increased paracellular permeability[24,25].

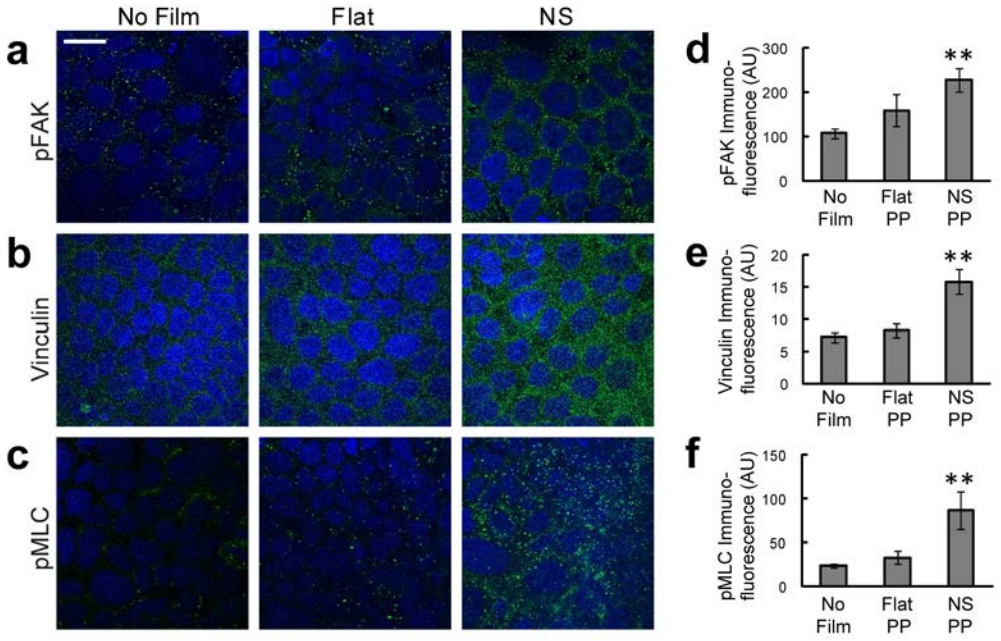


**Figure 4**

Nanotopography leads to clustering of focal adhesion proteins and activation of myosin light chain. (a - c) In Caco-2 cells, exposure to the nanostructured film (NS) leads to increased staining of pFAK, vinculin, and pMLC, relative to controls cells exposed to either no film or to flat, unstructured film (Flat) (scale bar = 20 μm). Nuclear staining is highlighted by DAPI in blue, while protein immunostaining is highlighted in green. (d-f) pFAK was increased by 112% and 43% compared with the no film or flat film controls respectively (**$p<0.01$). Vinculin was increased by 117% and 91% compared with the no film or flat film controls respectively (**$p<0.01$). pFAK was increased by 263% and 161% compared with the no film or flat film controls respectively (**$p<0.01$).

Immunofluorescence was used to investigate the effects of nanotopography on focal adhesion complexes and myosin activation within cells. Cells in contact with the nanostructures showed increased punctate staining of phosphorylated focal adhesion kinase (pFAK), which is phosphorylated upon integrin-ligand binding and subsequently recruits other components of the adhesion complex[26] (Figure 4a). Consistent with this increase in pFAK, clustering of vinculin – another downstream component of the focal adhesion complex – was also increased in response to nanotopography (Figure 4b). To assess whether these increases in focal adhesion proteins were associated with myosin activation, immunostaining for phosphorylated myosin light chain was performed. As with pFAK and vinculin, pMLC clustering was increased exclusively in cells exposed to the nanostructured films (Figure 4c). These data collectively demonstrate that integrin-binding to nanotopography induces formation of focal adhesion complexes and activation of actomyosin contractility.

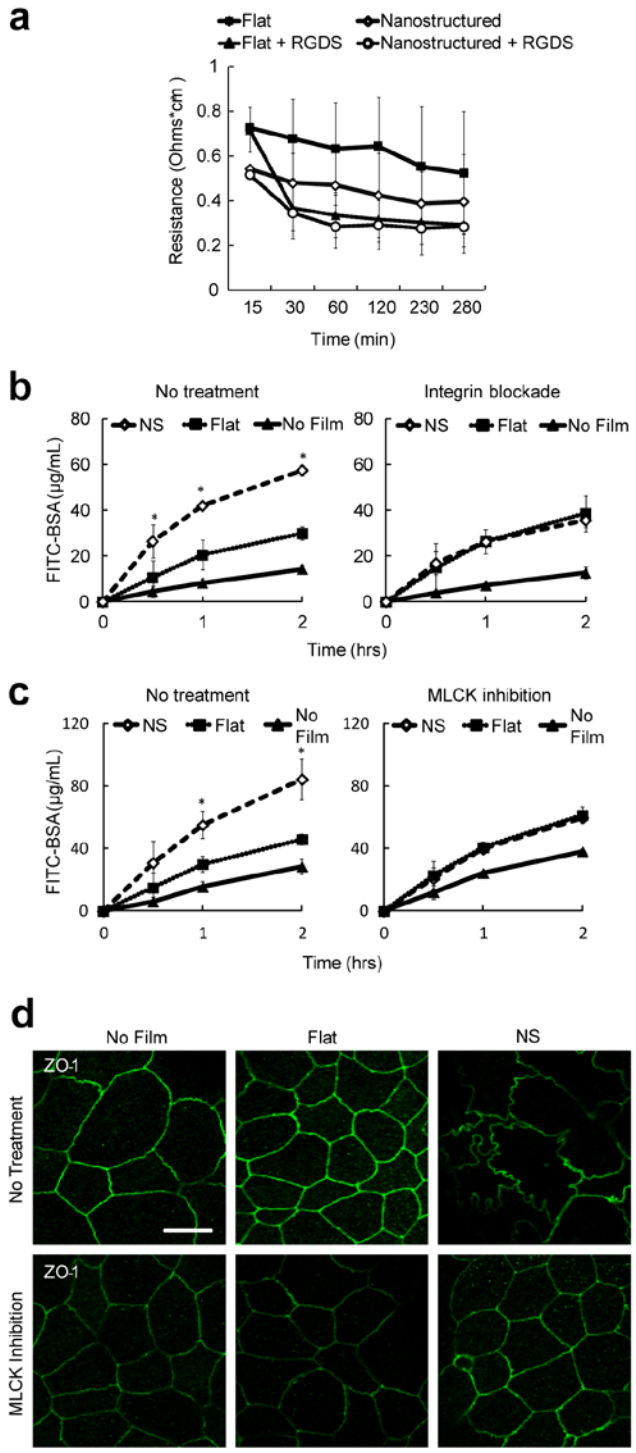
a
Flat
Nanostructured
Flat + RGDS
Nanostructured + RGDS
Resistance (Ohms*cm²)
Time (min)
b
No treatment
Integrin blockade
NS
Flat
No Film
FITC-BSA (µg/mL)
Time (hrs)
c
No treatment
MLCK inhibition
NS
Flat
No Film
FITC-BSA (µg/mL)
Time (hrs)
d
No Film
Flat
NS
No Treatment
MLCK Inhibition
ZO-1

**Figure 5**

Nanotopography-mediated drug delivery and downregulation of TJs requires integrin activation and phosphorylation of myosin light chain. (a) The integrin-binding RGDS peptide is sufficient to recapitulate the effect of nanotopography on Caco-2 permeability. As expected, cells exposed to nanostructured films without RGDS (open diamond) showed decreased transepithelial electrical resistance (TEER) relative to controls exposed to flat, unstructured film without RGDS (solid square). The addition of RGDS led to diminishment of TEER in both nanostructured and flat film groups, abrogating the previous difference observed in the absence of RGDS (n=4). (b) Integrin function is necessary for nanotopography-mediated drug transport. In the absence of integrin blockade, nanostructured films (NS) significantly increase transport of FITC-BSA (left panel) (*$p<0.05$). In the presence of integrin blockade, this nanotopography-induced increase in BSA transport is abolished, and there are no differences between the nanotopography and unstructured, flat film groups. (n=4) (c) Myosin light chain kinase (MLCK) function is necessary for nanotopography-mediated drug transport. In the absence of MLCK blockade, nanostructured films (NS) significantly increase transport of FITC-BSA (left panel) (*$p<0.05$). In the presence of MLCK blockade, this nanotopography-induced increase in BSA transport is abolished, and there are no differences between the nanotopography and unstructured, flat film groups. (n=4) (d) Myosin light chain kinase (MLCK) function is necessary for nanotopography-mediated changes in TJ structure. ZO-1 immunostaining adopts a ruffled pattern in Caco2 cells exposed to nanostructured films (NS), indicating a disruption of the TJ complex. After addition of MLCK inhibitor, this ruffling is abolished, and cells exposed to nanotopography resume the canonical ZO-1 pattern shown in control cells exposed to either no film or flat, unstructured films.

To investigate whether integrin engagement with the film and subsequent focal adhesion complex formation is sufficient for drug transport facilitated by nanotopography, we first treated cells with RGD peptide, which is the recognition sequence for some integrins and can artificially induce integrin clustering[27]. RGD treatment of the cells was found to fully mimic the drug-enhancing effects of nanotopography and nullified the previously observed differences in drug delivery between unstructured and nanostructured films (Figure 5a).

To explore whether integrins were necessary for nanotopography-induced TJ remodeling, we used antibody blockade to prevent integrin binding and downstream clustering of focal adhesions. Specifically, integrins alpha V and beta 1 were specifically inhibited because these integrins are common to the majority of RGD sequence binding integrin pairs[28]. As expected, nanotopography significantly enhanced drug delivery in the absence of integrin blockade. With integrin blockade, however, this finding was completely abrogated, with no difference in drug transport between the nanostructured film and the unstructured films (Figure 5b). Therefore, integrin binding appears to be both sufficient and necessary for nanotopography-mediated enhancement of drug delivery.

To assess whether downstream myosin phosphorylation and activation is also necessary for nanotopography-induced changes, cells were treated with permeant inhibitor of myosin light chain kinase (PIK). As with inhibition of integrin clustering, inhibition of myosin phosphorylation abolished the enhancement of drug delivery by nanotopography (Figure 5c). To investigate whether myosin phosphorylation was also required for nanotopography-induced changes in TJ structure, cells were treated with PIK, and TJ morphology was assessed by immunostaining for ZO-1. Treatment with PIK abolished the previously observed ruffling pattern of ZO-1 when cells were placed in contact with the nanostructured film (Figure 5d). Together, the above functional

studies demonstrate that both integrin and myosin activation are requisite for nanotopography-mediated remodeling of the epithelial TJ and increase in epithelial permeability.

Materials with controlled nanotopography have recently been explored in the drug delivery field. Other groups have shown that nanotopography can increase drug delivery via endocytosis[29,30]. We have shown previously that a purely topographical cue can significantly increase the transport of high molecular weight molecules across a simple epithelial monolayer by paracellular transport[16]. In this study, we show for the first time that nanotopography significantly enhances transdermal delivery of a high molecular weight therapeutic *in vivo*. To better understand these phenomena, we have identified a molecular mechanism in which nanotopography binds to cell surface integrins, induces clustering of focal adhesion proteins and actomyosin activation, and ultimately remodels components of the tight junction barrier to increase paracellular permeability (Figure 6).

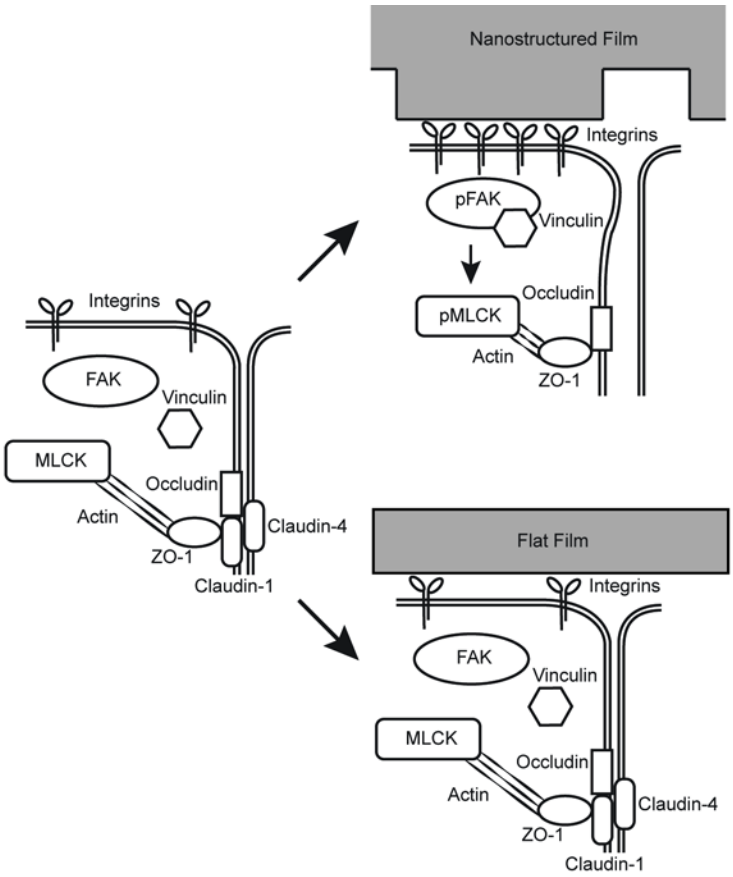

**Figure 6**

Nanotopography downregulates epidermal tight junctions via integrin activation and myosin light chain phosphorylation. Proposed mechanism for nanotopography-mediated enhancement of transdermal drug delivery: Integrins bind to adsorbed proteins on the nanotopography and induce downstream clustering of focal adhesion proteins such as pFAK and vinculin. Formation of focal adhesions, in turn, leads to phosphorylation of myosin light chain and increased myosin contraction of the actin cytoskeleton. Actin dynamics ultimately remodel and downregulate proteins at the epidermal tight junction, thereby allowing increased paracellular transport within the epidermis. By contrast, we propose that the lack of topography on the flat surfaces fails to induce integrin clustering and the downstream initiation of focal adhesions and actomyosin activation (right lower image).

What specific characteristics of the nanotopography are driving these effects? Although all of the nanostructured films we tested in this study effectively remodeled tight junctions, we found material-dependent differences between PEEK and polypropylene in human multilayered keratinocytes, with PEEK inducing more downregulation of claudins-1 and 4. As flat controls for both materials did not induce any changes in tight junctions, this material difference is unlikely to be due to chemical effects on the keratinocytes. Rather, the discrepancy is more likely attributable to differences in pliability and stiffness of the material, leading to differences in tension experienced within the cells. Other variables that could potentially have effects on drug delivery and be variably tuned include the aspect ratio of the fibers, the pitch between different fibers, and the surface area of the nanostructures [31–36]. It will be interesting in future studies to systematically define these parameter windows to maximize the biological effect of nanotopography. In addition

to varying the parameters of the devices themselves, it would be valuable to explore lower molecular weight therapeutics as well, in order to delineate the relationship between molecular weight, topography, and delivery rate.

Although we demonstrated that focal adhesion clustering and myosin activation are necessary for nanotopography-mediated drug delivery, it would be valuable to explore other mechanisms that may be acting in parallel with this. In particular, cells that are not in direct contact with the nanotopography also demonstrate dramatic reductions in tight junction proteins, suggesting that there is paracellular signaling from upper cells of the stratum granulosum downwards to the lower skin layers. This indirect effect on cells that are not in contact with the microneedles is further suggested by our *in vivo* rabbit data, in which microneedles likely do not penetrate to the lower epidermis yet still deliver etanercept as effectively as in rats. Interestingly, preliminary mRNA expression data from our laboratory identify a cellular adhesion/polarity pathway that is downregulated in response to nanotopography. Key signaling molecules in the establishment of cell polarity, such as Tiam1, Rac1, and aPKC, are all suppressed in Caco-2 cells after exposure to nanotopography. Such loss of polarity could provide another mechanism through which nanotopography alters epithelial permeability. For example, nanotopography may be promoting de-differentiation or trans-differentiation of epithelial cells, similar to what occurs in epithelial to mesenchymal transition (EMT)[37,38].

Regarding clinical usage, the impact of transdermally-delivered biologic therapeutics such as etanercept on rheumatoid arthritis and psoriasis would be significant. Currently, medications within this family are administrated subcutaneously, intramuscularly, or intravenously, all of which are inconvenient and painful for the patient. Exchanging this current standard of care with a longer lasting transdermal device would likely improve patient compliance, as well as offer more

biologically effective dosing with fewer peaks and troughs and less hepatic metabolism. Transdermal delivery also opens up the possibility of using biologics for localized, as opposed to systemic, therapy. For example, local topical agents for psoriasis are currently limited in scope, comprised primarily of corticosteroids and vitamin D analogues. Being able to deliver small doses of the appropriate biologic locally to the skin would expand upon this repertoire significantly.

**References**


(1) Celli, A.; Zhai, Y.; Jiang, Y. J.; Crumrine, D.; Elias, P. M.; Feingold, K. R.; Mauro, T. M. *Exp. Dermatol.* **2012**, *21* (10), 798–801.

(2) Kirschner, N.; Houdek, P.; Fromm, M.; Moll, I.; Brandner, J. M. *Eur. J. Cell Biol.* **2010**, *89* (11), 839–842.

(3) Roussel, A. J. J.; Knol, A. C.; Bourdeau, P. J.; Bruet, V. *J. Comp. Pathol.* **2014**, *150* (1), 35–46.

(4) Furuse, M.; Hirase, T.; Itoh, M.; Nagafuchi, A.; Yonemura, S.; Tsukita, S. *J. Cell Biol.* **1993**, *123* (6), 1777–1788.

(5) Fanning, A. S.; Jameson, B. J.; Jesaitis, L. A.; Anderson, J. M. *J. Biol. Chem.* **1998**, *273* (45), 29745–29753.

(6) Furuse, M.; Fujita, K.; Hiiragi, T.; Fujimoto, K.; Tsukita, S. *J. Cell Biol.* **1998**, *141* (7), 1539–1550.

(7) Sugawara, T.; Iwamoto, N.; Akashi, M.; Kojima, T.; Hisatsune, J.; Sugai, M.; Furuse, M. *J. Dermatol. Sci.* **2013**, *70* (1), 12–18.

(8) Furuse, M.; Hata, M.; Furuse, K.; Yoshida, Y.; Haratake, A.; Sugitani, Y.; Noda, T.; Kubo,

A.; Tsukita, S. *J. Cell Biol.* **2002**, *156* (6), 1099–1111.

(9) Deli, M. A. *Biochim. Biophys. Acta - Biomembr.* **2009**, *1788* (4), 892–910.

(10) Findley, M. K.; Koval, M. *IUBMB Life* **2009**, *61* (4), 431–437.

(11) Tsukita, S.; Furuse, M. *J. Cell Biol.* **2000**, *149* (1), 13–16.

(12) Broderick, K. E.; Chan, A.; Lin, F.; Shen, X.; Kichaev, G.; Khan, A. S.; Aubin, J.; Zimmermann, T. S.; Sardesai, N. Y. *Mol. Ther. — Nucleic Acids* **2012**, *1* (2), e11.

(13) Elsabahy, M.; Foldvari, M. *Curr. Pharm. Des.* **2013**, *19* (41), 7301–7315.

(14) Brown, M. B.; Traynor, M. J.; Martin, G. P.; Akomeah, F. K. *Methods Mol. Biol.* **2008**, *437*, 119–139.

(15) Rao, R.; Nanda, S. *J. Pharm. Pharmacol.* **2009**, *61* (6), 689–705.

(16) Kam, K. R.; Walsh, L. A.; Bock, S. M.; Koval, M.; Fischer, K. E.; Ross, R. F.; Desai, T. A. *Nano Lett.* **2013**, *13* (1), 164–171.

(17) Godin, B.; Touitou, E. *Adv. Drug Deliv. Rev.* **2007**, *59* (11), 1152–1161.

(18) Dalby, M. J.; Riehle, M. O.; Sutherland, D. S.; Agheli, H.; Curtis, A. S. G. *Eur. J. Cell Biol.* **2004**, *83* (4), 159–169.

(19) Dalby, M. J. *Med. Eng. Phys.* **2005**, *27* (9), 730–742.

(20) Dalby, M. J. *Int. J. Nanomedicine* **2007**, *2* (3), 373–381.

(21) Anselme, K.; Davidson, P.; Popa, A. M.; Giazzon, M.; Liley, M.; Ploux, L. *Acta Biomater.* **2010**, *6* (10), 3824–3846.

(22) Biggs, M. J. P.; Richards, R. G.; Dalby, M. J. *Nanomedicine-Nanotechnology Biol. Med.* **2010**, *6* (5), 619–633.

(23) Jockusch, B. M.; Bubeck, P.; Giehl, K.; Kroemker, M.; Moschner, J.; Rothkegel, M.; Rudiger, M.; Schluter, K.; Stanke, G.; Winkler, J. *Annu. Rev. Cell Dev. Biol.* **1995**, *11* (1), 379–416.

(24) Shen, L.; Black, E. D.; Witkowski, E. D.; Lencer, W. I.; Guerriero, V.; Schneeberger, E. E.; Turner, J. R. *J. Cell Sci.* **2006**, *119* (10), 2095–2106.

(25) Tinsley, J. H.; de Lanerolle, P.; Wilson, E.; Ma, W. Y.; Yuan, S. Y. *Am. J. Physiol. Physiol.* **2000**, *279* (4), C1285–C1289.

(26) Schaller, M.; Hildebrand, J.; Shannon, J.; Fox, J.; Vines, R.; Parsons, J. *Mol. Cell. Biol.* **1994**, *14* (3), 1680–1688.

(27) Maheshwari, G.; Brown, G.; Lauffenburger, D. A.; Wells, A.; Griffith, L. G. *J. Cell Sci.* **2000**, *113 ( Pt 1*, 1677–1686.

(28) Ruoslahti, E. *Annu. Rev. Cell Dev. Biol.* **1996**, *12* (1), 697–715.

(29) Adler, A. F.; Leong, K. W. *Nano Today* **2010**, *5* (6), 553–569.

(30) Dalby, M. J.; Berry, C. C.; Riehle, M. O.; Sutherland, D. S.; Agheli, H.; Curtis, A. S. . *Exp. Cell Res.* **2004**, *295* (2), 387–394.

(31) Sjöström, T.; Dalby, M. J.; Hart, A.; Tare, R.; Oreffo, R. O. C.; Su, B. *Acta Biomater.* **2009**, *5* (5), 1433–1441.

(32) Takagi, J.; Petre, B. M.; Walz, T.; Springer, T. A. *Cell* **2002**, *110* (5), 599–511.

(33) Kim, D.-H.; Kim, P.; Suh, K.; Kyu Choi, S.; Ho Lee, S.; Kim, B. *Conf. Proc. ... Annu. Int. Conf. IEEE Eng. Med. Biol. Soc. IEEE Eng. Med. Biol. Soc. Conf.* **2005**, *4*, 4091–4094.

(34) Lee, J.; Kang, B. S.; Hicks, B.; Chancellor Jr., T. F.; Chu, B. H.; Wang, H.-T.; Keselowsky,

B. G.; Ren, F.; Lele, T. P. *Biomaterials* **2008**, *29* (27), 3743–3749.

(35) Balaban, N. Q.; Schwarz, U. S.; Riveline, D.; Goichberg, P.; Tzur, G.; Sabanay, I.; Mahalu, D.; Safran, S.; Bershadsky, A.; Addadi, L.; Geiger, B. *Nat. Cell Biol.* **2001**, *3* (5), 466–472.

(36) Besser, A.; Safran, S. A. *Biophys. J.* **2006**, *90* (10), 3469–3484.

(37) Ikenouchi, J.; Matsuda, M.; Furuse, M.; Tsukita, S. *J. Cell Sci.* **2003**, *116* (10), 1959–1967.

(38) Yang, Z. B.; Rayala, S.; Nguyen, D.; Vadlamudi, R. K.; Chen, S.; Kumar, R. *Cancer Res.* **2005**, *65* (8), 3179–3184.

# Appendix 1 – The effect on nanotopography on macrophage polarization and cytokine production

## Introduction

A common issue with medical devices and other implants that put nonnative materials into direct and prolonged contact with the body is biofouling, inflammation, and fibrosis. Contact of biomaterials with biological fluid immediately results in the adsorption of proteins onto the surface of the material. These proteins serve as cellular receptors for interaction and adhesion.[1] It is well established that modifying the nanotopography of a surface influences the adsorption of proteins and other biomolecules.[2–6] Increased surface roughness of poly (methyl methacrylate) PMMA increased hydrophobicity, which increased protein adsorbtion.[2] Decreasing the pore size, 45 to 2.2 nm, on silica particles decreased adsorption of bovine serum albumin.[6] Therefore, modification of biomaterial surfaces can be a tool to direct cellular interaction and adhesion. Indeed, surface alteration has been shown to effect the extent of cellular adhesion.[2,7–13] Increasing the surface roughness of PMMA increased cellular adhesion of chick embryo vascular and corneal explant cells, probably due to changes in fibronectin adsorption.[2] The amount of protein adsorption paralleled the adherence of human osteoblast-like cells on titanium surfaces of different roughnesses.[8] The adherence to and cellular interaction of immune cells such as macrophages and monocytes with biomaterials influence the immunogenicity of the biomaterial and could direct the immune response. The ability to direct the surface material inflammatory response would be a powerful tool. Inflammatory responses would be beneficial for applications in immunization for instance. A biomaterial that would not necessarily cause an immune reaction on its own, but that would amplify the immune response of a concurrently administered antigen would be very beneficial. Particularly, it would be beneficial if the material could

present the antigen in such a way that could skew immunity towards cell-mediated immunity.[14] Certain nanotopographies have been shown to increase the inflammatory response.[15–17] Polytetrafluoroethylene materials with increasing intranodal distances showed increased proinflammatory cytokine production compared to nonporous material.[17] Macrophages showed decreased adhesion and increased proinflammatory cytokine production on nanowires.[15] Recent discoveries in immunology have shown that macrophage activation is more complicated than just an active versus inactive phenotypes. There are multiple subsets of macrophages that are differentially activated and serve difference functions.[18,19] The most basic division between macrophage subtypes are M1 or pro-inflammatory and M2 or anti-inflammatory and pro-wound healing. These different subtypes can be differentiated by differential surface receptor expression and cytokine production. We investigated the immunogenicity of two different low aspect ratio nanotopographical patterns of two different materials (Figure 1) by examining cytokine production and mRNA transcript levels.

P(1.5)

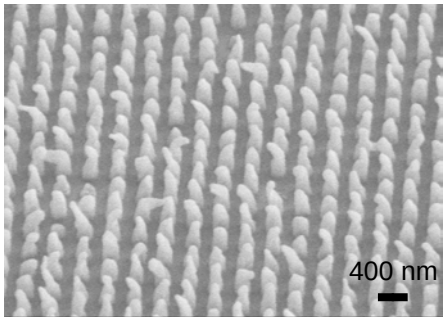


Aspect Ratio = 1.5

S(0.5, 1.4, 3.4)

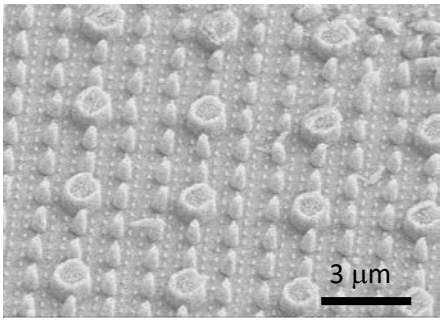


Aspect Ratios = 0.5, 1.4, 3.4

Figure 1 - Scanning electron microscopy images of nanostructured films. Films are named by the polymer type (P = polypropylene, S = polystyrene) and the aspect ratio (AR) of the features (AR = height/width)

**Results**

Macrophages were cultured on tissue culture plastic (TCPS), unimprinted polystyrene (UIPS), S(0.5, 1.4, 3.4) (DN(3)), unimprinted polypropylene (UIPP), or P(1.5) (DN2) for 24 or 48 hours. The amount of cytokine released into the media was measured by a 20-plex luminex assay. Growth factors measured were FGF-basic and VEGF. Chemokines measured were IP-10, KC, MCP-1, MIG, and MIP-1 alpha. Cytokines measured were GM-CSF, IFN-gamma, IL-1 alpha, IL-1 beta, IL-2, IL-4, IL-5, IL-6, IL-10, IL-12, IL-13, IL-17, and TNFa. (Figure 2) Lipopolysaccharide was used as a positive control of inflammation and was significantly higher than all other conditions, but is not shown here for ease of examining the specific effect of nanotopopgraphy versus flat film. Interleukin (IL)-1 beta, tumor necrosis factor alpha (TNFa), macrophage chemotactic protein 1 (MCP-1, CCL2), IL-4, and IL-5 showed reduced levels when cultured on S(0.5, 1.4, 3.4) as compared to UIPS at 48 hours. This suggests that nanotopography decreases inflammatory cytokine production, however the magnitude of this decrease is small. No statistically significant difference was seen between macrophages cultured on P(1.5) versus UIPP, however overall there was a trend of nanostructures decreasing cytokine production as compared to the same material but unimprinted.

To determine whether this down regulation in cytokine expression was due to a change in polarization, macrophage monocytes were cultured on the same surfaces: TCPS, UIPS, S(5), UIPP, and P(1.5) for 24 hours and the expression of six genes were measured.(Figure 3) IL-1 beta and IL-6 are over expressed in M1 polarized macrophages, while IL-10, arginase 1, TGF

beta and IGF-1 are upregulated in M2 polarization. M2 polarization can be divided into M2a (arg1, IGF-1, IL-10), M2b (IL-6, IGF-1), and M2c (TGFb, IL-10).[20] There was no statistically significant difference in expression of these cytokines due to presence of topography. However, there was a difference in expression based upon the material of the thin film. Both nanostructured and flat polypropylene films higher levels expression of Il-6, while the other targets were all reduced in comparison. This suggests a possible wound healing skewing of macrophage polarization. The polystyrene on the other hand showed high levels of expression of all targets except TGFb and IGF-1. This suggests the material skews macrophage polarization towards an M2 phenotype, but does not correspond directly to M2a, M2b or M2c. A caveat of these results is that the glue used to adhere the films to the TCPS also increased expression of all targets, though had a lower effect on TGFb and IGF-1. Therefore, the effect seen with the polystyrene is more striking since it overrides and decreases baseline expression of inflammatory genes upregulated by the presence of glue. Since the polystyrene films had the same pattern of expression as the TCPS with glue, further investigation is necessary to determine whether the effect was due to the presence of glue or due to the material itself. Also, a higher aspect ratio polystyrene nanostructured film was used (S(5)) in this study. It would be interesting to confirm whether the cytokine release results seen with S(0.5, 1.4, 3.4) is also reflected by mRNA expression.

**a. IL-1 beta**

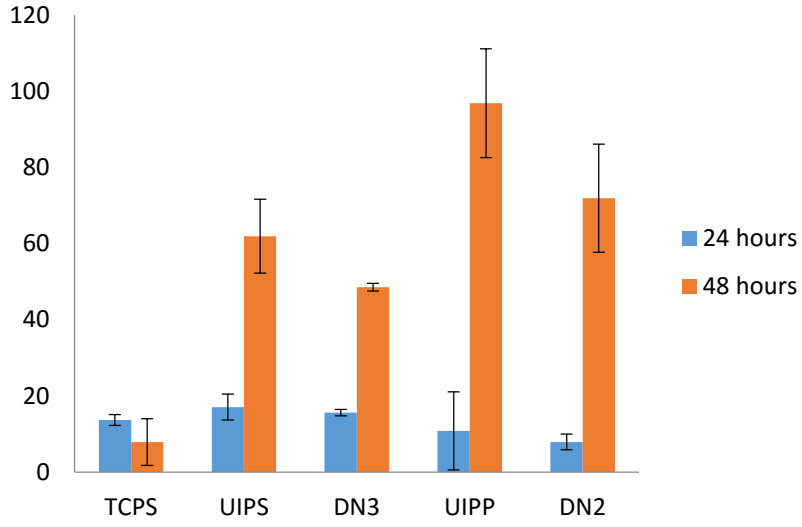


**b. TNF-alpha**

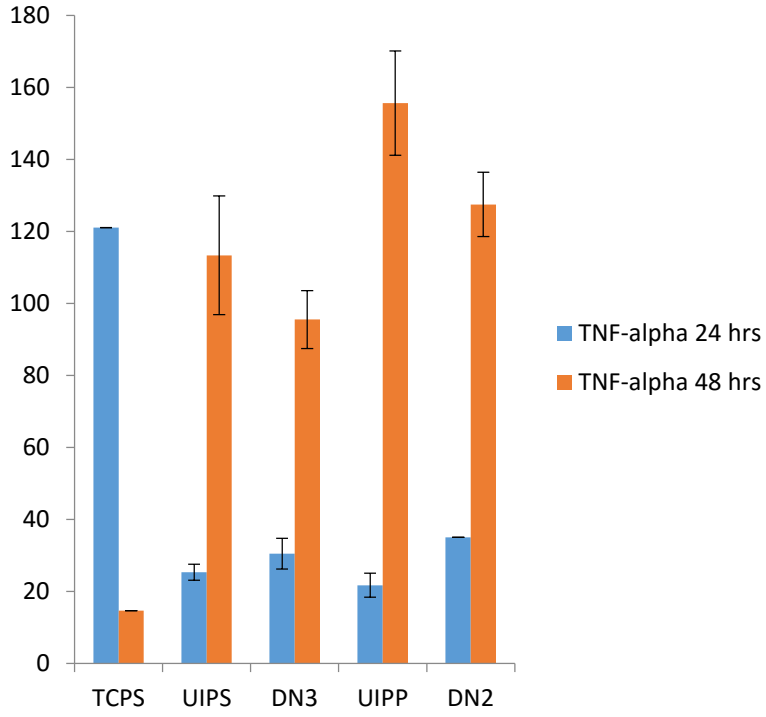

**c. MCP-1**

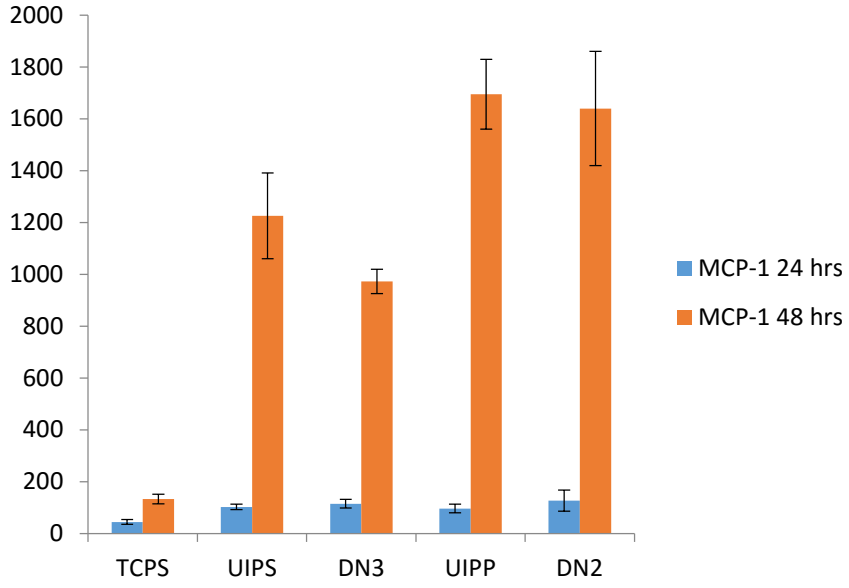
2000
1800
1600
1400
1200
1000
800
600
400
200
0
TCPS
UIPS
DN3
UIPP
DN2
MCP-1 24 hrs
MCP-1 48 hrs

**d. IL-4**

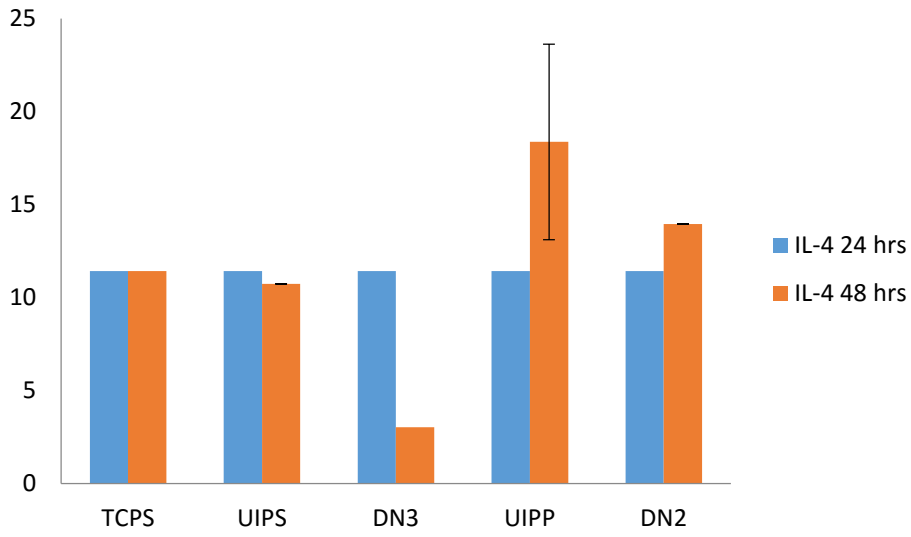
25
20
15
10
5
0
TCPS
UIPS
DN3
UIPP
DN2
IL-4 24 hrs
IL-4 48 hrs

**e. IL-5**

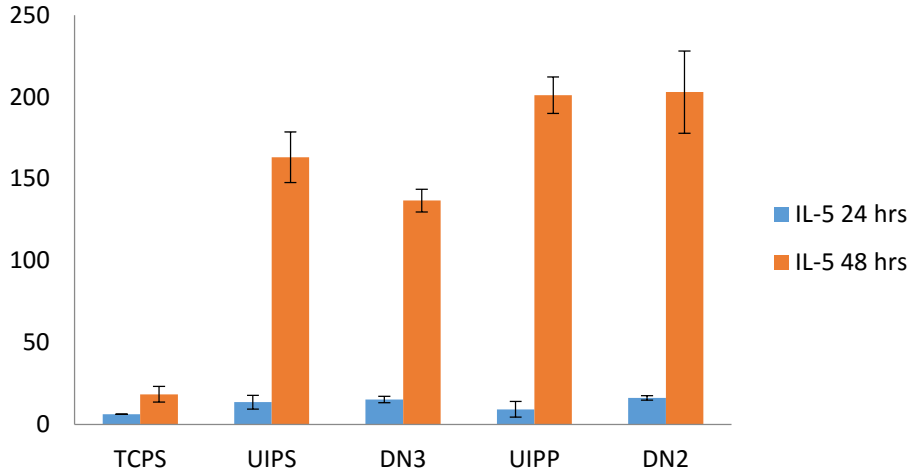


**f. IL-1 alpha**

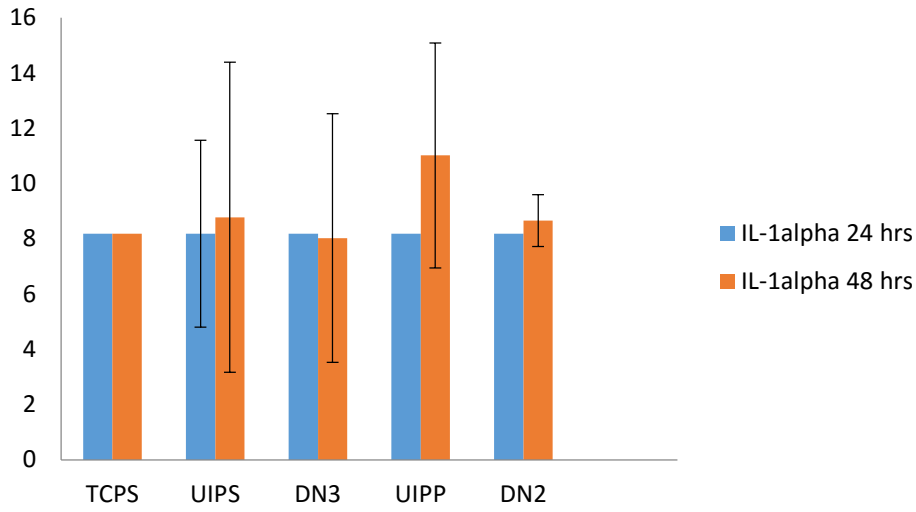

**g. IL-6**

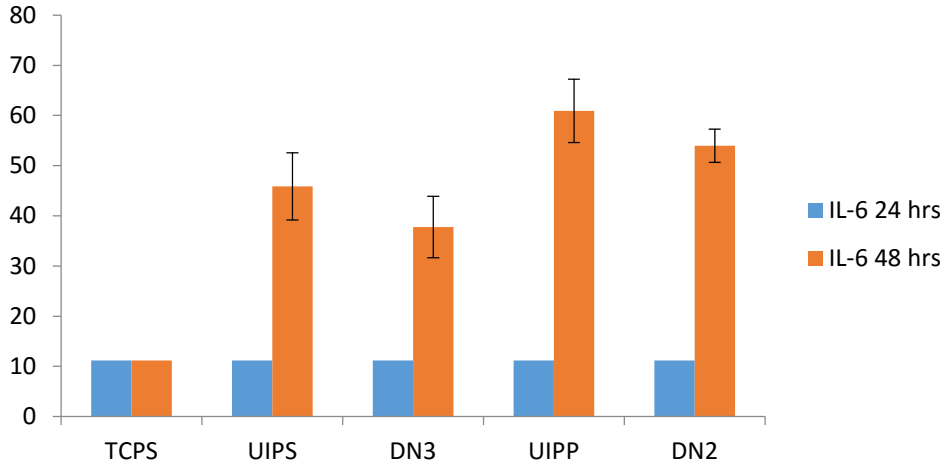


**h. IL-12**

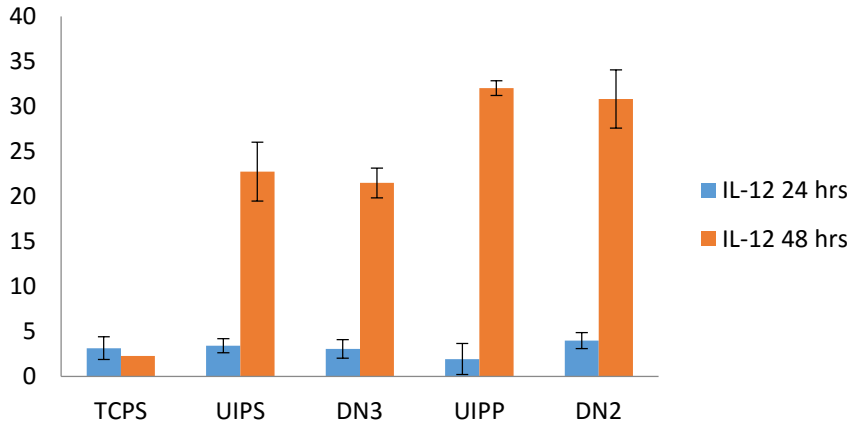


**i. IL-17**

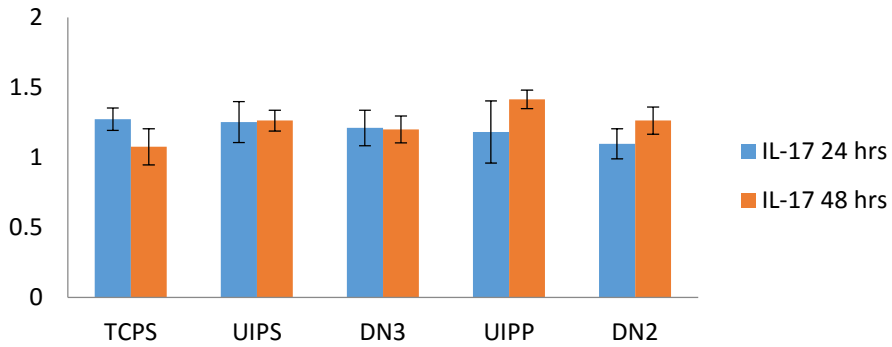

**j. MIP-1 beta**

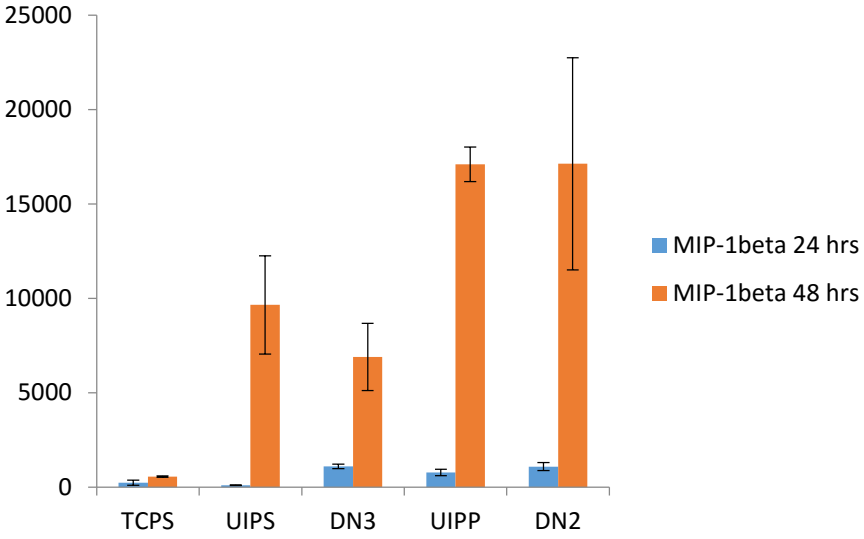


**k. IP-10**

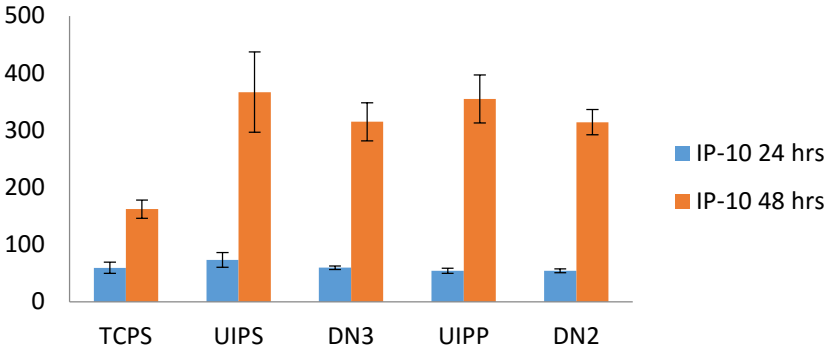


**l. IL-2**

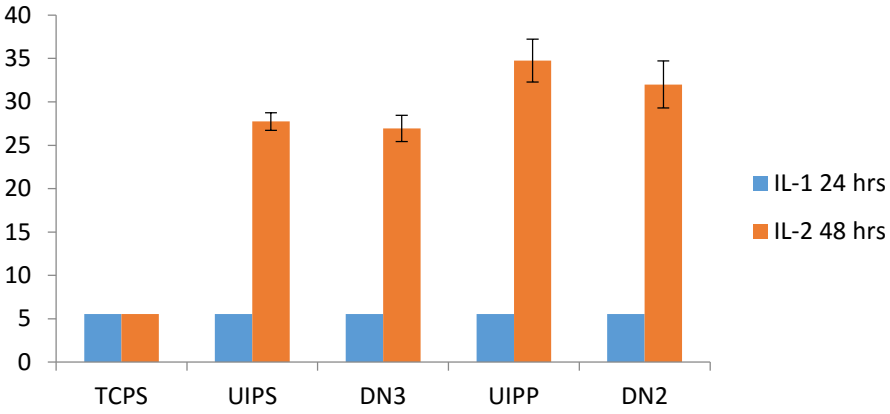

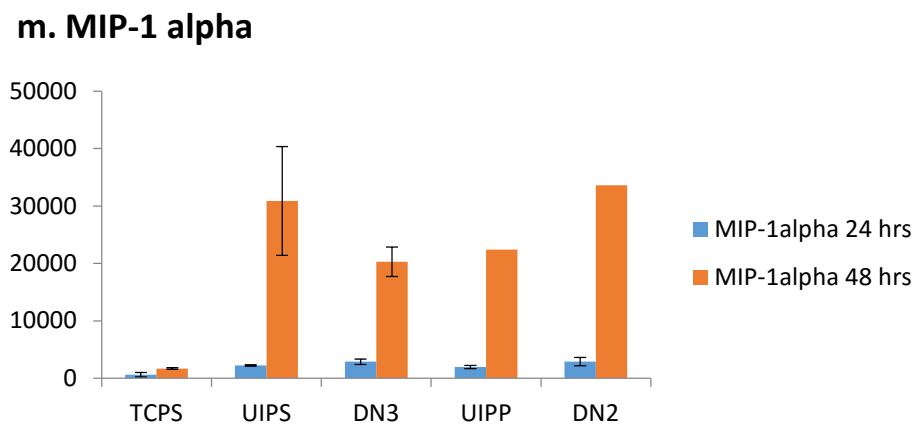


Figure 2 – Luminex assay measurement of cytokine released (pg/mL) by macrophage monocytes grown on tissue culture plastic (TCPS), unimprinted polystyrene (UIPS), S(0.5, 1.4, 3.4) (DN(3)), unimprinted polypropylene (UIPP), or P(1.5) (DN2) for 24 or 48 hours.

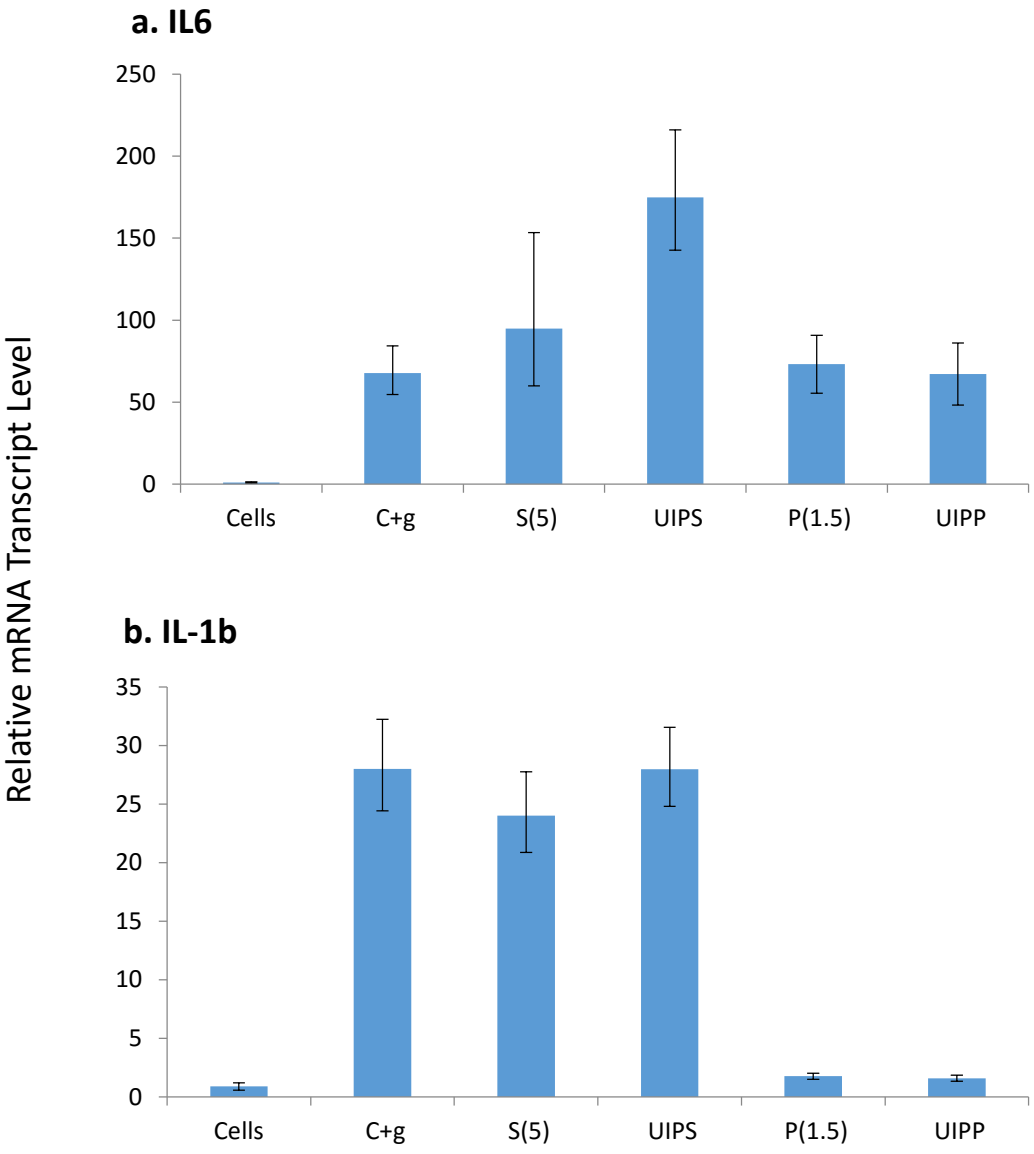
a. IL6
Relative mRNA Transcript Level
250
200
150
100
50
0
Cells
C+g
S(5)
UIPS
P(1.5)
UIPP
b. IL-1b
35
30
25
20
15
10
5
0
Cells
C+g
S(5)
UIPS
P(1.5)
UIPP

**c. IL-10**

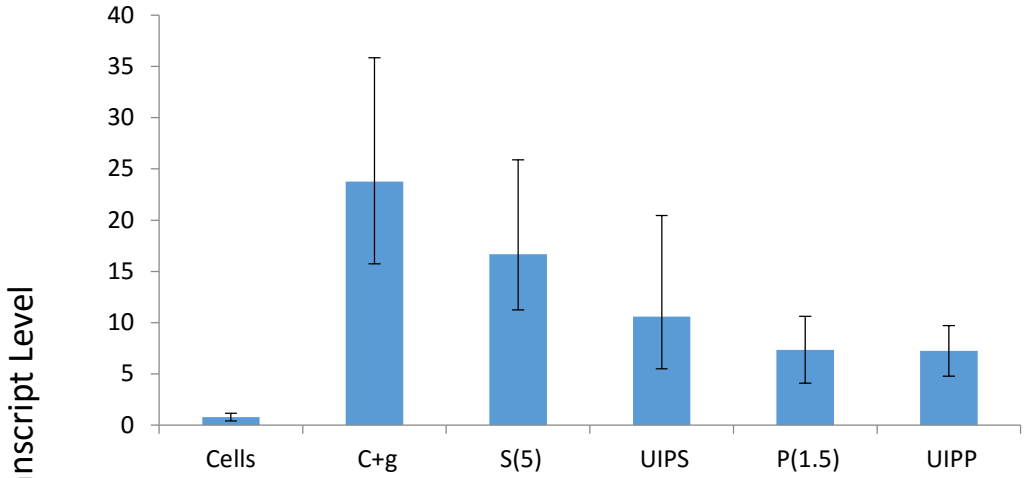
Relative mRNA Transcript Level
40
35
30
25
20
15
10
5
0
Cells
C+g
S(5)
UIPS
P(1.5)
UIPP

**d. Arg-1**

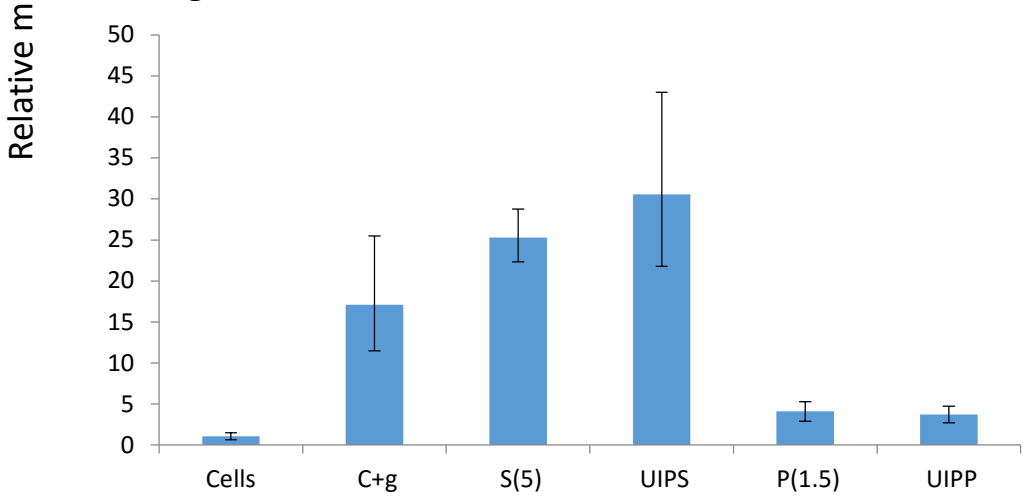
50
45
40
35
30
25
20
15
10
5
0
Cells
C+g
S(5)
UIPS
P(1.5)
UIPP

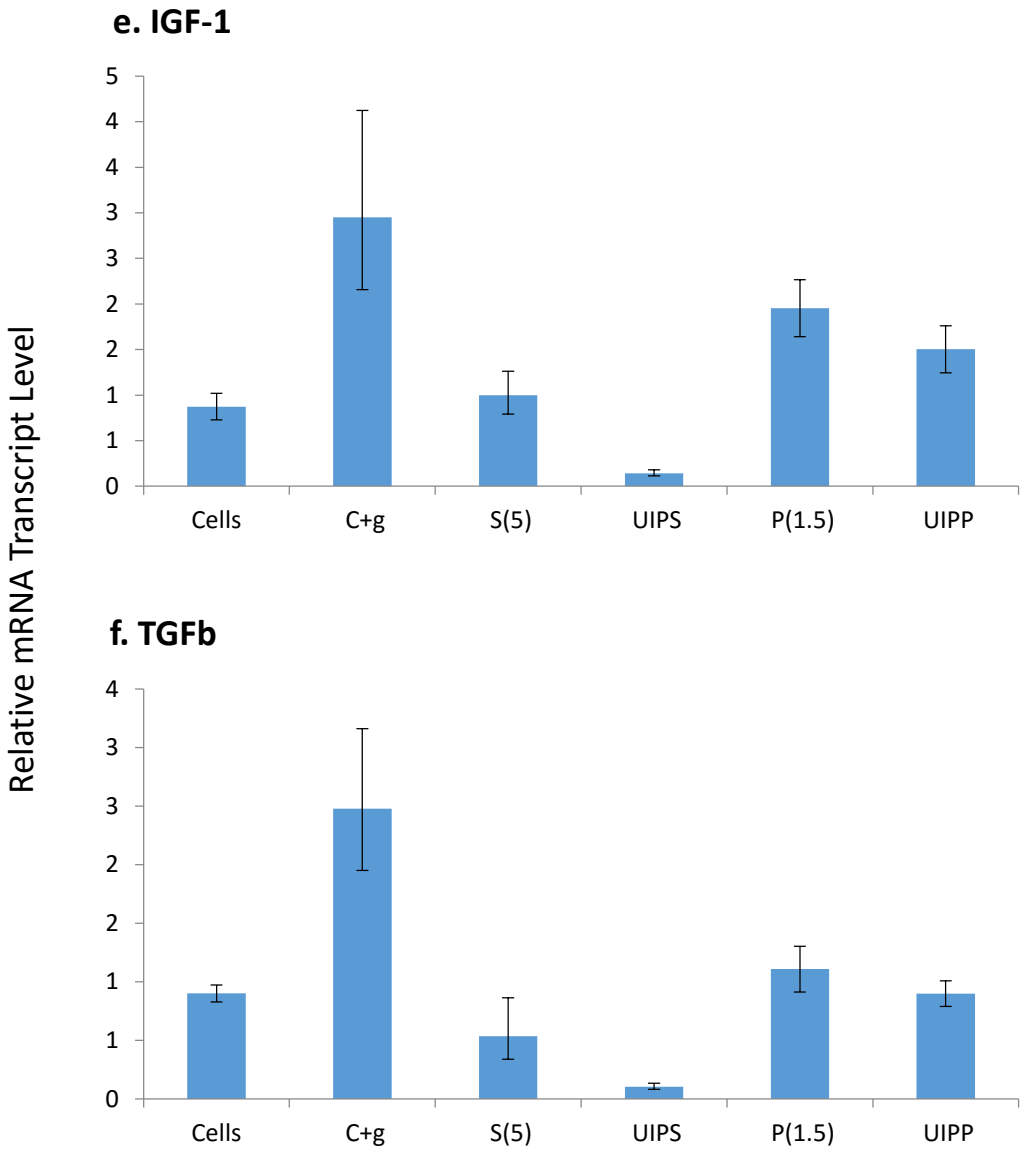


Figure 3 - Macrophage polarization qPCR. Cells were cultured on TCPS (cells), TCPS in the presence of glue (c+g), S(5), UIPS, P(1.5) or UIPP for 24 hours. mRNA expression was measured relative to cells cultured on TCPS for IL-6 (a), IL-1b (b), IL-10 (c), arg-1 (d), IGF-1 (e), and TGFb (f).

**References**

1. Balasubramanian, V., Grusin, N. K., Bucher, R. W., Turitto, V. T. & Slack, S. M. Residence-time dependent changes in fibrinogen adsorbed to polymeric biomaterials. *J. Biomed. Mater. Res.* **44,** 253–60 (1999).

2. Lampin, M., Warocquier-Clérout, Legris, C., Degrange, M. & Sigot-Luizard, M. F. Correlation between substratum roughness and wettability, cell adhesion, and cell migration. *J. Biomed. Mater. Res.* **36,** 99–108 (1997).

3. Lück, M., Paulke, B. R., Schröder, W., Blunk, T. & Müller, R. H. Analysis of plasma protein adsorption on polymeric nanoparticles with different surface characteristics. *J. Biomed. Mater. Res.* **39,** 478–85 (1998).

4. McFarland, C. D., Thomas, C. H., DeFilippis, C., Steele, J. G. & Healy, K. E. Protein adsorption and cell attachment to patterned surfaces. *J. Biomed. Mater. Res.* **49,** 200–10 (2000).

5. Denis, F. A. *et al.* Protein Adsorption on Model Surfaces with Controlled Nanotopography and Chemistry. *Langmuir* **18,** 819–828 (2002).

6. Kim, D.-H. *et al.* Modulation of adhesion and growth of cardiac myocytes by surface nanotopography. *Conf. Proc. ... Annu. Int. Conf. IEEE Eng. Med. Biol. Soc. IEEE Eng. Med. Biol. Soc. Conf.* **4,** 4091–4094 (2005).

7. Naji, A. & Harmand, M. F. Study of the effect of the surface state on the cytocompatibility of a Co-Cr alloy using human osteoblasts and fibroblasts. *J. Biomed. Mater. Res.* **24,** 861–71 (1990).

8. Martin, J. Y. *et al.* Effect of titanium surface roughness on proliferation, differentiation,

and protein synthesis of human osteoblast-like cells (MG63). *J. Biomed. Mater. Res.* **29,** 389–401 (1995).

9. Altankov, G., Grinnell, F. & Groth, T. Studies on the biocompatibility of materials: fibroblast reorganization of substratum-bound fibronectin on surfaces varying in wettability. *J. Biomed. Mater. Res.* **30,** 385–91 (1996).

10. Kanagaraja, S., Lundström, I., Nygren, H. & Tengvall, P. Platelet binding and protein adsorption to titanium and gold after short time exposure to heparinized plasma and whole blood. *Biomaterials* **17,** 2225–32 (1996).

11. Steele, J. G., Johnson, G., Griesser, H. J. & Underwood, P. A. Mechanism of initial attachment of corneal epithelial cells to polymeric surfaces. *Biomaterials* **18,** 1541–51 (1997).

12. Balcells, M. & Edelman, E. R. Effect of pre-adsorbed proteins on attachment, proliferation, and function of endothelial cells. *J. Cell. Physiol.* **191,** 155–61 (2002).

13. Lan, S., Veiseh, M. & Zhang, M. Surface modification of silicon and gold-patterned silicon surfaces for improved biocompatibility and cell patterning selectivity. *Biosens. Bioelectron.* **20,** 1697–708 (2005).

14. Jones, K. S. Biomaterials as vaccine adjuvants. *Biotechnol. Prog.* **24,** 807–14

15. Ainslie, K. M., Bachelder, E. M., Sharma, G., Grimes, C. A. & Pishko, M. V. Macrophage cell adhesion and inflammation cytokines on magnetostrictive nanowires. *Nanotoxicology* **1,** 279–290 (2009).

16. Zaveri, T. D. *et al.* Contributions of surface topography and cytotoxicity to the

macrophage response to zinc oxide nanorods. *Biomaterials* **31,** 2999–3007 (2010).

17. Bota, P. C. S. *et al.* Biomaterial topography alters healing in vivo and monocyte/macrophage activation in vitro. *J. Biomed. Mater. Res. A* **95,** 649–57 (2010).

18. Chinetti-Gbaguidi, G., Colin, S. & Staels, B. Macrophage subsets in atherosclerosis. *Nat. Rev. Cardiol.* **12,** 10–7 (2015).

19. Canton, J., Neculai, D. & Grinstein, S. Scavenger receptors in homeostasis and immunity. *Nat. Rev. Immunol.* **13,** 621–34 (2013).

20. Gensel, J. C. & Zhang, B. Macrophage activation and its role in repair and pathology after spinal cord injury. *Brain Res.* **1619,** 1–11 (2015).

# Appendix 2 - Development of a Microneedle-based Transdermal Patch Vaccine for Schistosomiasis and Vaccine Delivery


## Abstract

Nearly 1 billion people are at risk or infected by the blood fluke Schistosoma[1,2] making it the second most devastating parasitic disease in present day. Schistosomiasis is found primarily in tropical and sub-tropical poor communities that lack adequate sanitation and clean drinking water. Current infection control focuses on treatment, but a more effective approach would be attained through prevention by developing a vaccine[1,2]. However, even with the development of a vaccine, current vaccine technology is based primarily on hollow needle syringes that carry a risk of blood borne infection[3] and expensive administration and training costs. The development of a transdermal patch with nanostructured microneedles would simplify the vaccination process, reduce risk of infection, and increase patient compliance. Skin acts as barrier that limits the size of transdermally delivered therapeutics to small molecules[4-6], but the Desai lab is collaborating with Kimberly-Clark to develop a patch to overcome with challenge. Our previous research shows that adding nanostructures to the microneedle surface significantly increases the permeability of skin to larger molecules, for example in delivering therapeutic levels of etanercept in the blood of rabbits[7]. We propose the development of a transdermal microneedle based vaccine for schistosomiasis with cercarial elastase[8-10] as the antigen. We hypothesize that the transdermal vaccine would benefit from access to the extensive immune system within the skin and would target the desired organ and route of infection.


## Introduction

Schistosomiasis is caused by infection from a parasitic worm. Cercaria, the larval form, is released from a snail host into fresh water. When a cercaria encounters a human, it penetrates the skin, matures into an adult schistosome, and lives in blood vessels. When cercaria whose host is not normally human penetrates skin a vigorous immune response, termed 'swimmers itch,' prevents the establishment of infection. It is hypothesized that a vaccine target released during the skin invasion of the parasite would mimic this immunity.

The microneedle device is a patch that can be applied to the skin to deliver a vaccine across the skin. The needles penetrate through the non-viable epidermis into the viable epidermis, reaching far enough to deliver the vaccine but stopping short of stimulating pain-causing nerves or penetrating blood vessels below (Figure 1). Nanostructures (Figure 2) on the surface of these microneedles significantly increase transdermal transport of large biological molecules (IgG, etanercept) across tight junction barriers by facilitating the opening of tight junctions between epithelial cells[7]. We have previously shown nanostructures allow delivery of large biological molecules across the skin, and other microneedle patches are being used or developed for vaccine delivery[15]. The development of a microneedle patch for schistosoma vaccine delivery could be generalized to deliver other large biological molecule vaccines. The development of either passive or active immunity would be a significant step towards limiting the effects of schistosomiasis.

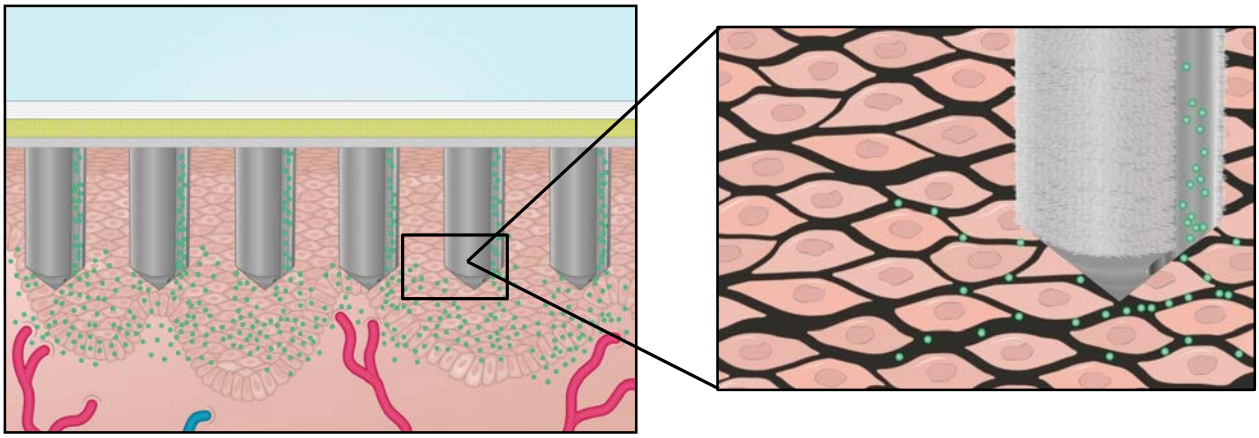

*Figure 1* - Schematic of the microneedle patch. The nanostructured thin films are wrapped around the silicon microneedles to increase transport. Russell Ross, Kimberly-Clark.

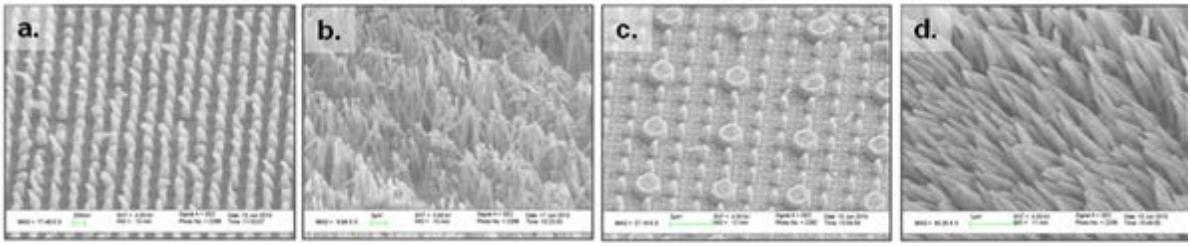


*Figure 2* - **a)** P(1.5), polypropylene with an aspect ratio of 1.5, **b)** P(20), polypropylene with an aspect ratio of 20, **c)** S(0.5, 2.5), polystyrene with an aspect ratio of 0.5 and 2.5, **d)** S(5) polystyrene with an aspect ratio of 5. Russell Ross, Kimberly-Clark.

Optimization of Microneedle Device Nanostructures

A microneedle based vaccine poses minimal risk of disease transfer and potentially reduces costs of vaccination campaigns. Additionally, the nanostructures have the potential to modulate the immune response within the skin[11,12], as well as the induction of immunological memory[13,14]. As a proof-of-concept for the microneedle patch as a vaccine delivery device, a transport study was performed to determine the feasibility of cercarial elastase delivery across the skin barrier. A subsequent study to test vaccination efficacy using tetanus toxoid as the model antigen was also

performed to determine the effect of not including an adjuvant since neither alum nor mineral oil adjuvants would be compatible with the current device design.

**Results**

To examine the ability of our nanostructured transdermal patch (NS patch) to deliver a protein-based vaccine and elicit an immune response, a rat tetanus vaccine model was used. Rats were randomly assigned to one of four groups: subcutaneous injection with vaccine, subcutaneous injection without vaccine, NS patch with vaccine or NS patch without vaccine. The vaccine or carrier was administered at day 0 and then again boosted at day 14. Blood samples were taken at days 0, 14, 28, and 32 and the level of anti-tetanus IgG was measured in the serum by ELISA. Although the subcutaneous injection elicited a more protective immune response as measured by anti-tetanus IgG level, the NS patch successfully elicited an immune response capable of producing antibody (Figure 3). This antibody response is more meaningful in the context that it was not possible to use an adjuvant with the patch design we had at the time of this experiment since mineral oil would clog the rate controlling membrane and alum would be too large to delivery by patch transdermally. Future work would investigate alternative adjuvants and determine whether the immune response is protective when challenged by the infectious agent.

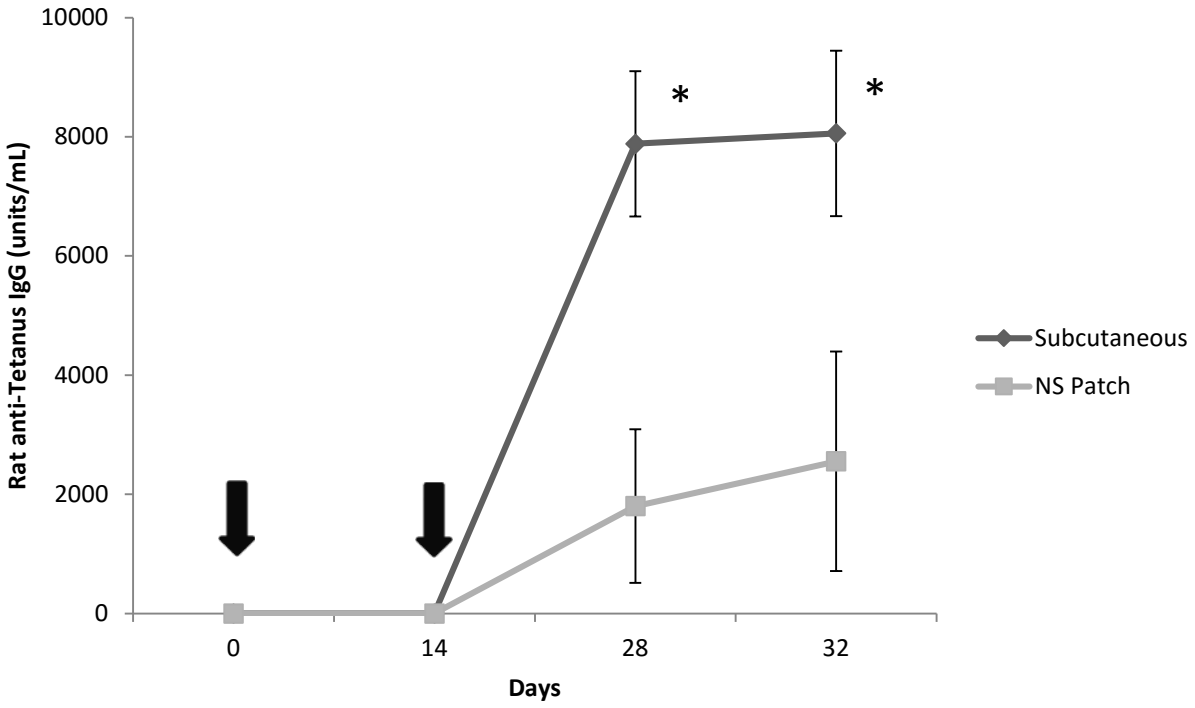


Figure 3 – Tetanus toxoid vaccination model in rats – Rats were vaccinated at days 0 and boosted at day 14 by either subcutaneous injection of tetanus vaccine or nanostructured patch (NS Patch) delivery of tetanus toxoid without adjuvant. Anti-Tetanus IgG was measured in the serum at days 0, 14, 28, and 32 (n=5). * = $p>0.05$ comparing subcutaneous to NS patch.

We then used the NS patch to deliver ecotin to *ex vivo* skin of mice as a proof of concept of vaccination against cercarial elastase. Initially we delivered ecotin into mouse skin and took samples at 3 and 6 hours post patch application. At 3 hours the device reservoir was observed to be empty and by western blot the ecotin was found to be predominantly in the phosphate buffered saline (PBS) on the basal side of the skin at both 3 and 6 hours as measured by western blot (Figure 4).

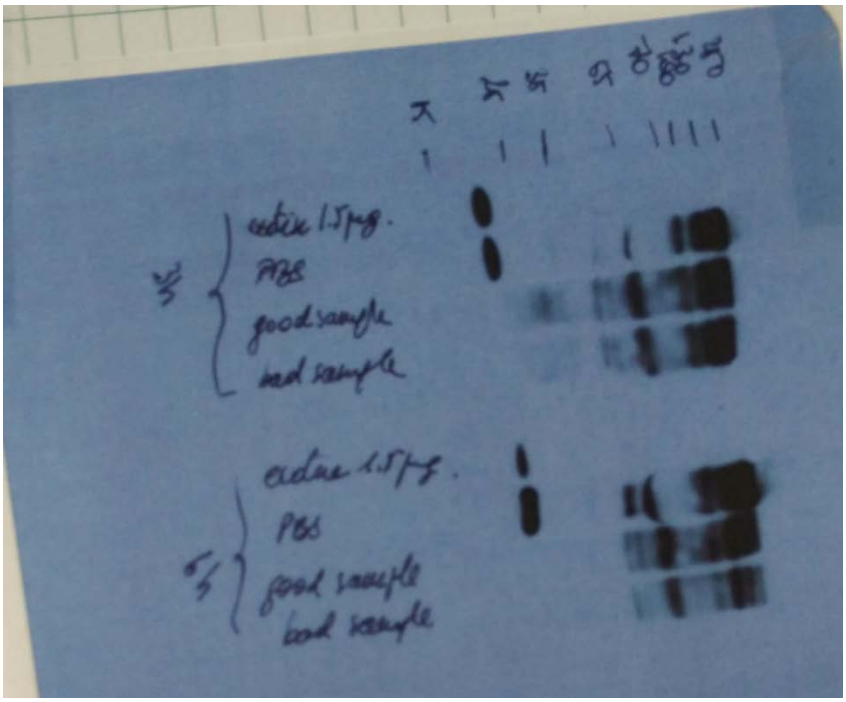


Figure 4 – Ecotin delivery to *ex vivo* mouse skin using NS patch. The columns are as follows: ecotin alone (ecotin 15 ug), PBS from under the basal surface of the skin (PBS), skin sample from below patch (good sample), and skin from outside the patch (bad sample) at 3 hours and 6 hours post device application.

To try and find the time when the ecotin is still in the skin, we shortened time the device was in contact with the skin. We sampled the skin at 30 minutes and 1 hour post device application. Similarly, we found the ecotin only in the PBS basal to the skin (Figure 5).

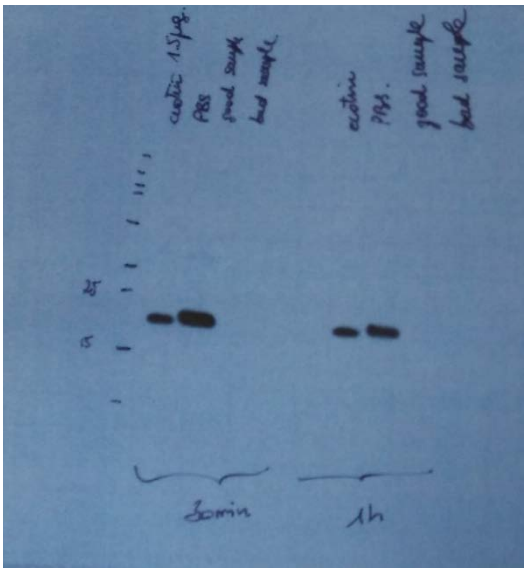


Figure 5 – Ecotin delivery to *ex vivo* mouse skin using NS patch. The columns are as follows: ecotin alone (ecotin 15 ug), PBS from under the basal surface of the skin (PBS), skin sample from below patch (good sample), and skin from outside the patch (bad sample) at 30 minutes and 1 hour post device application.

Even with shorter time points we were unable to find ecotin in the skin. Therefore, we further shortened the time points and modified our protocol. First, we did not put PBS below the skin during the experiment, in case the liquid drew the ecotin through the skin too quickly. Second, we performed the western blot on a skin sample that was not digested additionally with collagenase, in the case that the collagenase was breaking down the his-tag used to identify the ecotin. As seen with previous experiments, ecotin was only found to be present in the basal side of the skin (figure 6), suggesting that delivery of ecotin through the skin happens in a time period faster than 15 minutes.

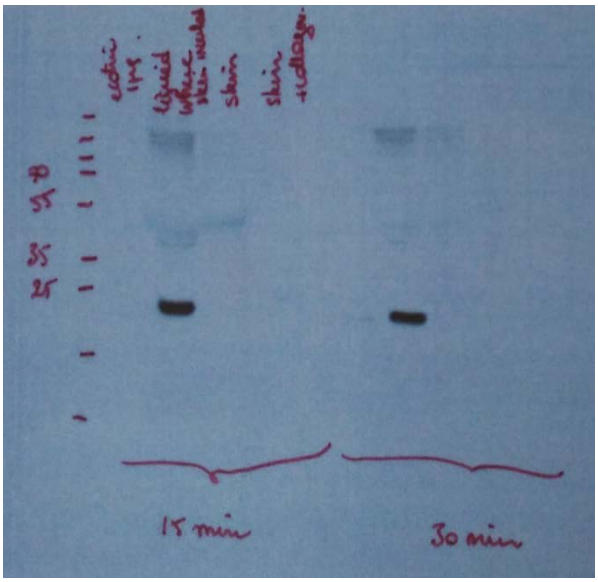


Figure 6 - Ecotin delivery to *ex vivo* mouse skin using NS patch. The columns are as follows: ecotin alone (ecotin 1 ug), liquid sample from under the basal surface of the skin (liquid where skin washed), skin sample physically disrupted (skin), and skin digested by collagenase (skin + collagen.) at 15 minutes and 30 minutes post device application.

We performed an *in vivo* proof of concept study, delivering ecotin to the skin of mice using the NS patch then challenging the skin under the device with cercaria. One group of mice was sacrificed after one day and the number of cercaria in the skin was counted. The second group of mice were sacrificed at a later time point and the number of eggs in the small intestines was counted. The number of cercaria in the skin and the number of eggs in the intestines were both decreased by ecotin delivery to the skin, but the protection was incomplete (data not shown).

**References**

1. Bergquist, R., Utzinger, J. & McManus, D. P. Trick or treat: the role of vaccines in integrated schistosomiasis control. (2008)*PLoS Negl. Trop. Dis.* **2**, e244.

2. McManus, D. P. & Loukas, A. (2008) Current status of vaccines for schistosomiasis. *Clin. Microbiol. Rev.* **21**, 225–242.
3. Mitragotri S. (2005) Immunization without needles. Nat Rev Immunol;5(December (12)):905–16.
4. Trommer, H., Neubert, R.H.H. (2006) Overcoming the Stratum Corneum: The Modulation of Skin Penetration. Skin Pharm. Phys.;19:106-121.
5. Escobar-Chavez J.J., Bonilla-Martinez D.; Villegas-Gonzalez M.A.; et al. (2011) Microneedles: A Valuable Physical Enhancer to Increase Transdermal Drug Delivery. J of Clinical Pharm: 51(7):964 -977.
6. Scheindlin, S. Transdermal (2004).Drug Delivery: PAST, PRESENT, FUTURE. *Molecular Interventions* **4**, 308 -312.
7. Walsh L, Ryu J, Bock S, Koval M, Mauro T, Ross R, Desai T. Nanotopography facilitates in vivo transdermal delivery of high molecular weight therapeutics through an integrin-dependent mechanism.*Nano Letters*, 2015, 15 (4), pp 2434–2441.
8. Hansell E, Braschi S, Medzihradszky KF, Sajid M, Debnath M, et al. (2008) Proteomic analysis of skin invasion by blood fluke larvae. PLoS Negl Trop Dis 2: e262.
9. Knudsen GM, Medzihradszky KF, Lim KC, Hansell E, McKerrow JH (2005) Proteomic analysis of Schistosoma mansoni cercarial secretions. Mol Cell Proteomics 4: 1862-1875.
10. Salter JP, Lim KC, Hansell E, Hsieh I, McKerrow JH (2000) Schistosome invasion of human skin and degradation of dermal elastin are mediated by a single serine protease. J Biol Chem 275: 38667-38673.

11. Anslie K.M., Bachelder E.M., Sharma G., Grimes C.A., Pishko M.V. (2007) Macrophage cell adhesion and inflammation cytokines on magnetostrictive nanowires. Nanotox.1(4):279-290.
12. Riedel M., Muller B., Wintermantel E. (2001) Protein adsorption and monocyte activation on germanium nanopyramids. Biomaterials 22:2307-2316.
13. Carey J.B., Pearson F.E, Vrdoljak A., McGrath M.G., Crean A.M., et al. (2011) Microneedle array design determines the induction of protective memory $CD8^+$ T cell responses induced by a recombinant live malaria vaccine in mice. PLoS ONE 6(7): e22442.
14. Koutsonanos DG, del Pilar Martin M, Zarnitsyn VG, Jacob J, Prausnitz MR, Compans RW, Skountzou, I. (2011) Serological Memory and Long-term Protection to Novel H1N1 Influenza Virus After Skin Vaccination. JID 204 (15 August): 582-591.
15. Van Damme P, Oosterhuis-Kafeja F, Van der Wielen M, Almagor Y, Sharon O, Levin Y. (2009) Safety and efficacy of a novel microneedle device for dose sparing intradermal influenza vaccination in healthy adult. Vaccine 27: 454-459.

# Appendix 3 - Controlling Attachment and Detachment of Cell Sheets on a Thermally-Responsive Polymer Surface


## Abstract

Cell sheet fabrication (CSF) is a technique whereby a confluent layer of cells can be easily released through a temperature "switch." CSF has major applications in tissue reconstruction and regenerative medicine. One example of a clinical application of CSF is in myocardial infarctions. In the U.S. alone there are about 1.5 million cases of myocardial infarctions per year. The infracted area forms scar tissue that doesn't contract and is not electrically active, so the pumping function of the heart is compromised. Potentially, the ability to implant cell sheets over the area of infraction will restore some function to the area in human patients, as has already been demonstrated in animal models. However, there is a lack of general applicability of CSF to multiple cell types. This project's aim was to better understand the mechanism of cell attachment and detachment in order to enable this technique to be more broadly applied. Understanding the determining factors of the success of CSF would be one step towards being able to not only broaden the understanding and applications of this technique, but also bring it closer to more human clinical applications.


## Introduction

A common material that is used for CSF is the thermoresponsive polymer poly-(N-isopropylacrylamide) (pNIPAM). pNIPAM undergoes a phase change within a physiological temperature range (Figure 1). At temperatures higher than its lower critical solution temperature (LCST), of around 32°C, pNIPAM is relatively hydrophobic and takes on a globular conformation, allowing cell adherence. Below that temperature, pNIPAM is hydrophilic and

hydrated, releasing adherent protein and cells (Figure 2). Four different methods, UV irradiation, electron beam irradiation (EB), surface initiated polymerization, and plasma-polymerization, can be used to successfully prepare pNIPAM grafted thermoresponsive surfaces. EB irradiation easily grafts a uniformly spread pNIPAM monomer layer onto tissue culture polystyrene (TCPS), and therefore will be used in our applications. Cells can be seeded onto the polymer grafted surface at 37°C. Once confluent, the cells can spontaneously detach as a biologically active and functional cell sheet by lowering the temperature to 20°C, below the

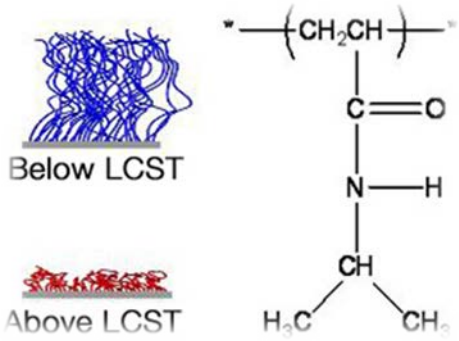


LCST of pNIPAM. Therefore, an intact cell sheet is obtained, without using physical scraping or harsh chemical treatments, such as trypsin, that can damage the cells or disturb the extracellular matrix (ECM) (Figure 3).

Figure 1 – pNIPAM conformation below LCST (hydrated) and above LCST (globular), and chemical structure. © 2011 Society For Biomaterials

The success of the CSF technique is dependent on successful cell attachment to and detachment from the polymer. There are differences in cell behavior on pNIPAM coated surfaces between different cell types and species. Our proposal investigates why only certain cell types can be used for CSF. Most current methods for controlling cell attachment and detachment focus on physical properties of the surfaces or media conditions. The exact mechanism of cell detachment

is not fully understood. It is proposed that detachment is a two step process, requiring both passive hydration of the pNIPAM chains during initial detachment and active cell processes for the second step. The second, or active, phase requires ATP generation, tyrosine phosphorylation activity, and preserved cytoskeletal dynamics. Understanding the scientific mechanisms of how different cell types adhere to pNIPAM has tremendous impact on the general applicability of CSF to multiple cell types.

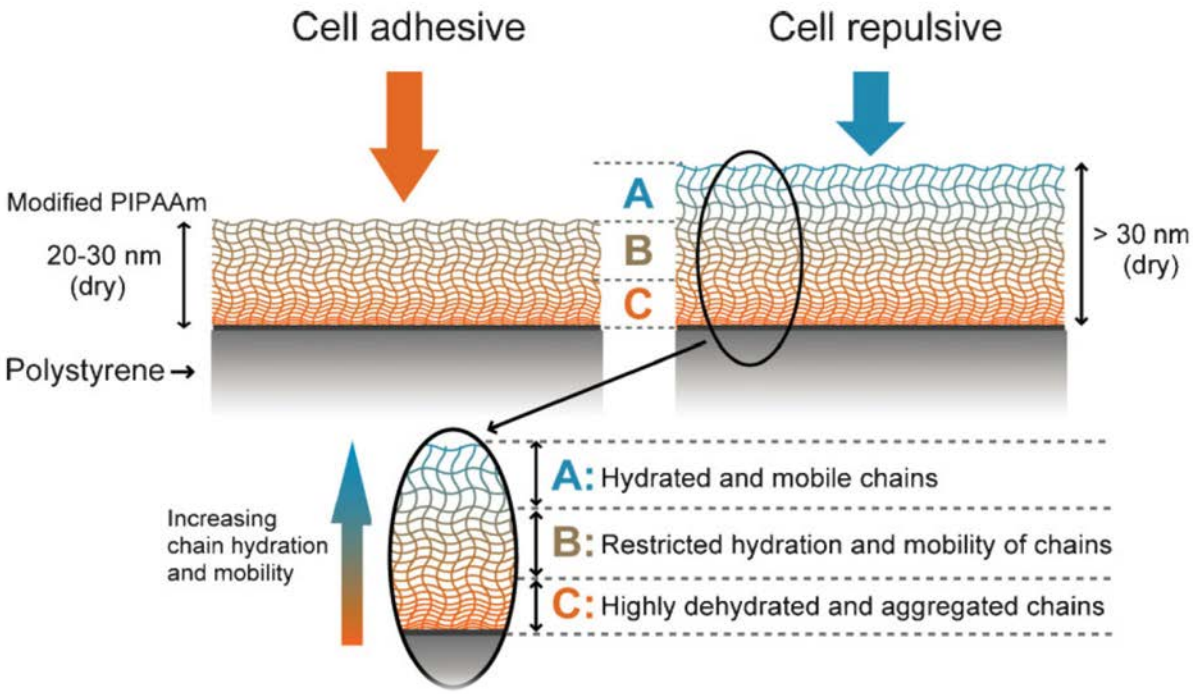


Figure 2 – pNIPAM repels cells below LCST. Fukumori K., Akiyama Y., Kumashiro Y., etal. 2010.

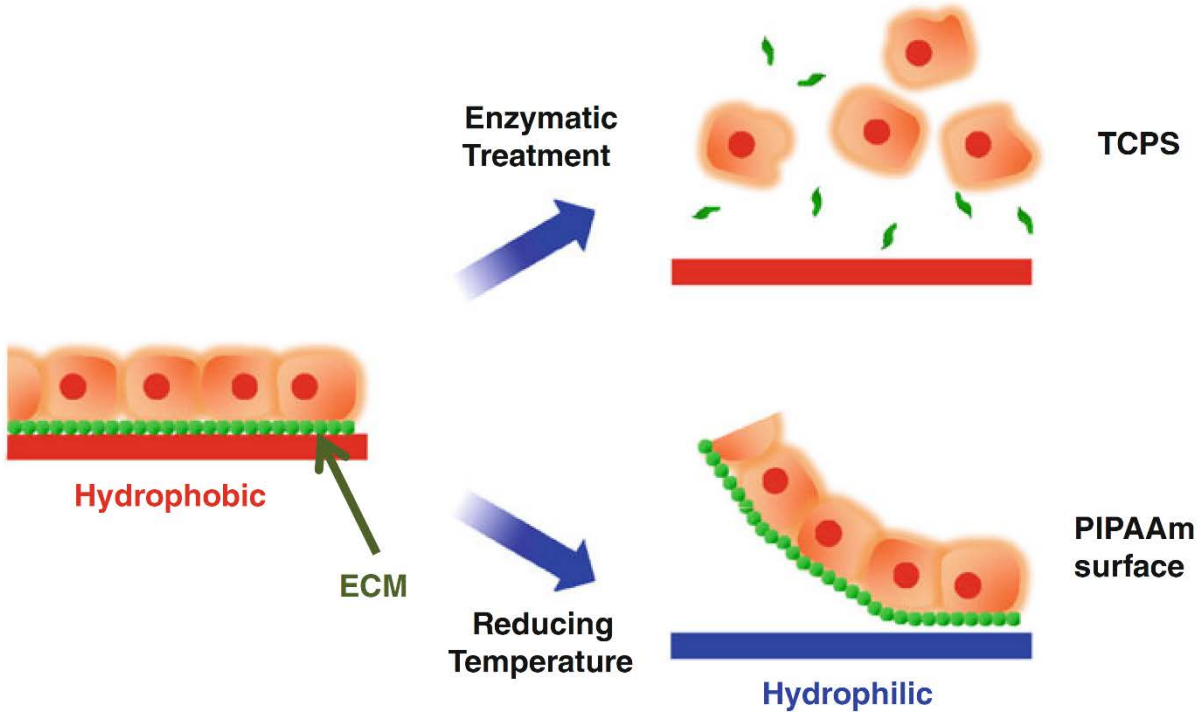


Figure 3 – Below the LCST of pNIPAM, a cell sheet grown on the surface is released with its ECM in tact, versus harsh enzymatic treatments where cells are dissociated from one another as well as from the surface. Kumashiro Y., Yamato M, Okano T. 2010

**Results**

To optimize culturing conditions for keratinocyte cell sheets, we examined the effect of both culture medium and surface coating for keratinocyte outgrown from the primary tissue sample. All three coatings resulted in keratinocyte outgrowth and culture on petri dishes, as measured by number of cells. However, cellular viability was the least on poly-lysine coated TCPS. Although all surface treatments showed successful outgrowth, the culture medium was critical for cellular proliferation. Keratinocyte culture medium was the only medium that successfully supported keratinocyte outgrowth, since primary tissue samples cultured in keratinocyte growth medium showed little to no cell outgrowth. Fibroblast culture was least successful on poly-lysine coated

TCPS, suggesting that poly-lysine coating would be a possible way to select for keratinocyte over fibroblast growth since poly-lysine coating preserved the number of keratinocytes, which fibroblast growth was decreased 2 fold. These results suggest that adsorbing either collagen 1 or poly-lysine to the pNIPAM surface may increase the success of forming keratinocyte cell sheets with the added benefit of keeping fibroblast growth minimized.

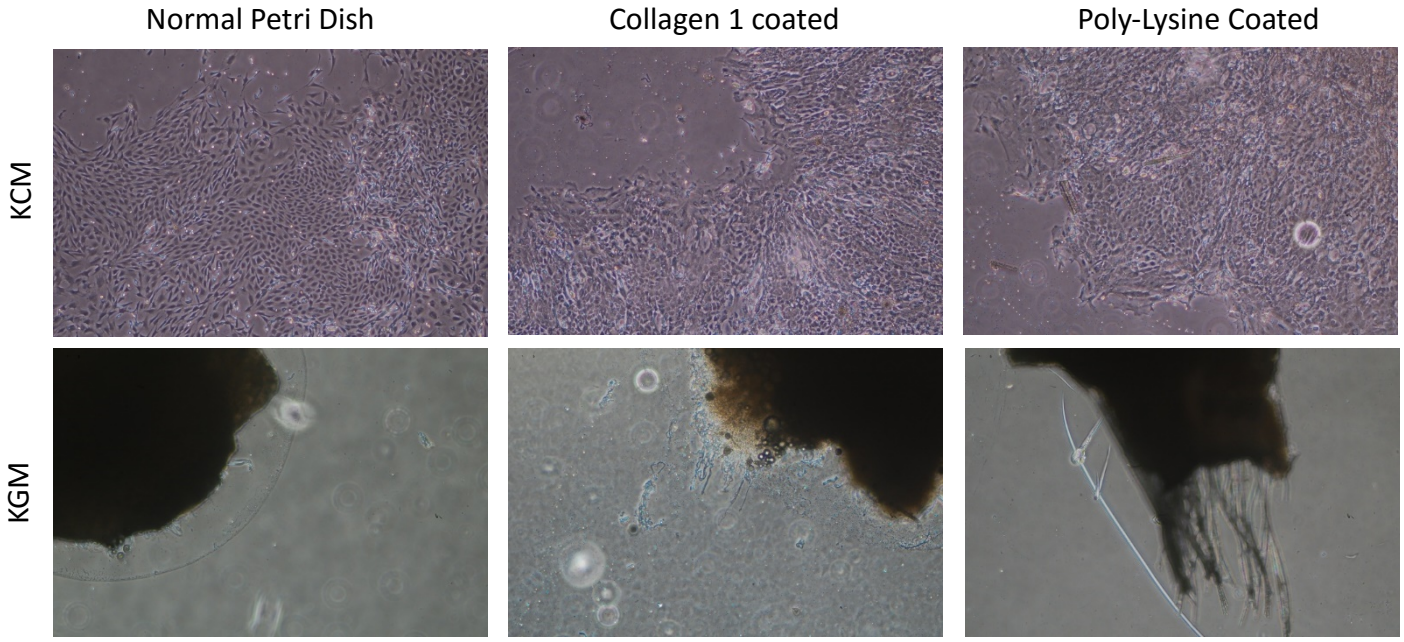


Figure 4 – Keratinocyte explant culturing comparing surface coating of the dish with nothing (normal petri dish), collagen 1 coated, and poly-lysine coated. Cells were cultured in either keratinocyte culture medium or keratinocyte growth medium.

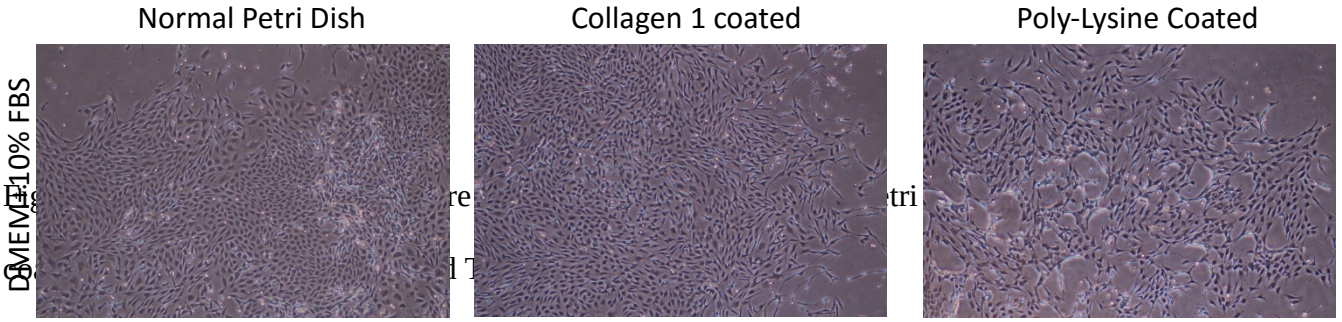


Fig re tri
Co l 1

| | | Normal Dish | Collagen I Coated | Poly-Lysine Coated |
|---|---|---|---|---|
| **Cell Viability** | Keratinocyte | 97.6% | 93.75% | 83.4% |
| | Fibroblast | 99.8% | 98.5% | 98.7% |
| **Cells/mL** | Keratinocyte | $8.2x10^5$ | $4.8x10^5$ | $7.8x10^5$ |
| | Fibroblast | $2.6x10^6$ | $1.34x10^6$ | $1.15x10^6$ |

Table 1 – Explant culture viability and proliferation

To examine whether protein adhesion and adsorption to the pNIPAM inserts affected successful cell sheet growth and isolation, we compared the surface of the insert with and without culture proteins from fetal bovine serum in the culture medium and compared it the inserts post cell sheet recovery. Keratinocyte cell sheets are more difficult to isolate since the sheet does not release cleanly when the temperature is lowered, as appreciated by the ragged edges post isolation.(Figure 6, b) This is in comparison with more easily isolated cells sheets such as oral mucosal cell sheets (Figure 6, a).

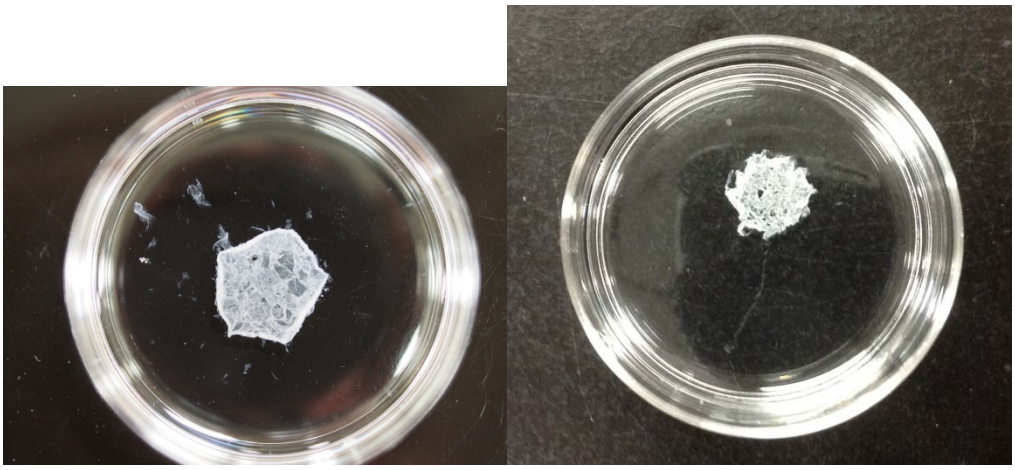

Figure 6 – a) Rat oral mucosa cell sheet grown in KCM (12 days) b) rat keratinocyte cell sheet grown in KCM with 3T3 feeder cells (13 days)

Keratinocyte cell sheets were isolated with and without the addition of an E cadherin antibody to block basolateral E cadherin.(Fukuyama & Shimizu, 1991) The surfaces of the pNIPAM inserts were then examined by atomic force microscopy (AFM) and x-ray photoelectron spectroscopy (XPS) (data not shown) for differences to identify adsorbed proteins common for successful cell sheet detachment. AFM imaging shows that the range of heights are similar between conditions (Figures 8, 10, 12) However, the phase data from the AFM show differences between conditions, suggesting that the proteins adsorbed to the inserts and therefore the surfaces that present to cells are indeed different (Figures 9, 11, 13). Further work up of this data and the raw XPS data is needed to determine possible protein based differences that might determine successful cell sheet detachment. These results could be used to identify proteins that could be functionalized to the polymer surface to either block cellular interaction or increase adhesion resulting in increased ease of working with difficult cell types.

Cellular surface receptors for extracellular matrix proteins are possibly another determining factor of ease of cell sheet isolation. Differential expression of integrins, which are a class of

cell surface receptors that bind to conserved motifs presented by extra cellular matrix proteins, may be predictive. The integrin expression profile of four different cell types ranging from easy to isolate cell sheets, oral mucosal cells, to difficult to isolate, fibroblast, was determine by qPCR of multiple integrins of both alpha and beta subtypes (Figure 7). Noting the similarity of integrin expression by keratinocyte culture with a feeder cells to fibroblast cells suggest that culture with feeder cells may create a cell sheet that is easier to harvest since keratinocytes cultured without feeder cells is more similar to oral mucosal cells. This work could be expanded to examine other culturing techniques effect on integrin expression, and expanded to investigate further cell surface receptors.

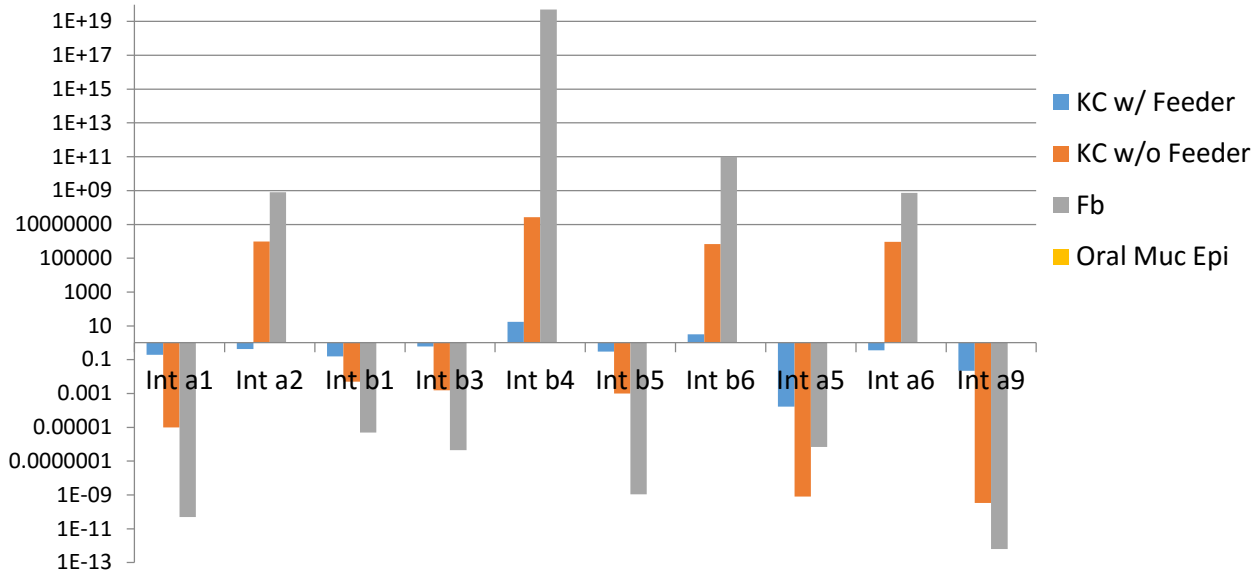


Figure 7 – Cell Sheet Intergrin Expression - qPCR of rat primary oral mucosal epithelial cells (oral muc epi) in yellow, keratinocyte with 3t3 feeder cells (KC w/ Feeder) in blue, keratinocytes without feeder 3T3 cells (KC w/o feeder) in orange, and fibroblast (fb) cell sheets in gray. Expression of integrins α-1,3,5,6,9 and β-1,3,4,5,6 was measured.

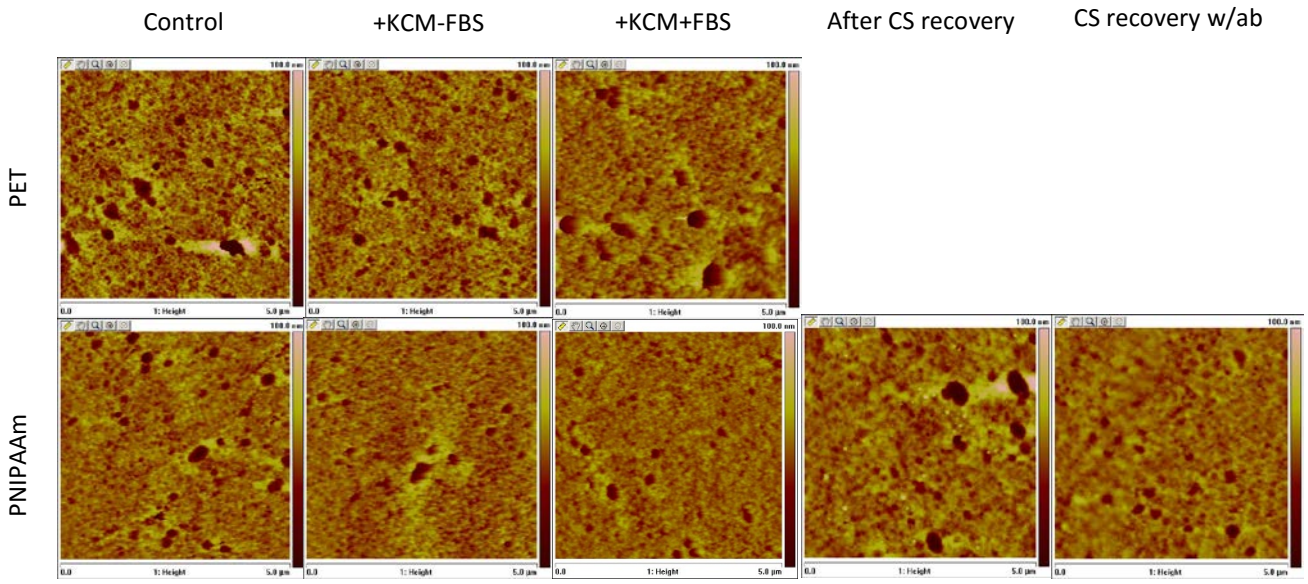


Figure 8 – AFM height measurement in 5 um area of inserts made of polyethylene terephthalate (PET) or pNIPAAm. These inserts were untreated (control), treated with KCM without FBS (+KCM-FBS), treated with KCM with FBS (+KCM+FBS), after cell sheet recovery (after CS recovery) or after cell sheet recovery in the presence of E-cad antibody (CS recovery w/ ab).

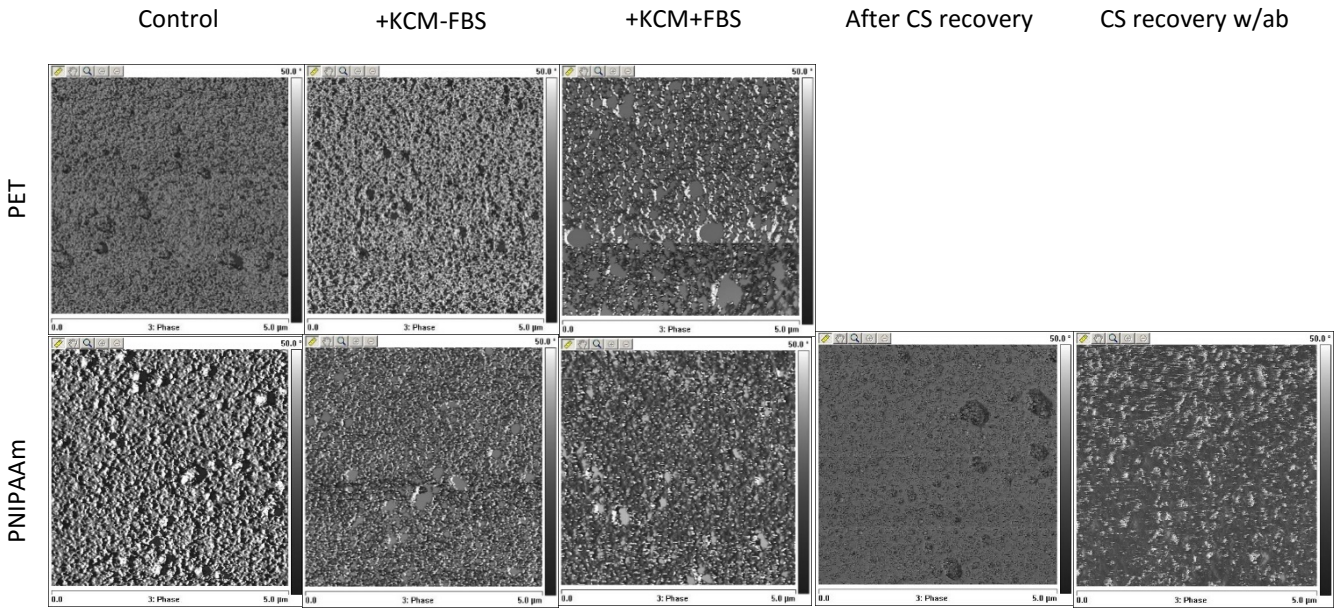

Figure 9 – AFM phase measurement in 5 um area of inserts made of polyethylene terephthalate (PET) or pNIPAAm. These inserts were untreated (control), treated with KCM without FBS (+KCM-FBS), treated with KCM with FBS (+KCM+FBS), after cell sheet recovery (after CS recovery) or after cell sheet recovery in the presence of E-cad antibody (CS recovery w/ ab).

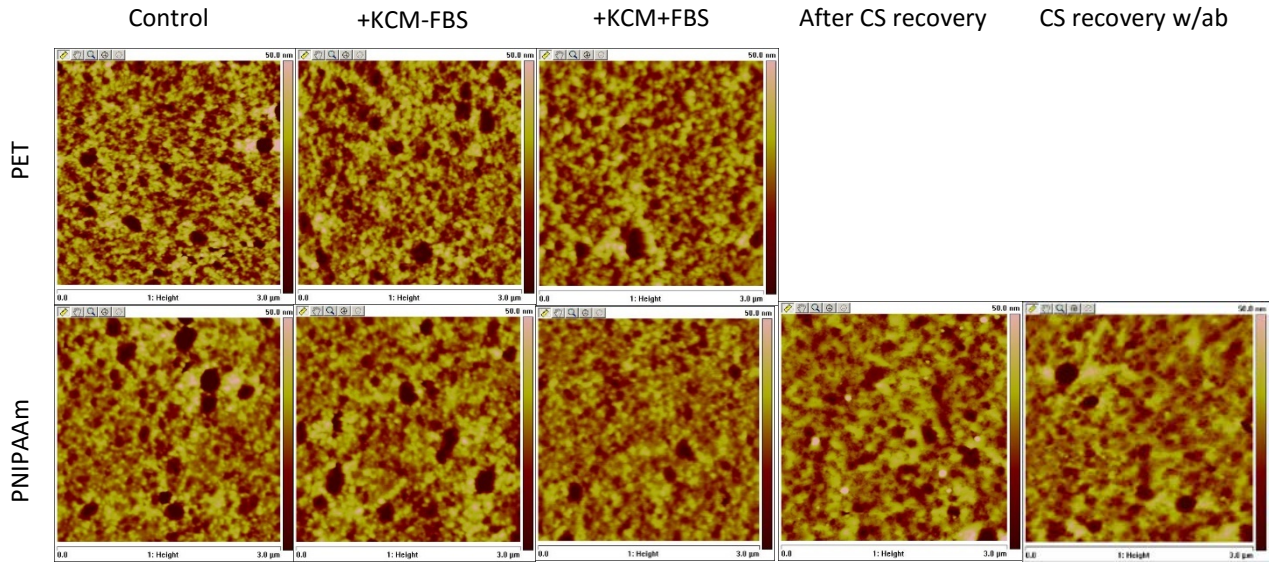


Figure 10 – AFM height measurement in 3 um area of inserts made of polyethylene terephthalate (PET) or pNIPAAm. These inserts were untreated (control), treated with KCM without FBS (+KCM-FBS), treated with KCM with FBS (+KCM+FBS), after cell sheet recovery (after CS recovery) or after cell sheet recovery in the presence of E-cad antibody (CS recovery w/ ab).

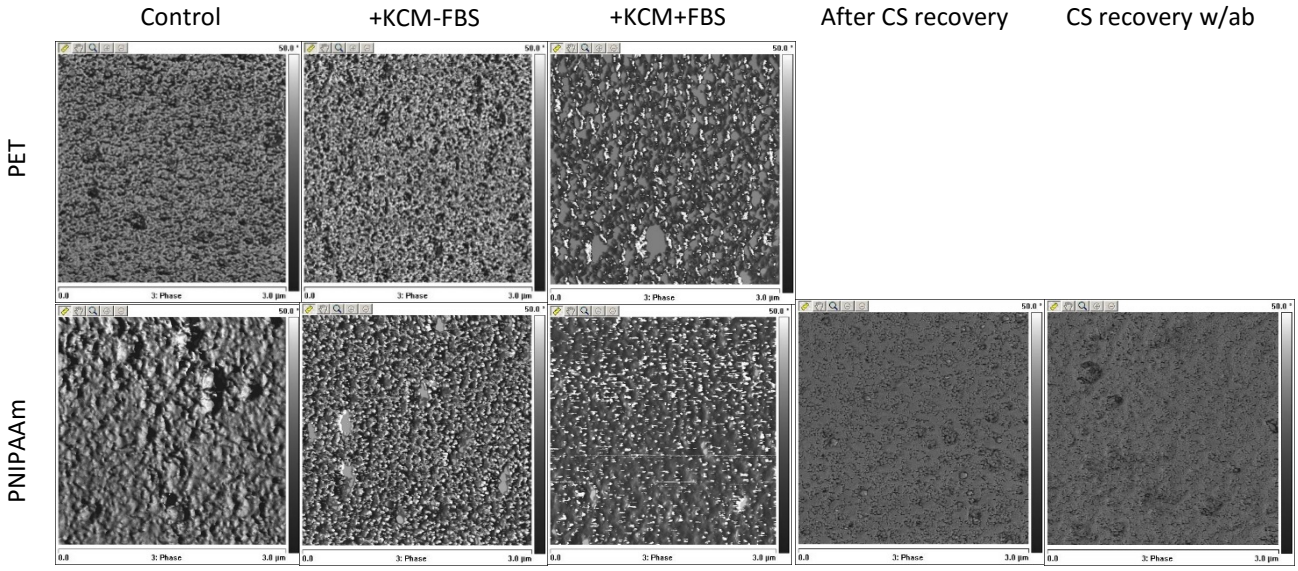

Figure 11 – AFM phase measurement in 3 um area of inserts made of polyethylene terephthalate (PET) or pNIPAAm. These inserts were untreated (control), treated with KCM without FBS (+KCM-FBS), treated with KCM with FBS (+KCM+FBS), after cell sheet recovery (after CS recovery) or after cell sheet recovery in the presence of E-cad antibody (CS recovery w/ ab).

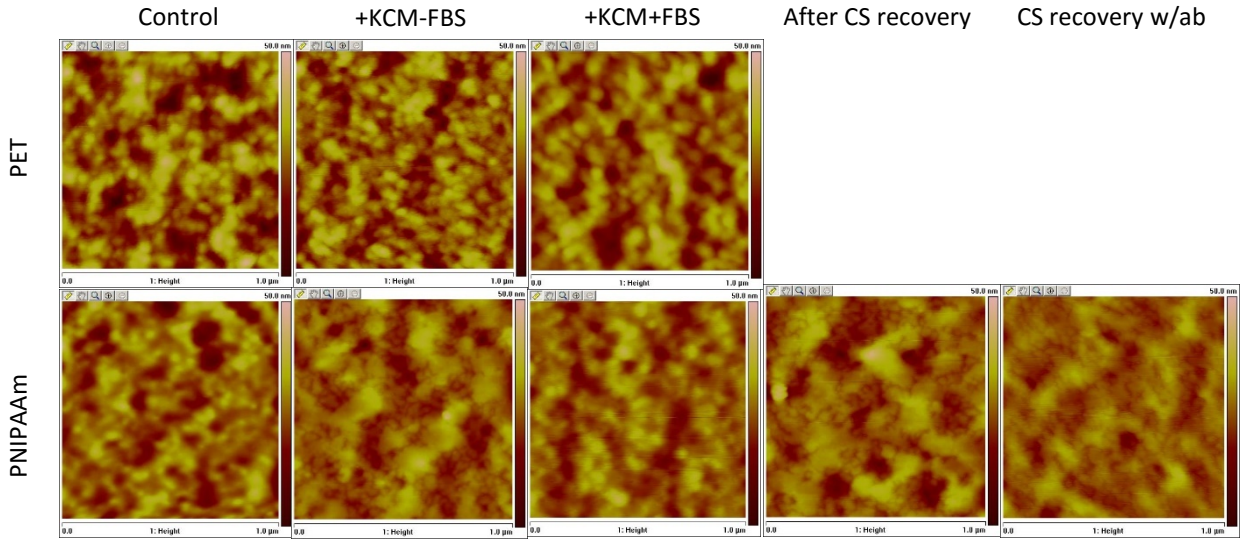


Figure 12 – AFM height measurement in 1 um area of inserts made of polyethylene terephthalate (PET) or pNIPAAm. These inserts were untreated (control), treated with KCM without FBS (+KCM-FBS), treated with KCM with FBS (+KCM+FBS), after cell sheet recovery (after CS recovery) or after cell sheet recovery in the presence of E-cad antibody (CS recovery w/ ab).

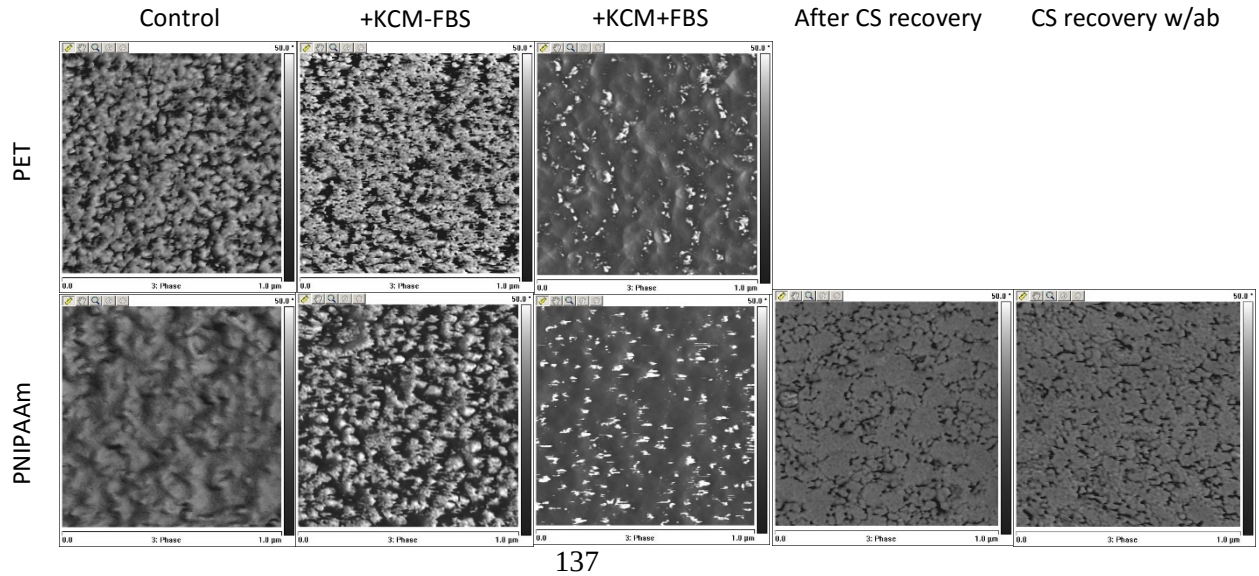

Figure 13 – AFM phase measurement in 1 um area of inserts made of polyethylene terephthalate (PET) or pNIPAAm. These inserts were untreated (control), treated with KCM without FBS (+KCM-FBS), treated with KCM with FBS (+KCM+FBS), after cell sheet recovery (after CS recovery) or after cell sheet recovery in the presence of E-cad antibody (CS recovery w/ ab).

**Publishing Agreement**

*It is the policy of the University to encourage the distribution of all theses, dissertations, and manuscripts. Copies of all UCSF theses, dissertations, and manuscripts will be routed to the library via the Graduate Division. The library will make all theses, dissertations, and manuscripts accessible to the public and will preserve these to the best of their abilities, in perpetuity.*

***Please sign the following statement:***

*I hereby grant permission to the Graduate Division of the University of California, San Francisco to release copies of my thesis, dissertation, or manuscript to the Campus Library to provide access and preservation, in whole or in part, in perpetuity.*

Author Signature

3-21-2016

Date